NTNU – Trondheim
Norwegian University of
Science and Technology

A Multi-Scale Approach for Modelling of Fracture in Aluminium Alloys under Impact Loading

Bjørn Håkon Frodal
Heidi Valle

Mechanical Engineering
Submission date: June 2015
Supervisor: Tore Børvik, KT
Co-supervisor: Odd Sture Hopperstad, KT
Jens Kristian Holmen, KT
Lars Edvard Dæhli, KT

Norwegian University of Science and Technology
Department of Structural Engineering

Department of Structural Engineering
Faculty of Engineering Science and Technology
NTNU- Norwegian University of Science and Technology

ACCESSIBILITY

OPEN

MASTER'S THESIS 2015

SUBJECT AREA:	DATE:	NO. OF PAGES:
Computational Mechanics	10 June 2015	18+144+26

TITLE:

A multi-scale approach for modelling of fracture in aluminium alloys under impact loading

BY:

Bjørn Håkon Frodal
Heidi Valle

SUMMARY:
The main objective of this thesis was to investigate the ballistic properties of an isotropic AlMgSi aluminium alloy both experimentally and numerically. Uncoupled and coupled fracture models were calibrated using micromechanical unit cells and existing material data, to model ductile fracture in the alloy.

Ballistic impact experiments were conducted on 30 mm thick plates at the Departement of Structural Engineering at NTNU, using the steel core of 7.62 mm APM2 bullets. The Recht-Ipson model was used to obtain the ballistic limit curve, and good correspondence was seen between the curve and the experimental results. Ductile hole growth proved to be the dominant failure mechanism for all tests, with negligible fragmentation.

Simplified two-dimensional micromechanical cells were analysed for different Lode parameters and triaxialities, to calibrate the Cockcroft-Latham, Johnson-Cook and Gurson-Tvergaard-Needleman (GTN) failure models. The calibrations were done with either a von Mises yield criterion or GTN in the matrix material, resulting in lower failure strains for the latter.

Numerical analyses of the ballistic impacts were conducted in both IMPETUS Afea Solver and Abaqus/Explicit. A parameter study investigating the effects of strain rate, temperature and friction, concluded that friction had the largest influence on the ballistic limit velocity. Abaqus analyses gave the overall best correspondence with the experimental data, with only minor deviations between the fracture models. These deviations were probably due to the dominating temperature erosion criterion. Larger differences were seen between the models for the IMPETUS analyses. Both IMPETUS and Abaqus were able to recreate the deformation pattern seen in the experimental tests. The use of micromechanical cells for numerical modelling of ductile fracture is considered promising.

RESPONSIBLE TEACHER: Professor Tore Børvik

SUPERVISORS: Professor Tore Børvik, Professor Odd Sture Hopperstad, PhD Candidate Jens Kristian Holmen and PhD Candidate Lars Edvard Dæhli

CARRIED OUT AT: SIMLab, The Departement of Structural Engineering, NTNU

Institutt for konstruksjonsteknikk
Fakultet for ingeniørvitenskap og teknologi
NTNU- Norges teknisk- naturvitenskapelige universitet

TILGJENGELIGHET

ÅPEN

MASTEROPPGAVE 2015

FAGOMRÅDE:	DATO:	ANTALL SIDER:
Beregningsmekanikk	10. juni 2015	18+144+26

TITTEL:

En multiskala tilnærming for modellering av brudd i aluminiumslegeringer ved støtlast

UTFØRT AV:

Bjørn Håkon Frodal
Heidi Valle

SAMMENDRAG:
Hovedmålet med denne avhandlingen var å undersøke de ballistiske egenskapene til en isotrop AlMgSi-aluminiumslegering, både eksperimentelt og numerisk. Ukoblede og koblede bruddmodeller ble kalibrert ved bruk av mikromekaniske enhetsceller og eksisterende materialdata, for å modellere duktilt brudd.

Ballistiske tester ble utført på 30 mm tykke plater ved Institutt for konstruksjonsteknikk ved NTNU, hvor stålkjernen fra 7,62 mm APM2 kuler ble benyttet. Recht-Ipson modellen ble brukt for å finne den ballistiske grensekurven, og god korrespondanse ble sett mellom kurven og de eksperimentelle resultatene. Duktil hullutvidelse viste seg å være den dominerende bruddmekanismen for alle testene, med neglisjerbar fragmentering.

Forenklede todimensjonale mikromekaniske celler ble analysert for ulike Lode-parametre og triaksialiteter, for å kalibrere bruddmodellene Cockcroft-Latham, Johnson-Cook og Gurson-Tvergaard-Needleman (GTN). Kalibreringene ble utført med enten et von Mises flytekriterium eller GTN i matriksmaterialet, som resulterete i lavere bruddtøyning for sistnevnte.

Numeriske analyser av de ballistiske testene ble gjennomført i både IMPETUS Afea Solver og Abaqus/Explicit. Et parameterstudie som undersøkte effekten av tøyningsrate, temperatur og friksjon, konkluderte med at friksjonen hadde størst innflytelse på den ballistiske grensen. Abaqus-analysene ga den generelt beste korrespondansen med de eksperimentelle resultatene, med kun mindre avvik mellom bruddmodellene. Disse avvikene var sannsynligvis på grunn av det dominerende temperaturerosjonskriteriet. Større forskjeller ble sett mellom modellene i IMPETUS. Både IMPETUS og Abaqus var i stand til å gjenskape deformasjonsmønsteret sett i de eksperimentelle testene. Bruken av mikromekaniske celler for numerisk modellering av duktilt brudd vurderes som lovende.

FAGLÆRER: Professor Tore Børvik

VEILEDERE: Professor Tore Børvik, Professor Odd Sture Hopperstad, ph.d. kandidat Jens Kristian Holmen og ph.d. kandidat Lars Edvard Dæhli

UTFØRT VED: SIMLab, Institutt for konstruksjonsteknikk, NTNU

Department of Structural Engineering
FACULTY OF ENGINEERING SCIENCE AND TECHNOLOGY
NTNU – Norwegian University of Science and Technology

MASTER'S THESIS 2015

for

Bjørn Håkon Frodal and Heidi Valle

A multi-scale approach for modelling of fracture in aluminium alloys under impact loading

1. INTRODUCTION

CASA (Centre for Advanced Structural Analysis) is the new Centre for Research-based Innovation hosted by SIMLab and the Department of Structural Engineering at NTNU. The purpose of this research center is to create a platform for credible numerical simulations of structures for innovation and value creation in e.g. enterprises working with physical security through multi-scale testing, modelling and simulation. Coupling of the micro-scale (particle size) and the macro-scale (component size) is a central part of the research activities within CASA. The main idea with this master's thesis project is to provide new insight into ductile fracture modelling. Isotropic aluminium made for SIMLab in cooperation with Norsk Hydro ASA will be used in this work since it is an ideal subject to couple micromechanical modelling with common phenomenological approaches used in structural problems such as impact events.

2. OBJECTIVES

The research project has three main objectives: (1) investigate experimentally the ballistic properties of a cast and homogenized AlMgSi aluminium alloy, (2) couple the micromechanical unit-cell approach and the Gurson porous plasticity model to the phenomenological descriptions of fracture commonly used in impact analyses, i.e., to calibrate the Cockcroft-Latham and the Johnson-Cook fracture criteria, (3) predict the behaviour of the plates under impact loading with the nonlinear finite element method through the use of the IMPETUS Afea Solver and Abaqus/Explicit.

3. A SHORT DESCRIPTION OF THE RESEARCH PROJECT

The main topics in the research project will be as follows;

1. Plates are made of a cast and homogenized AlMgSi aluminium alloy. The size of the plates will be determined by numerical simulations.
2. A literature survey is done to obtain a theoretical foundation in constitutive modelling, fracture modelling, porous plasticity and ballistic impact.
3. Already available material data from tension tests are used to calibrate constitutive models and fracture criteria. The following approaches are suggested:
    a. Use a well-known technique to obtain the parameters in a Johnson-Cook type constitutive model and the Cockcroft-Latham fracture criterion from experimental data.
    b. Employ a unit-cell model to calibrate the Gurson porous plasticity model and subsequently calibrate typical fracture criteria.
4. Ballistic tests are performed using 7.62 mm bullets to determine the ballistic properties of the alloy.
5. Numerical simulations of the ballistic impact experiments are carried out in the IMPETUS Afea Solver and Abaqus/Explicit.
6. The numerical results are compared and discussed in relation to the experimental findings.

Supervisors: Tore Børvik, Odd Sture Hopperstad, Jens Kristian Holmen, Lars Edvard Dæhli (NTNU)

The thesis must be written according to current requirements and submitted to Department of Structural Engineering, NTNU, no later than June 10th, 2015.

NTNU, January 14th, 2015

Tore Børvik
Professor

Preface

This thesis was written for the Structural Impact Laboratory (SIMLab) at the Norwegian University of Science and Technology (NTNU) during 20 weeks in the spring of 2015. The thesis is a requirement for the degree of Master of Science at NTNU, and finalized our study in the programme Mechanical Engineering, with specialization in Applied Mechanics. The master thesis was carried out under supervision of Professor Tore Børvik, Professor Odd Sture Hopperstad and PhD Candidates Lars Edvard Dæhli and Jens Kristian Holmen at the Department of Structural Engineering at NTNU.

Acknowledgements

First, we would like to thank Engineer Tore Kristensen at SINTEF for conducting the tensile tests, as well as Senior Engineer Trond Auestad for helping us carry out the ballistic experiments. Also, thanks to Engineer Tore Wisth for making the rigid steel frame used in the ballistic experiments. Furthermore, we would like to thank Dr. David Morin for valuable assistance with Abaqus and the SIMLab Metal Model.

Associate Professor Ida Westermann was helpful with macro- and micro analyses of the target plates. She has provided essential metallurgical insight and given us information on the target material.

Big thanks are given to our supervisors, PhD Candidates Lars Edvard Dæhli and Jens Kristian Holmen, for valuable assistance and guidance throughout this semester. They were available to us at all times, and their doors were always open when input and advice were needed. Lars provided us with a Python script and a Fortran script for the axisymmetric unit cell model, and valuable insight on unit cell analyses. Jens proved invaluable when solving unexpected problems with IMPETUS Afea Solver. We highly appreciate their eagerness to help overcoming some of the obstacles faced along the way, as well as their prompt response on emails.

Lastly, we would like to thank our main supervisors, Professor Tore Børvik and Professor Odd Sture Hopperstad, for guidance and discussions during the work with this thesis. The weekly meetings and discussions have been helpful. We are grateful for having them as our supervisors, and feel that the present work has been educational due to their enthusiasm and knowledge.

Trondheim
June 10, 2015

Bjørn Håkon Frodal

Heidi Valle

Abstract

The main objective of this thesis was to investigate the ballistic properties of an isotropic AlMgSi aluminium alloy both experimentally and numerically. Uncoupled and coupled fracture models were calibrated using micromechanical unit cells and existing material data, to model ductile fracture in the alloy.

Ballistic impact experiments were conducted on 30 mm thick plates at the Department of Structural Engineering at NTNU, using the steel core of 7.62 mm APM2 bullets. The Recht-Ipson model was used to obtain the ballistic limit curve, and good correspondence was seen between the curve and the experimental results. Ductile hole growth proved to be the dominant failure mechanism for all tests, with negligible fragmentation.

Simplified two-dimensional micromechanical cells were analysed for different Lode parameters and triaxialities to calibrate the Cockcroft-Latham, Johnson-Cook and Gurson-Tvergaard-Needleman (GTN) failure models. The calibrations were done with either a von Mises yield criterion or GTN in the matrix material, resulting in lower failure strains for the latter.

Numerical analyses of the ballistic impacts were conducted in both IMPETUS Afea Solver and Abaqus/Explicit. A parameter study investigating the effects of strain rate, temperature and friction, concluded that friction had the largest influence on the ballistic limit velocity. Abaqus analyses gave the overall best correspondence with the experimental data, with only minor deviations between the fracture models. These deviations were probably due to the dominating temperature erosion criterion. Larger differences were seen between the models for the IMPETUS analyses. Both IMPETUS and Abaqus were able to recreate the deformation pattern seen in the experimental tests. The use of micromechanical cells for numerical modelling of ductile fracture is considered promising.

Contents

Nomenclature

α	Thermal expansion coefficient
$\dot{\boldsymbol{\varepsilon}}^{\boldsymbol{p}}$	Plastic strain rate tensor
$\boldsymbol{\sigma}^{'}$	Deviatoric stress tensor
$\boldsymbol{\varepsilon}$	Strain tensor
$\boldsymbol{\varepsilon}^{e}$	Elastic strain tensor
$\boldsymbol{\varepsilon}^{p}$	Plastic strain tensor
$\widetilde{\boldsymbol{\sigma}}$	Effective stress tensor
$\boldsymbol{C}$	4^{th} order tensor of elastic constants
$\boldsymbol{\sigma}$	Stress tensor
χ	Taylor-Quinney coefficient
$\ddot{\mathbf{D}}$	Acceleration
Δt_{cr}	Critical time step
δ_{ij}	Kronecker delta
$\dot{\lambda}$	Plastic multiplier
$\dot{\mathbf{D}}$	Velocity
$\dot{\omega}$	Change of the volume fraction of voids
$\dot{\omega}_g$	Change of the volume fraction of voids due to qrowth
$\dot{\omega}_n$	Change of the volume fraction of voids due to nucleation
$\dot{\omega}_s$	Change of the volume fraction of voids due to shear softening
$\dot{p}^*$	Dimensionless strain rate
ϵ_l	Logaritmic strain
γ	Shear strain
κ	Stress dependent parameter
$\mathbf{C}$	Damping matrix
$\mathbf{M}$	Mass matrix
$\mathbf{R}^{\mathbf{ext}}$	External forces

$\mathbf{R}^{\mathbf{int}}$	Internal forces
μ_σ	Lode parameter
ω	Damage parameter
ω_{max}	Highest natural frequency
ρ	Density
σ	Cauchy stress
σ^*	Stress triaxiality
σ_0	Initial yield stress
σ_I	Major principal stress
σ_{II}	Intermediate principal stress
σ_{III}	Minor principal stress
σ_H	Hydrostatic stress
σ_M	Flow stress of matrix material
σ_{VM}	von Mises stress
Σ_{eq}	Macroscopic von Mises equivalent stress
σ_{eq}	von Mises equivalent stress
Σ_H	Macroscopic hydrostatic stress
Σ_i	Macroscopic principal stresses
θ_L	Lode angle
ξ	Damping ratio
a	Cross-sectional radius
c_d	Dilatational wave speed
C_i	Material parameters Voce hardening law
C_p	Specific heat
D_i	Johnson-Cook parameters
E_{eq}	Macroscopic von Mises strain
E_i	Macroscopic logarithmic strains in the principal directions
f	Void volume fraction
f_0	Initial void volume fraction
f_c	Critical void volume fraction

H_0	Initial height of unit cell
H_ω	Damage modulus
J_2	Second principal invariant of $\boldsymbol{\sigma}'$
J_3	Third principal invariant of $\boldsymbol{\sigma}'$
k_s	Shear parameter
L^e	Characteristic length
m_p	Mass of projectile
p_0	Critical strain
p_f	Plastic strain at failure
Q_i	Material parameters Voce hardening law
R	Necking radius
R_0	Initial characteristic length of unit cell
r_0	Initial void radius
T	Current temperature
T^*	Homologous temperature
T_0	Ambient temperature
T_m	Melting temperature
U_0	Strain energy
V_0	Total initial cell volume
v_{bl}	Ballistic limit velocity
v_i	Initial/impact velocity
v_r	Residual velocity
W_c	Cockcroft-Latham material constant
V_{v0}	Initial void volume
a	Parameter in the Recht-Ipson model
D	Dissipated energy
E	Young's modulus
H	Height of unit cell
p	Accumulated plastic strain
p	Parameter in the Recht-Ipson model

R	Characteristic length of unit cell
R	Isotropic hardening variable

1 Introduction

Aluminium alloys are often used as an alternative to steel in protective structures due to their good energy absorption capability, high specific strength, low density, good corrosion resistance and good thermal conductivity [1]. Such alloys are particularly interesting in the fields of engineering based on lightweight structures, e.g., the automotive, aviation and military industries. The need for lightweight fortification for defence purposes is increasing [2], and for the design to be optimal regarding energy absorption there is a strong need of exact, efficient and robust constitutive equations and fracture models.

To fully elaborate the material properties of a given metal, extensive testing is needed to account for different loading cases. Typically this includes subjecting the material to tension, compression, shear, impact and explosion loading. It is therefore desirable to simplify the preliminary structural design phase, by minimizing the need of comprehensive material testing, and instead use existing data or simple material tests to establish the material model.

Lightweight aluminium structures are often designed to absorb energy due to impact loading, such as ballistic impacts. Previous research at SIMLab investigated the material behaviour of different aluminium alloys subjected to impact loading [1, 3, 4]. It was concluded that by taking areal mass into account, high-strength aluminium alloys may have equally good or even better perforation resistance than steel. Other recent studies indicated that the ballistic properties of plates are highly dependent on both material strength and local ductility [5, 6].

Ductile fracture in metals is governed by void nucleation, growth and coalescence. For high-strength aluminium alloys the strength is often obtained at the expense of ductility, which makes modelling of ductile fracture important [7]. To properly investigate the ductile fracture mechanism, micro-scale modelling has been used in several studies to examine void growth especially [8–12]. The main idea of micro-scale modelling is to reduce the number of material tests needed for determining a material's fracture properties. A reduction in number of extensive material tests will result in a more effective and profitable design phase.

The study on micro-scale material behaviour used in the present investigation is based on a review paper by Benzerga and Leblond [13]. The first analytical descriptions of void growth were given in the late 60's by McClintock [14] and Rice and Tracey [15]. The porous plasticity model developed by Gurson [16] in 1977 founded the constitutive framework on analysis of ductile fracture on a micro level. The Gurson model was later modified by both Tvergaard and Needleman [17] and Nahshon and Hutchinson [18], amongst others, to account for strain hardening, void interacting effects and softening due to shear. A study was performed by Gao and Kim [19] regarding the effect of different void shapes, which proved to be significant for void growth and coalescence.

To get a better understanding of how ductile fracture in aluminium alloys influences the response of structures under impact loading, and what causes these fractures, it is desirable to use micro-scale models to avoid comprehensive material testing. The micromechanical unit-cell approach and the Gurson porous plasticity model can be coupled to give phenomenological descriptions of fracture commonly used in impact analyses, i.e., the Cockcroft-Latham and Johnson-Cook fracture models [20, 21]. This coupling between micro- and macro analyses for ballistic impacts is a relatively unexplored field of science, and this thesis will hopefully provide some new insight into ductile fracture modelling.

In this thesis, the ballistic properties of isotropic 30 mm thick circular AlMgSi-plates are investigated both experimentally and numerically. This aluminium alloy is considered ideal for coupling of micromechanical modelling with common phenomenological approaches used in structural problems such as impact events, due to its isotropic material behaviour. The main objective is to calibrate different fracture models, both coupled and uncoupled, using computational unit cells and existing material data. These fracture models will be used in the numerical analyses for reproduction of the ballistic impacts.

This master thesis aims at using IMPETUS Afea Solver and Abaqus/Explicit to reproduce ballistic impacts from experimental tests. To be able to properly describe the material behaviour, tensile tests are conducted and investigated. Numerical analyses on micro-scale, using computational unit cells, are used to map the material behaviour by applying different loading cases. The microscopic unit cell results are to be connected to macroscopic fracture models, using MATLAB for the calibration process. These calibrated fracture models will further form the basis of the material used in the numerical analysis in IMPETUS. To verify the results from the IMPETUS analyses, an identical model is made in Abaqus.

An overview of the different chapters in this thesis is presented below.

Chapter 2 - Theory: This chapter contains relevant theoretical background for this thesis. It includes an introduction to impact dynamics, materials mechanics, micromechanical computational cells and some information on finite element analysis and codes.

Chapter 3 - Experimental Study: Describes the material at hand, the experimental setup and results from both tensile tests and ballistic impact tests, as well as macro-and microscopy of the target material.

Chapter 4 - Micromechanical Modelling: Description of the three different two-dimensional computational unit cells studied in this thesis. The results from the analyses are presented, as well as a comparison with three-dimensional cell data.

Chapter 5 - Calibration of Fracture Models: The results obtained from the tensile tests and the computational unit cell study are used to calibrate the Cockcroft-Latham, Johnson-Cook and Gurson-Tvergaard-Needleman fracture models. The fracture parameters are calibrated using a non-linear least-square algorithm, and a thorough discussion of the results is presented in the final section.

Chapter 6 - Preliminary Numerical Study: Description of the preliminary numerical study executed to investigate the influence of different parameters on the perforation

process. A pinhole study was conducted, as well as an investigation of different element erosion techniques in IMPETUS Afea Solver. A limited mesh sensitivity study is also presented.

Chapter 7 - Numerical Analyses of Ballistic Impacts: Presentation and discussion of the results from numerical analyses using all three fracture models. A comparison of the deformation pattern with the experimental tests studied in the macroscopy is also presented.

Chapter 8 - Concluding Remarks: This chapter contains an assessment of the experimental and numerical results in this thesis.

Chapter 9 - Future Work: Suggestions for further work on the topic of full scale modelling of aluminium is given.

2 Theory

In this chapter some relevant theoretical background is presented. First, an introduction to impact dynamics is given, followed by a section presenting relevant relations of materials mechanics. Further, a section is dedicated to the micromechanical unit cell modelling approach. Lastly, a brief introduction to the finite element method, as well as IMPETUS Afea Solver and SIMLab Metal Model, is given.

2.1 Impact Dynamics

"Structural impact is defined as the collision between two or more solids, where the interaction between the bodies may be elastic, plastic or fluid, or any combination of these" [2]. There are two important features that distinguish impact dynamics from other disciplines of classical mechanics which operates under quasi-static conditions; inertia effects and stress wave propagation. The governing equations, based on fundamental conservation laws of mechanics and physics, must include inertia effects to properly describe the structural impact problem. Stress wave propagation must be taken into account due to the fact that most impact events are highly transient phenomena, which may not have steady-state conditions. In addition, the short impact introduce effects that are not observed in quasi-statically loaded materials, such as thermal softening, strain rate dependency and hydrodynamic material behaviour.

An impact phenomenon may be influenced by several factors, such as impact angle, impact velocity, target and projectile geometry and material characteristics. These factors may yield different fracture modes in the target, which will be further discussed in Section 2.1.1 that presents some relevant definitions used in structural impact dynamics. Sections 2.1.2 and 2.1.3 present the ballistic limit velocity and the Recht-Ipson model, respectively.

2.1.1 Terminology

Ballistics is in modern science defined as the study of motion, forces and impact of free-flying projectiles, especially those discharged from firearms or guns. The science of ballistics can be divided into three main research areas [2]:

1. Interior: Study of the motion and forces acting on an object when it is still inside the launcher.
2. Exterior: Study of the motion and forces acting on an object during free flight.
3. Terminal: Study of the interaction between object and target during impact.

This thesis focuses only on terminal ballistics, since this is the area of interest in fortification, i.e., structures used for additional strengthening [2].

Projectiles are according to Zukas [22] any item that can be launched. They can be characterized as soft, semi-hard or hard depending on the degree of deformation during impact and the material used. Figure 2.1 illustrates some typical projectiles with different projectile nose shapes.

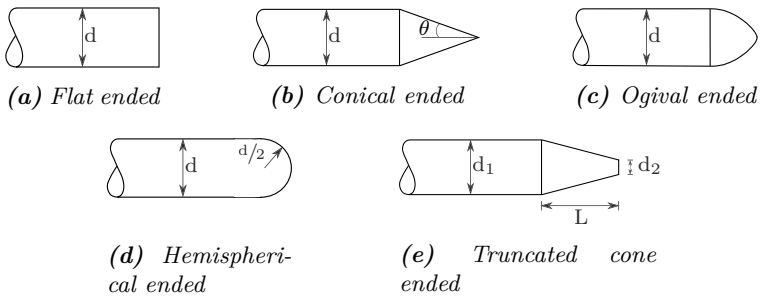

(a) *Flat ended* ***(b)*** *Conical ended* ***(c)*** *Ogival ended*

(d) *Hemispherical ended* ***(e)*** *Truncated cone ended*

Figure 2.1: *Different projectile nose shapes, adapted from Børvik [2].*

The target can be defined as any object, moving or stationary, that is struck by the projectile. Backman and Goldsmith classifies targets by its thickness in four different categories [23]:

1. Semi-infinite: No influence of the distal boundary on the penetration process.
2. Thick: The distal boundary influence the penetration process only after substantial travel into the target.
3. Intermediate: Rear surface exerts considerable influence on the deformation process during nearly all of the penetrator motion.
4. Thin: Nonexisting stress and deformation gradients throughout the target thickness.

Penetration is defined as the entry of a projectile into any region of a target [2]. As mentioned earlier in this section, several factors may affect the penetration and fracture process, and hence result in different failure modes for the target material. The failure mechanisms are highly dependent on variables such as the projectile impact velocity, material properties and relative dimensions of projectile and target, as well as the target support. The target impact response can be divided into non-perforating and perforating failure modes, respectively. The non-perforating failure modes include elastic deformation, plastic deformation and cratering. These mechanisms do not result in complete perforation of the target, and often occur for low impact velocities. There are two types of transverse deformation caused by plastic deformation for thin plates; bulging and dishing. Bulging is referred to as deformation that conforms with the procetile nose, while dishing is bending of the plate caused by the impact. These two deformation modes become less significant for thicker plates, where cratering is the dominant failure mode.

Perforating failure modes occur in thin and intermediate plates where the impact velocity is above a critical velocity, determined by the target material and geometry. The most frequent fracture modes for thin and intermediate plates are illustrated in Figure 2.2, adapted from Backman and Goldsmith [23]. These failure modes often have one dominant failure mechanism, but may be a combination of several modes. The reader is referred to Børvik [2] for further information regarding the perforating failure modes.

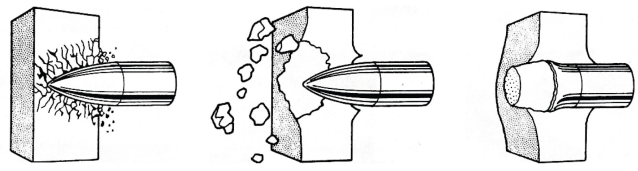

(a) *Brittle fracture* ***(b)*** *Fragmentation* ***(c)*** *Plugging*

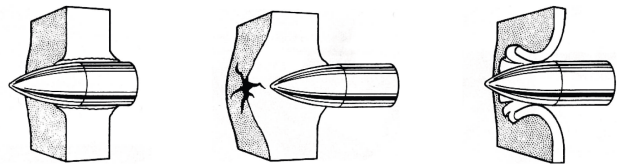

(d) *Ductile hole growth* ***(e)*** *Radial fracture* ***(f)*** *Petalling*

Figure 2.2: *Common failure modes in impacted target plates, adapted from Backman and Goldsmith [23].*

Although several factors affect the ballistic impact process, the impact velocity is considered the predominant factor. Backman and Goldsmith [23] classified the impact velocities in the following regimes:

1. Low velocity regime (0-50 $^{m}/_{s}$): Elastic and plastic bending controls the deformation.

2. Sub-ordnance velocity regime (50-500 $^{m}/_{s}$): Hard projectiles behave elastically and the target response is primarily plastic.

3. Ordnance velocity regime (500-1300 $^{m}/_{s}$): The material strength is an important parameter, but the density gets gradually more important with increasing velocity. This range is particularly interesting for military applications.

4. Ultra-ordnace velocity regime (1300-3000 $^{m}/_{s}$): The materials often behave like fluids, hence a hydrodynamic description of the material behaviour is necessary. The material density is a dominant parameter.

5. Hypervelocity regime (>3000 $^{m}/_{s}$): Both projectile and target behave like fluids, and the material strength is no longer important.

Our problem operates with velocities in the sub-ordnance and ordnance regimes.

2.1.2 Ballistic Limit Velocity

The ballistic limit velocity, v_{bl}, is defined as the maximum velocity a projectile can have for a given target to be able to withstand complete penetration. The ballistic limit velocity can be estimated as the average of the highest velocity that only gives partial penetration, and the lowest velocity that yields complete perforation.

Figure 2.3 illustrates a typical ballistic limit curve, limit velocity and limit line for a penetration process of a thin plate. The ballistic limit curve is obtained by plotting the initial/impact velocity against the residual velocity, and drawing a continuous line between the points. This is often compared with the ballistic limit line, which represents the ballistic limit curve for a target with zero thickness.

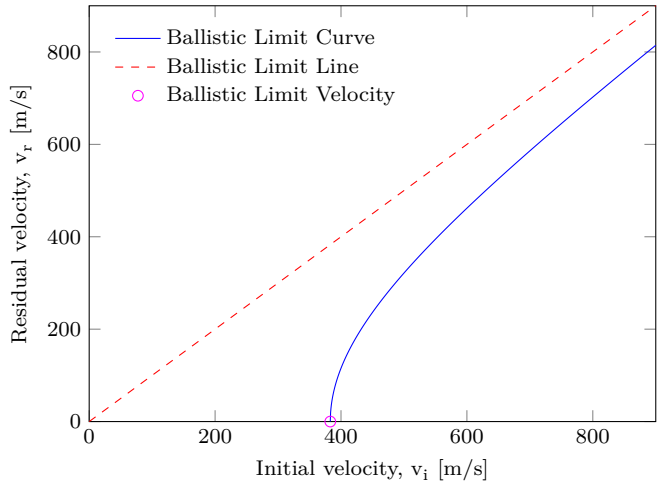

Figure 2.3: *Ballistic limit curve, ballistic limit velocity and ballistic limit line.*

2.1.3 The Recht-Ipson Model

Recht and Ipson [24] proposed a model for the relationship between impact and residual velocities in 1963. The model is based on the concepts of energy and momentum conservation, and includes the ballistic limit. The energy balance yields

$$\frac{1}{2}m_p v_i^2 = \frac{1}{2}m_p v_r^2 + D \tag{2.1}$$

where v_i is the impact velocity, v_r is the residual velocity, m_p is the mass of the projectile and D is the dissipated energy in the impact. Further in this derivation an ogival or conical projectile is assumed. These projectiles are assumed to yield ductile hole growth, hence no fragmentation. Setting the impact velocity equal to the ballistic limit velocity, v_{bl}, and the residual velocity equal to zero Equation 2.1 yields

$$D = \frac{1}{2}m_p v_{bl}^2 \tag{2.2}$$

Assuming D constant for impact velocities different from the ballistic limit velocity, inserting Equation 2.2 into Equation 2.1 and rearranging yields the Recht-Ipson model for ogival and conical projectiles.

$$v_r = (v_i^2 - v_{bl}^2)^{\frac{1}{2}} \tag{2.3}$$

A modified version of the Recht-Ipson model was established by Lambert and Jonas [22], and is given as

$$v_r = a(v_i^p - v_{bl}^p)^{\frac{1}{p}} \tag{2.4}$$

where a and p are constants.

2.2 Materials Mechanics

In this section, some fundamental theories of mechanics of materials is presented. First, a few sections are dedicated to experimental measures and stress invariants. Further, two sections are devoted to ductile fracture and damage mechanics, respectively. Lastly, an overview of three different fracture models used in this thesis is presented. Most of this section is based on Hopperstad and Børvik [25].

2.2.1 Experimental Measures

To analyse data obtained from tensile tests, the Cauchy stress and logarithmic strain need to be calculated. The Cauchy stress, σ, and logarithmic strain, ε_l, are defined as

$$\sigma = \frac{F}{A}, \qquad \varepsilon_l = \ln \frac{A_0}{A} \tag{2.5}$$

where F is the force, A_0 is the initial cross-sectional area and A is the current cross-sectional area of the gauge section of the given test specimen. Small elastic strains are assumed, hence the tensile test is presumed to be isochoric. This thesis focuses only on smooth specimens with circular cross sections, cf. Section 3.2.1, hence the current area is assumed to be elliptical. The area is calculated by using the following definitions

$$A_0 = \frac{\pi}{4} D_0^2, \qquad A = \frac{\pi}{4} D_1 D_2 \tag{2.6}$$

where D_0 is the initial diameter of the gauge section and $D_{1,2}$ are measured diameters in perpendicular directions. Plastic strain is calculated by using the following expression

$$\varepsilon^p = \varepsilon - \frac{\sigma}{E} \tag{2.7}$$

where ε is the total strain and E is Young's modulus. After necking occurs, there is no longer a uniaxial stress state in the test specimen, i.e., the true stress is not equal to the equivalent stress after the point of necking. The equivalent stress after necking can be calculated by using the Bridgman correction

$$\sigma_{eq} = \frac{\sigma_t}{(1 + 2\frac{R}{a})[\ln(1 + \frac{a}{2R})]} \tag{2.8}$$

where a is the specimen radius at the neck and R is the neck radius. Note that a number of assumptions have been made to obtain the expression in Equation 2.8. The reader is referred to Bridgman [26] for further information. An empirical expression for the ratio $^a/_R$ was proposed by Le Roy et al. [27]

$$\frac{a}{R} = 1.1(\varepsilon^p - \varepsilon_u), \qquad \varepsilon^p > \varepsilon_u \tag{2.9}$$

where ε_u is the equivalent plastic strain at necking.

2.2.2 Stress Invariants

For an isotropic material the following three stress invariants are important for describing the stress state; the von Mises stress σ_{VM}, stress triaxiality ratio σ^* and the Lode angle θ_L. These invariants are defined in this section, and used later in the derivations of the Cockcroft-Latham (CL) and Johnson-Cook (JC) fracture models presented in Sections 2.2.6.1 and 2.2.6.2, respectively. The stress tensor can be divided into a deviatoric and a hydrostatic part

$$\sigma_{ij} = \sigma_{ij}^{'} + \sigma_H \delta_{ij}, \qquad \sigma_H = \frac{1}{3}\sigma_{kk} = \frac{1}{3}(\sigma_I + \sigma_{II} + \sigma_{III}) \tag{2.10}$$

where $\sigma_I \geq \sigma_{II} \geq \sigma_{III}$ are the ordered principal stresses. From the deviatoric part of the stress tensor the von Mises stress can be defined as

$$\sigma_{VM} \equiv \sqrt{3J_2} = \sqrt{\frac{3}{2}\sigma_{ij}^{'}\sigma_{ij}^{'}} \tag{2.11}$$

where J_2, the second principal invariant of the deviatoric stress tensor $\boldsymbol{\sigma}^{'}$, can be expressed as

$$J_2 = \frac{1}{2}\sigma_{ij}^{'}\sigma_{ij}^{'} = \frac{1}{2}\left[(\sigma_I - \sigma_H)^2 + (\sigma_{II} - \sigma_H)^2 + (\sigma_{III} - \sigma_H)^2\right] \tag{2.12}$$

The stress triaxiality σ^* is a non-dimensional parameter describing the ratio between the hydrostatic and the von Mises stress, defined as

$$\sigma^* \equiv \frac{I_\sigma}{3\sqrt{3J_2}} = \frac{\sigma_H}{\sigma_{VM}} \tag{2.13}$$

Figure 2.4 illustrates the Lode angle θ_L in the Π-plane in the Haigh-Westergaard space. The angle is defined as

$$cos(3\theta_L) \equiv \frac{J_3}{2\sqrt{(J_2/3)^3}} \tag{2.14}$$

where J_3 represents the third principal invariant of the deviatoric stress tensor $\boldsymbol{\sigma}^{'}$. Hopperstad and Børvik [25] defines the Lode angle in the range from $0 < \theta_L < \frac{\pi}{3}$, while others like Gao and Kim [19] use the range $-\frac{\pi}{6} < \theta_L < \frac{\pi}{6}$. In this thesis we have chosen the former definition.

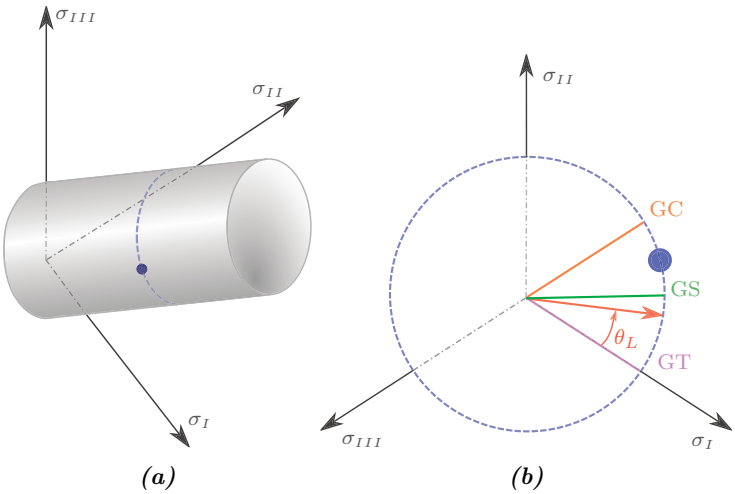

Figure 2.4: *(a) von Mises yield surface and (b) identification of generalized tension (GT), generalized shear (GS), generalized compression (GC) and the Lode angle (θ_L) in the* Π*-plane in the Haigh-Westergaard space, adapted from Hopperstad and Børvik [25].*

2.2.3 Ductile Fracture

Anderson [28] characterises the ductile fracture process of metals by the following three stages:

1. Formation of a free surface at an inclusion or second-phase particle by either interface decohesion or particle cracking.
2. Growth of the void around the particle, by means of plastic strain and hydrostatic stress.
3. Coalescence of the growing void with adjacent voids.

Figure 2.5 illustrates the complete process of ductile fracture, as described above. The formation of micro voids, cf. Figures 2.5(a) and 2.5(b), occur when the interfacial bonds between the particle and the matrix break. In order to achieve this, a sufficient amount of stress must be applied. The critical step in ductile fracture is determined by the amount of stress needed to break these interfacial bonds. If the bonds are strong, a high amount of stress is needed for void nucleation and fracture will occur shortly after the voids form. Weak interfacial bonds, on the other hand, will result in fracture properties that are controlled by growth and coalescence of voids. Note that voids may be present in the initial material.

Once voids have been formed, hydrostatic stress and further plastic straining cause void growth and coalescence of adjacent voids. Coalescence takes place when neighbouring voids join together and form macro-cracks in the material. It is considered a precursor for failure, i.e., when the material suffers a total loss of load-carrying capacity [25]. These

steps are shown in Figures 2.5(c)-2.5(f). Note that the orientation of the fracture path is dependent on the stress state [28].

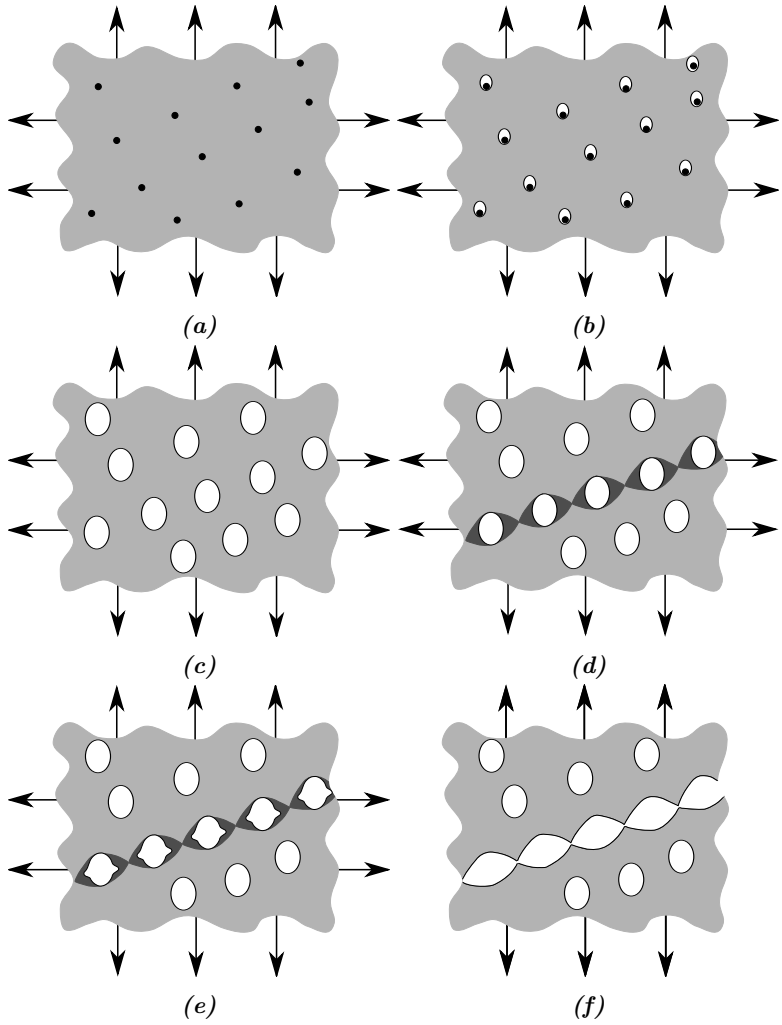

Figure 2.5: *Void nucleation, growth and coalescence in ductile metals: (a) inclusions in a ductile matrix, (b) void nucleation, (c) void growth, (d) strain localization between voids, (e) necking between voids , and (f) void coalescence and fracture. Adapted from Anderson [28].*

2.2.4 Damage Mechanics

Ductile fracture models should contain a criterion for void nucleation, an evolution equation for void growth and a criterion for void coalescence [29]. In damage mechanics the damage parameter ω is introduced in the strain energy function for the elastic-plastic

model as

$$U_0(\boldsymbol{\varepsilon}^e, \omega) = (1-\omega)\frac{1}{2}\varepsilon^e_{ij} C_{ijkl} \varepsilon^e_{kl} \tag{2.15}$$

where the strain tensor $\boldsymbol{\varepsilon}$ is divided into an elastic part $\boldsymbol{\varepsilon}^e$ and a plastic part $\boldsymbol{\varepsilon}^p$, and $\boldsymbol{C}$ is the 4^{th} order tensor of elastic constants. The Cauchy stress tensor $\boldsymbol{\sigma}$ can then be derived from the strain energy function as

$$\sigma_{ij} = \frac{\partial U_0}{\partial \varepsilon^e_{ij}} = (1-\omega) C_{ijkl} \varepsilon^e_{kl} \tag{2.16}$$

The effective stress tensor $\widetilde{\boldsymbol{\sigma}}$ acting on the hypothetical undamaged part of the material can be expressed as

$$\widetilde{\sigma}_{ij} = \frac{\sigma_{ij}}{1-\omega} = C_{ijkl} \varepsilon^e_{kl} \tag{2.17}$$

The yield function is defined as for rate independent plasticity without damage, but instead of the Cauchy stress tensor, the effective stress tensor is now applied such that

$$f(\widetilde{\boldsymbol{\sigma}}, R) = \varphi(\widetilde{\boldsymbol{\sigma}}) - (\sigma_0 + R(p)) \leq 0 \tag{2.18}$$

where σ_0 is the initial yield stress and R the isotropic hardening variable depending on the accumulated plastic strain, p. For a Voce hardening rule with two terms $R(p)$ can be expressed as

$$R(p) = \sum_{i=1}^{2} Q_i (1 - e^{-C_i p}) \tag{2.19}$$

where Q_1, Q_2, C_1 and C_2 are material constants. The effective equivalent stress is given as

$$\widetilde{\sigma}_{eq} = \varphi(\widetilde{\boldsymbol{\sigma}}) = \frac{\varphi(\boldsymbol{\sigma})}{1-\omega} = \frac{\sigma_{eq}}{1-\omega} \tag{2.20}$$

By applying the von Mises yield criterion the effective equivalent stress can be expressed as presented in Equation 2.20, where $\sigma_{eq} = \sigma_{VM}$, as defined in Equation 2.11. The equivalent stress is conjugate in plastic power to the accumulated plastic strain, such that $\sigma_{ij}\dot{\varepsilon}^p_{ij} = \sigma_{eq}\dot{p}$. Implementing an associated flow rule, the plastic strain rate can be expressed as

$$\dot{\varepsilon}^p_{ij} = \dot{\lambda}\frac{\partial f(\widetilde{\boldsymbol{\sigma}}, R)}{\partial \sigma_{ij}} = \frac{\dot{\lambda}}{1-\omega}\frac{\partial f(\widetilde{\boldsymbol{\sigma}}, R)}{\partial \widetilde{\sigma}_{ij}} \tag{2.21}$$

where the plastic multiplier $\dot{\lambda} \geq 0$ is related to the accumulated plastic strain as

$$p = \int \frac{\dot{\lambda}}{1-\omega} dt \tag{2.22}$$

In order to describe how the damage parameter evolves, a damage evolution rule needs to be defined

$$\dot{\omega} = \begin{cases} 0 & \text{if } p \leq p_0 \\ H_\omega \dot{p} & \text{if } p > p_0 \end{cases}$$

where H_ω is the damage modulus and p_0 is a characteristic strain where damage starts to evolve. When the damage parameter reaches a critical value $\omega_c \leq 1$ the material is assumed to fail. The damage modulus H_ω is often dependent on the effective stress tensor $\widetilde{\boldsymbol{\sigma}}$ seen in the following sections.

When studying ductile fracture, one can choose between a coupled and an uncoupled approach. In an uncoupled damage model, it is assumed that damage has a negligible effect on the elastic-plastic constitutive equations, i.e., the yield condition, the plastic flow and the strain hardening of the material.

For uncoupled models, the damage parameter ω is neglected, ergo set to zero in Equations 2.15-2.22. In practice, this implies that no damage occurs in the material prior to fracture. Coupled damage models, on the other hand, account for material damage evolution prior to fracture. The coupled models are assumed to be more accurate than the uncoupled, but the identification of parameters from test data is more troublesome.

Section 2.2.6 presents two different uncoupled damage models, the Cockcroft-Latham and Johnson-Cook fracture models. Further, a coupled model, the Gurson-Tvergaard-Needleman (GTN) model, is described in Section 2.2.7.

2.2.5 Johnson-Cook Material Model

In 1983, Johnson and Cook [30] proposed a model for the von Mises flow stress expressed as

$$\sigma_{eq} = [A + Bp^n]\,[1 + C\ln\dot{p}^*]\,[1 - T^{*m}] \tag{2.23}$$

$$\dot{p}^* = \frac{\dot{p}}{\dot{p}_0}, \qquad T^* = \frac{T - T_0}{T_m - T_0}$$

where $\dot{p}^*$ is the dimensionless plastic strain rate obtained from the plastic strain rate $\dot{p}$ and a reference plastic strain rate $\dot{p}_0$. A, B, C, m and n are material constants. The homologous temperature T^* is given by the current temperature T, the melting temperature T_m and the ambient temperature T_0. Assuming adiabatic conditions, high plastic strain rates in the material yield an increase in temperature. This increase can be calculated as

$$\Delta T = \int_0^p \chi \frac{\sigma_{eq} dp}{\rho C_p} \tag{2.24}$$

where ρ is the material density, C_p is the specific heat capacity at constant pressure and χ is the Taylor-Quinney empirical coefficient that is often assigned the value 0.9 [31].

To avoid undesirable effects if $\dot{p} < 1$, Camacho and Ortiz [32] proposed a modification of the strain rate term in the JC model (MJC) [31].

$$\sigma_{eq} = [A + Bp^n]\,[1 + \dot{p}^*]^C\,[1 - T^{*m}] \tag{2.25}$$

As seen in Equation 2.25, the strain hardening is found using the Power law. The Voce hardening law has proved better for describing the material behaviour for aluminium [33].

By substituting the Voce hardening law presented in Equation 2.19 into Equation 2.25 one obtains the final expression for the MJC model

$$\sigma_{eq} = \left[A + \sum_{i=1}^{j} Q_i (1 - e^{-C_i p}) \right] [1 + \dot{p}^*]^C [1 - T^{*m}] \tag{2.26}$$

where j corresponds to the total number of Voce terms, and Q_i and C_i are Voce hardening parameters. In this thesis, we have used $j = 2$.

2.2.6 Fracture Models

When analysing the response of stuctures that exhibit large plastic deformations, a fracture criterion is needed to accurately describe the material behaviour. This section describes two different uncoupled models for material failure; the Cockcroft-Latham and Johnson-Cook fracture models.

2.2.6.1 Cockcroft-Latham Fracture Model

A phenomenological ductile fracture criterion was proposed by Cockcroft and Latham [20] in 1968. This one-parameter criterion states that the damage parameter depends on plastic straining, stress triaxiality and the Lode angle, through the maximum principal stress.

The Cockcroft-Latham criterion is given by

$$\omega = \frac{1}{W_c} \int_0^p \langle \sigma_I \rangle dp \tag{2.27}$$

where W_c is a material constant that represents the "plastic work" needed to reach failure and σ_I is the maximum principal stress. $\langle \sigma_I \rangle$ is defined as

$$\langle \sigma_I \rangle = \begin{cases} \sigma_I & \text{if } \sigma_I > 0 \\ 0 & \text{if } \sigma_I \leq 0 \end{cases}$$

Fracture is assumed to occur when the dimensionless damage variable, ω, equals unity. The real plastic work is calculated from the equivalent stress, but as stated, the CL-criterion is based on the maximum principal stress, hence the quotation marks. The first prinicpal stress can be expressed in terms of the triaxiality and Lode parameter as follows

$$\sigma_I = \left(\sigma^* + \frac{3 - \mu_\sigma}{3\sqrt{3 + \mu_\sigma^2}} \right) \sigma_{eq} \tag{2.28}$$

where σ_{eq} equals the von Mises stress, σ_{VM}, and the Lode parameter is defined as

$$\mu_\sigma = \sqrt{3} \tan\left(\theta_L - \frac{\pi}{6}\right) = \frac{2\sigma_{II} - \sigma_I - \sigma_{III}}{\sigma_I - \sigma_{III}} \tag{2.29}$$

From Equation 2.29, we obtain the following values for the Lode parameter for three generalized stress states

$$\mu_\sigma = \begin{cases} +1 & \text{Generalized compression, } \sigma_I = \sigma_{II} \\ 0 & \text{Generalized shear} \\ -1 & \text{Generalized tension, } \sigma_{II} = \sigma_{III} \end{cases}$$

By inserting the expression in Equation 2.28 into Equation 2.27, and assuming $\sigma_I \geq 0$, we get the following

$$\omega = \frac{1}{W_c} \int_0^p \left(\sigma^* + \frac{3 - \mu_\sigma}{3\sqrt{3 + \mu_\sigma^2}} \right) \sigma_{eq} dp \tag{2.30}$$

It is seen from Equation 2.30 that the CL-criterion depends on both the flow stress of the material, the Lode parameter, the accumulated plastic strain and the stress triaxiality [29]. As stated earlier in this chapter, fracture occurs at certain critical values of the "plastic work" W_c and plastic strain p_f, that yield $\omega = 1$. The CL-criterion at fracture can be expressed as

$$\omega = \frac{1}{W_c} \int_0^{p_f} (\sigma^* + \bar{\mu}) \cdot (\sigma_0 + R(p))\, dp = 1 \tag{2.31}$$

where p_f is the plastic strain at fracture, σ_0 is the yield stress of the material and $R(p)$ a work-hardening rule that is a function of the accumulated plastic strain. By using the Voce hardening rule with two terms, and rearranging the expression in Equation 2.31, we obtain the following expression for the relation between the stress triaxiality and plastic strain at failure

$$\sigma^* = \frac{W_c}{H} - \bar{\mu}, \qquad \bar{\mu} = \frac{3 - \mu_\sigma}{3\sqrt{3 + \mu_\sigma^2}} \tag{2.32}$$

where H is given as

$$H = \sigma_0 p_f + \sum_{i=1}^{2} \left(Q_i p_f + \frac{Q_i}{C_i} (e^{-C_i p_f} + 1) \right) \tag{2.33}$$

2.2.6.2 Johnson-Cook Fracture Model

Johnson and Cook [21] proposed an uncoupled fracture model that accounts for the effects of temperature and plastic strain rate [25]. As for the CL-criterion, fracture is assumed to occur when the damage variable ω equals unity. The damage variable is defined as follows for the Johnson-Cook fracture model

$$\omega = \int_0^p \frac{1}{p_f} dp \tag{2.34}$$

where the fracture strain p_f is defined for stress paths that have constant values for the Lode angle and stress triaxiality, given an existing fracture surface. By introducing the

Lode angle in the original JC fracture model [21], we obtain the extended JC fracture model

$$p_f(\sigma^*, \theta_L, \dot{p}, T) = [D_1 + D_2 \exp(D_3\sigma^*)]\,(1 + D_4 \ln \dot{p}^*)\,(1 + D_5 T^*)\,[1 - D_6\kappa(\theta_L)] \quad (2.35)$$

where D_1,D_2,...,D_6 are model constants. κ is a stress-dependent parameter defined as

$$\kappa(\theta_L) \equiv 1 - \cos^2(3\theta_L), \qquad 0 \leq \theta_L \leq \frac{\pi}{3} \quad (2.36)$$

From Equation 2.36 it is seen that $\kappa \in [0, 1]$, where $\kappa = 0$ represents all axisymmetric stress states and $\kappa \neq 0$ all other stress states with a combination of hydrostatic and shear stresses. The κ parameter was introduced by Nahshon and Huctchinson [18] regarding shearing of voids in the coupled Gurson model. This modification of the GTN model is presented in Section 2.2.7.2.

For a problem independent of both the plastic strain rate $\dot{p}^*$ and the temperature T^*, the corresponding model constants D_4 and D_5 are equal to zero. The relationship between the Lode parameter and the Lode angle is given by Equation 2.29, and by using this we can rewrite κ in terms of the Lode parameter as

$$\kappa(\mu_\sigma) = 1 - \cos^2\left(3\arctan\left(\frac{\mu_\sigma}{\sqrt{3}}\right) + \frac{\pi}{2}\right) \quad (2.37)$$

By using the relation presented in Equation 2.37, Equation 2.35 can be written as

$$p_f(\sigma^*, \mu_\sigma) = (D_1 + D_2 \exp(D_3\sigma^*))\left[1 - D_6\left(1 - \cos^2\left(3\arctan\left(\frac{\mu_\sigma}{\sqrt{3}}\right) + \frac{\pi}{2}\right)\right)\right] \quad (2.38)$$

2.2.7 Porous Plasticity

Ductile fracture is, as mentioned in Section 2.2.3, characterized by three stages; nucleation, growth and coalescence of voids and micro-cracks. "In porous plasticity models, a macroscopic material element is assumed to consist of a matrix material and voids" [25]. Porous metals are characterised by pressure sensitivity and compressible plastic flow. Both volumetric and deviatoric plastic strains develop under straining, and due to occurring work-hardening under void growth and nucleation there is a continuous competition between isotropic work-hardening of the matrix and softening due to nucleation and growth of voids [25]. Note that in a coupled damage model such as the Gurson-Tvergaard-Needleman model presented in Section 2.2.7.1, the damage parameter is directly coupled to the volume fraction of voids, i.e., $\omega = f$.

2.2.7.1 The Gurson-Tvergaard-Needleman Model

Gurson [16] developed in 1977 a porous plasticity model based on micro-mechanics of voided materials, that was later modified by Tvergaard and Needleman [9, 10, 17]. The

Gurson-Tvergaard-Needleman (GTN) extension is valid for metallic materials that is considered to be porous and isotropic. The yield function is defined as

$$f(\boldsymbol{\sigma}, \omega, \sigma_{_M}) = \frac{\sigma_{eq}^2}{\sigma_{_M}^2} + 2\omega q_1 \cosh\left(\frac{q_2\sigma_{kk}}{2\sigma_{_M}}\right) - 1 - (\omega q_1)^2 \leq 0 \tag{2.39}$$

where q_1 and q_2 are material constants, typically $q_1 = 1.5$ and $q_2 = 1.0$ [17], ω is the void volume fraction, $\sigma_{_M}$ is the flow stress of the matrix material and $\sigma_{eq} = \sqrt{\frac{3}{2}\sigma'_{ij}\sigma'_{ij}}$ is the equivalent macroscopic Cauchy stress. It is easily seen that when $\omega = 1/q_1$, the yield surface, expressed by Equation 2.39, collapse to a single point. The material then lose all its load carrying capacity. The original Gurson model is obtained when $q_1 = q_2 = 1$.

By assuming associated plastic flow, the plastic strain rate can be divided into volumetric and deviatoric parts as follows

$$\dot{\varepsilon}_{ij}^p = \dot{\lambda}\frac{\partial f}{\partial \sigma_{ij}} = \dot{\lambda}\left(\frac{3}{\sigma_{_M}^2}\sigma'_{ij} + \frac{\omega q_1 q_2}{\sigma_{_M}}\sinh\left(\frac{q_2\sigma_{kk}}{2\sigma_{_M}}\right)\delta_{ij}\right) \tag{2.40}$$

where the first term on the right-hand side represents the deviatoric part and the second term the volumetric part. Note that for the GTN model, the yield function is *not* a homogeneous function of order one, and hence the plastic multiplier, $\dot{\lambda}$, is not dimensionless.

As described in Section 2.2.3, hydrostatic stress and plastic straining cause void nucleation and growth. The change of the void volume fraction can be expressed as

$$\dot{\omega} = \dot{\omega}_n + \dot{\omega}_g \cong \dot{\omega}_g \tag{2.41}$$

where $\dot{\omega}_n$ and $\dot{\omega}_g$ represent void nucleation and growth, respectively. In this thesis the statistical nucleation term in Equation 2.41 was neglected, i.e., it was assumed that all change in void volume fraction was due to growth of existing voids. The reader is referred to Hopperstad and Børvik [25] and Benzerga and Leblond [13] for further information regarding the nucleation term.

The void growth equation, using the assumption in Equation 2.41, is given as

$$\dot{\omega} \cong \dot{\omega}_g = \dot{\lambda}\,(1-\omega)\,\frac{3\omega q_1 q_2}{\sigma_{_M}}\sinh\left(\frac{q_2\sigma_{kk}}{2\sigma_{_M}}\right) \tag{2.42}$$

A simple fracture criterion for the GTN model is that fracture initiates at a critical value of the void volume fraction, i.e., $\omega = \omega_{_C}$. For $\omega > \omega_{_C}$, a modified void volume fraction is often used to simulate rapid loss of strength in the final stages of void coalescence. This rapid loss of stress carrying capacity can be expressed in terms of an effective void volume fraction, defined by Tvergaard and Needleman [17], as

$$\omega^*(\omega) = \begin{cases} \omega & \text{for } \omega \leq \omega_{_C} \\ \omega_{_C} + \frac{\omega_{_U} - \omega_{_C}}{\omega_{_F} - \omega_{_C}}\,(\omega - \omega_{_C}) & \text{for } \omega > \omega_{_C} \end{cases}$$

where $\omega_{_U} = 1/q_1$ and $\omega^*(\omega_{_F}) = \omega_{_U}$. $\omega_{_F}$ represents the void volume fraction where the material has completely lost its load-carrying capacity.

2.2.7.2 The Modified Gurson Model with Softening in Shear

To properly describe damage evolution for low triaxialities, such as shear-dominated stress states, Nahshon and Hutchinson [18] proposed an extension of the Gurson model that accounts for shear softening due to void distortion and inter-void linking. The void growth equation for the modified Gurson model is expressed as

$$\dot{\omega} = \dot{\omega}_n + \dot{\omega}_g + \dot{\omega}_s \cong \dot{\omega}_g + \dot{\omega}_s \tag{2.43}$$

The evolution of shear damage ω_s defined as

$$\dot{\omega}_s = k_s \omega \kappa(\theta_L) \frac{\sigma'_{ij} \dot{\varepsilon}^p_{ij}}{\sigma_{eq}} \tag{2.44}$$

where k_s is a constant and κ is defined as in Equation 2.36. Note that for the modified Gurson model the damage variable accounts for softening of the material due to void distortion and growth, ergo $\omega \neq f$.

2.3 Micromechanical Computational Cells

As presented in Section 2.2.3, the ductile fracture process goes through three defined stages where growth of voids and coalescence are essential parts. One way of calibrating the fracture models presented in Sections 2.2.6.1 and 2.2.6.2 is to use micromechanical computational unit cells. The cells can also be used for calibrating void growth models such as the GTN model, presented in Sections 2.2.7.1 and 2.2.7.2.

The computational cells illustrated in Figure 2.6 are microscopic cells the macroscopic continuum is composed of. Each cell represents a characteristic volume element. The cell is composed of a single void or particle, and a surrounding ductile matrix. The microscopic cell boundaries must be constrained to remain straight during deformation, such that the cells fit together in an array.

2.3.1 Macroscopic versus Microscopic

The microscopic cell matrix is subjected to macroscopic stresses and strains, denoted by capital Greek letters in this section. The von Mises equivalent stress defined in Section 2.2.2 can now be written in terms of the macroscopic quantities as

$$\Sigma_{eq} = \sqrt{\frac{1}{2}\Big[(\Sigma_{11} - \Sigma_{22})^2 + (\Sigma_{22} - \Sigma_{33})^2 + (\Sigma_{33} - \Sigma_{11})^2\Big]} \tag{2.45}$$

where Σ_{11}, Σ_{22} and Σ_{33} are the stress components acting on the cell. The work conjugate equivalent von Mises strain is defined as

$$E_{eq} = \frac{2}{3}\sqrt{\frac{1}{2}\Big[(E_{11} - E_{22})^2 + (E_{22} - E_{33})^2 + (E_{33} - E_{11})^2\Big]} \tag{2.46}$$

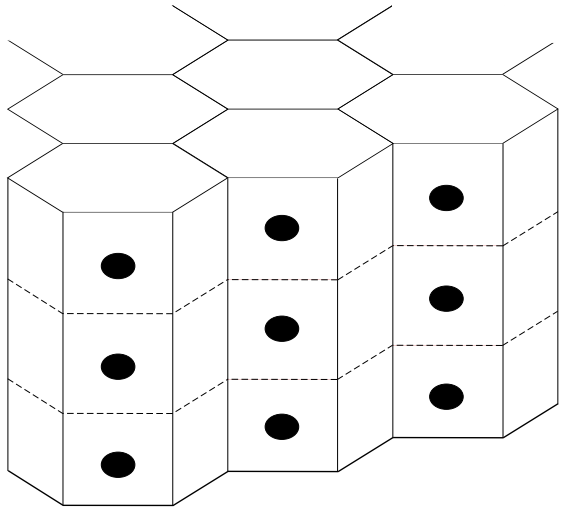

Figure 2.6: *Macroscopic continuum consisting of microscopic unit cells with a void or a particle. Adapted from Benzerga and Leblond [13].*

where E_{11}, E_{22} and E_{33} are the logarithmic strains in the principal directions. The hydrostatic or mean stress can be defined, as in Section 2.2.2, for the macroscopic stresses as

$$\Sigma_H = \frac{1}{3}(\Sigma_{11} + \Sigma_{22} + \Sigma_{33}) \tag{2.47}$$

Hence the triaxiality ratio can now be expressed as

$$\sigma^* = \frac{\Sigma_H}{\Sigma_{eq}} \tag{2.48}$$

The cell matrix is composed of an elastic-plastic material with isotropic hardening. The microscopic stresses and strains inside the cell follow a von Mises yield criterion and an associated flow rule.

2.3.2 Simplifications

The three-dimensional computational cell can be simplified in a number of ways. In this section two such simplifications are presented; the axisymmetric cell and the plane strain cell.

2.3.2.1 Axisymmetric Cell

In this section the axisymmetric computational cell is presented and important parameters defined. For the axisymmetric cell, shown in Figure 2.7, the stresses and strains in the

circumferential direction are equal to the ones in the radial direction, hence $\Sigma_{22} = \Sigma_{11}$ and $E_{22} = E_{11}$. Using this, Equations 2.45 - 2.48 can be simplified.

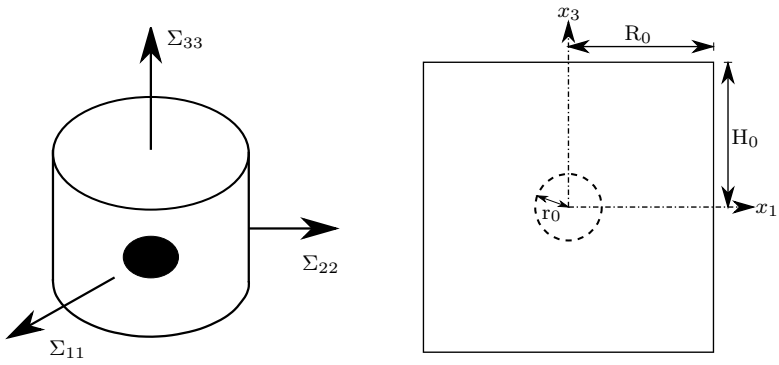

Figure 2.7: *(a) Axisymmetric unit cell and (b) geometry of the axisymmetric cell model. Adapted from Benzerga and Leblond[13].*

The equivalent strain can now be written as

$$E_{eq} = \frac{2}{3} \mid\mid E_{33} - E_{11} \mid\mid \tag{2.49}$$

where E_{11} and E_{33} are the logarithmic strains in the x_1- and x_3-directions, defined as

$$E_{11} = \ln\Big(\frac{R}{R_0}\Big), \qquad E_{33} = \ln\Big(\frac{H}{H_0}\Big) \tag{2.50}$$

The initial radius and height of the axisymmetric cell, R_0 and $2H_0$, are illustrated in Figure 2.7(b). R and $2H$ are the deformed radius and height of the cell, respectively. The equivalent von Mises stress and the hydrostatic stress simplifies to

$$\Sigma_{eq} = \mid\mid \Sigma_{33} - \Sigma_{11} \mid\mid, \qquad \Sigma_H = \frac{1}{3}\Big(\Sigma_{33} + 2\Sigma_{11}\Big) \tag{2.51}$$

Inserting this into the definition of the stress triaxiality ratio yields

$$\sigma* = \frac{\Sigma_H}{\Sigma_{eq}} = \frac{1 + 2\rho}{3 \mid\mid 1 - \rho \mid\mid}, \qquad \rho = \frac{\Sigma_{11}}{\Sigma_{33}} \tag{2.52}$$

where $\Sigma_{33} > 0$ has been assumed. For $\rho > 1$, the principal stresses will be $\Sigma_{11} = \Sigma_{22} > \Sigma_{33}$ and the Lode parameter is

$$\mu_\sigma = \frac{2\Sigma_{II} - \Sigma_I - \Sigma_{III}}{\Sigma_I - \Sigma_{III}} = \frac{2\Sigma_{11} - \Sigma_{11} - \Sigma_{33}}{\Sigma_{11} - \Sigma_{33}} = \frac{\Sigma_{11} - \Sigma_{33}}{\Sigma_{11} - \Sigma_{33}} = +1 \tag{2.53}$$

hence a generalized compression stress state. For $\rho < 1$, the principal stresses will be $\Sigma_{33} > \Sigma_{11} = \Sigma_{22}$ and the Lode parameter is

$$\mu_\sigma = \frac{2\Sigma_{II} - \Sigma_I - \Sigma_{III}}{\Sigma_I - \Sigma_{III}} = \frac{2\Sigma_{11} - \Sigma_{33} - \Sigma_{11}}{\Sigma_{33} - \Sigma_{11}} = \frac{\Sigma_{11} - \Sigma_{33}}{\Sigma_{33} - \Sigma_{11}} = -1 \tag{2.54}$$

hence a generalized tension stress state. The initial void volume fraction for the axisymmetric cell can be determined by

$$f_0 = \frac{V_{v0}}{V_0} = \frac{\frac{4\pi r_0^3}{3}}{2\pi R_0^2 H_0} = \frac{2r_0^3}{3R_0^2 H_0} \tag{2.55}$$

where V_{v0} is the initial void volume, V_0 is the total initial volume of the cell and r_0 is the initial radius of the void.

2.3.2.2 Plane Strain Cell

As for the axisymmetric cell model, this section presents important parameters for the plane strain cell model. Figure 2.8 shows the plane strain cell. Note that the void has a cylindrical shape while the shape for the axisymmetric void is spherical. For the plane strain cell, the strain in the x_2-direction is zero, and hence $E_{22} = 0$ and $\Sigma_{22} = \frac{1}{2}(\Sigma_{11} + \Sigma_{33})$. Equations 2.45 - 2.48 can again be simplified, here for the plane strain cell.

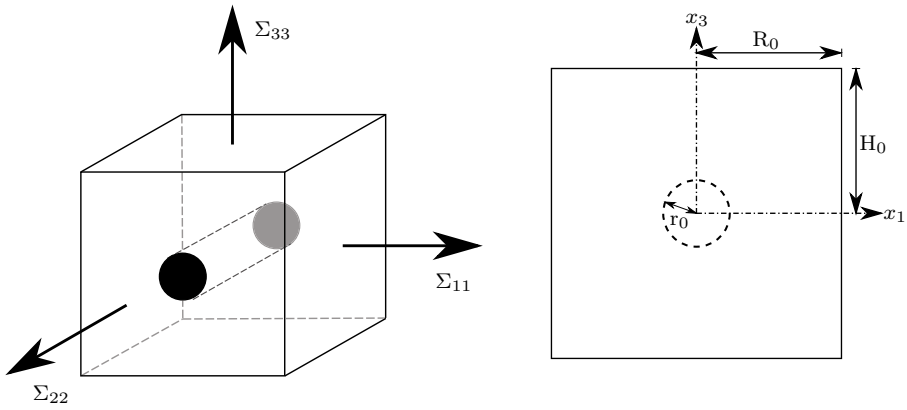

Figure 2.8: *(a) Plane strain unit cell and (b) geometry of the plane strain cell model.*

The equivalent strain simplifies to

$$E_{eq} = \frac{2}{3}\sqrt{\left(E_{33} - E_{11}\right)^2 + E_{11}E_{33}} \tag{2.56}$$

$$E_{11} = \ln\left(\frac{R}{R_0}\right), \qquad E_{33} = \ln\left(\frac{H}{H_0}\right) \tag{2.57}$$

The logarithmic strains are defined by the initial and deformed side lengths of the cell, given as $2R_0$ and $2H_0$, and 2R and 2H, respectively. The plane strain cell is illustrated in Figure 2.8(b). Again the equivalent von Mises stress and the hydrostatic stress simplifies to

$$\Sigma_{eq} = \frac{\sqrt{3}}{2} \mid\mid \Sigma_{33} - \Sigma_{11} \mid\mid, \qquad \Sigma_H = \frac{1}{2}\Big(\Sigma_{33} + \Sigma_{11}\Big) \tag{2.58}$$

Now the stress triaxiality ratio can be expressed as

$$\sigma^* = \frac{\Sigma_H}{\Sigma_{eq}} = \frac{1+\rho}{\sqrt{3} \mid\mid 1-\rho \mid\mid}, \qquad \rho = \frac{\Sigma_{11}}{\Sigma_{33}} \tag{2.59}$$

assuming $\Sigma_{33} > 0$. For $\rho \neq 1$, the Lode parameter for the plane strain cell is

$$\mu_\sigma = \frac{2\Sigma_{II} - \Sigma_I - \Sigma_{III}}{\Sigma_I - \Sigma_{III}} = \frac{(\Sigma_{11} + \Sigma_{33}) - \Sigma_{11} - \Sigma_{33}}{\Sigma_{11} - \Sigma_{33}} = \frac{0}{\Sigma_{11} - \Sigma_{33}} = 0 \tag{2.60}$$

hence a generalized shear stress state. For the plane strain cell, the initial void volume fraction can be determined from

$$f_0 = \frac{V_{v0}}{V_0} = \frac{\pi r_0^2}{4R_0H_0} \tag{2.61}$$

2.4 The Finite Element Method

The finite element method (FEM) is a numerical method used for solving boundary value problems, where non-linear finite element analysis (NFEA) can be used for solving non-linear problems. In solid mechanics, the continuum is discretized into elements where the deformation of each element can be described by interpolation functions. Cook [34] identified three different non-linearities in FEM for solid mechanics:

- Material non-linearity, in which material properties are functions of the state of stress or strain. Examples include non-linear elasticity, plasticity and creep.
- Contact non-linearity, in which a gap between adjacent parts may open or close, the contact area between parts changes as the contact force changes, or there is sliding contact with frictional forces.
- Geometric non-linearity, in which deformation is large enough that equilibrium equations must be written with respect to the deformed structural geometry. Also, loads may change direction as they increase, as when pressure inflate a membrane.

Ballistic impact is an example of an event with strong non-linearities, due to presence of material non-linearities, complex contacts and large deformations. When solving such non-linear problems, various integration methods that are classified into either implicit or explicit schemes are available. Both methods have its advantages, but for high-speed non-linear dynamic problems, explicit time integration is preferable [35]. The time-dependent equilibrium equation of solid dynamics is given as:

$$\mathbf{M}\ddot{\mathbf{D}} + \mathbf{C}\dot{\mathbf{D}} + \mathbf{R}^{\mathbf{int}} = \mathbf{R}^{\mathbf{ext}} \tag{2.62}$$

where

$\mathbf{M}$	Mass matrix
$\mathbf{C}$	Damping matrix
$\mathbf{R}^{\mathbf{int}}$	Internal forces
$\mathbf{R}^{\mathbf{ext}}$	External forces
$\ddot{\mathbf{D}}$	Acceleration
$\dot{\mathbf{D}}$	Velocity

2.4.1 Explicit Integration Methods

Explicit integration methods are used to solve the dynamic equilibrium equations (Equation 2.62) based on information that is already known, i.e., information that is directly obtained at preceding time steps. This implies that no equation solving or equilibrium iterations are needed to achieve convergence, and the computational time can be relatively low compared to implicit methods for given problems. The main disadvantage with an explicit method is that it is only conditionally stable, which requires very small time steps in order to obtain convergence.

"The time step must be small enough such that information does not propagate more than the distance between two adjacent nodes during a single time step"[35]. For a damped system, the critical time step is defined as:

$$\Delta t_{cr} \leq \frac{2}{\omega_{max}}\left(\sqrt{1-\xi^2}-\xi\right) \tag{2.63}$$

where ω_{max} is the highest natural frequency and ξ represents the damping ratio corresponding to ω_{max} of the system given in Equation 2.62. A special case of Equation 2.63, is given as

$$\Delta t_{cr} = \frac{L^e}{c_d}, \qquad c_d = \sqrt{\frac{E}{\rho}} \tag{2.64}$$

where L^e is the characteristic length of the smallest element in the FE-mesh and c_d is the dilatational wave speed given in terms of the Young's modulus and density of the material. This equation apply for a one-dimensional system without damping and with a Poisson's ratio equal to zero.

2.4.2 IMPETUS Afea Solver

"IMPETUS Afea Solver is a software package for non-linear computational mechanics. It is primarily developed to predict large deformations of structures and components exposed to extreme loading conditions" [36]. The software package is composed of several solver modules; the Finite Element module, the Discrete Particle module, the Smoothed Particle Hydrodynamics module and the WELDSIM module. The Finite Element module is primarily a non-linear explicit finite element code and is the one used in this thesis.

IMPETUS offers higher order solid elements, with no zero energy modes, that can handle large deformations. The 64-node hexahedral elements used in IMPETUS are shown in Figure 2.9.

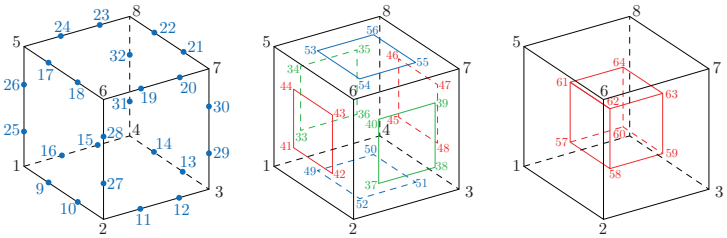

Figure 2.9: *64-node hexahedron used in IMPETUS. Adopted from Olovsson [37].*

IMPETUS has the option to select graphical processing unit (GPU) parallelization, which enables the use of thousand of threads such that relatively large analyses can be computed on a standard computer or workstation. The solver offers only penalty contact and uses a Lagrangian formulation of motion. The mesh creator is very basic, and can only create simple geometric shapes. More complex geometries need to be created with a third party software and the mesh imported to IMPETUS.

2.4.2.1 Element Erosion

Impetus offers the following four ways to deal with damage and element erosion [37]:

1. Failed element is not eroded at material failure but loses its deviatoric properties and are still able to take hydrostatic stresses.
2. Failed element is eroded at material failure.
3. Node splitting at failure (crack plane orthogonal to max principal strain).
4. Node splitting at failure (crack plane orthogonal to max principal stress).

This thesis focuses only on element erosion of 64-node hexahedra.

For erosion technique 1, the integration points successively lose their deviatoric strength when they reach the critical damage [38]. The element is not eroded before the critical time step for the element drops below a predefined value.

Concerning erosion technique 2, the element is eroded when 16 out of the 64 integration points reach the critical damage [38].

For erosion techniques 3 and 4, the nodes at the element boundary are split or divided in two to allow for crack propagation and fragmentation. The element is not eroded before the critical time step for the element drops below a predefined value.

2.4.3 SIMLab Metal Model

The Structural Impact Laboratory (SIMLab) at the Norwegian University of Science and Technology (NTNU) has over the last years developed several material models that can

be used in combination with FEA-software, such as Abaqus, LS-DYNA and IMPETUS. The SIMLab Metal Model (SMM), which is developed for metals and alloys, has been used in this thesis to describe the AlMgSi material behaviour when performing ballistic analyses with Abaqus.

The SMM is developed for use with both solid and shell elements, and is particularly useful when applying different features such as e.g. plasticity, viscoplasticity and thermo(visco)-plasticity, non-linear isotropic and kinematic hardening as well as criteria for ductile failure. It is based on several assumptions, such as; small elastic deformations, isotropic elastic behaviour and isochoric plastic deformation. The reader is referred to the SMM manual [39] for further information regarding features and assumptions.

The most important features for this thesis are adiabatic heating and criteria for ductile failure based on damage and temperature. Adiabatic heating of the material yields a temperature increase in the material that causes thermal softening. This feature was applied due to use of the JC material model, cf. Section 2.2.5, where the equivalent stress is a function of the temperature. When applying a fracture criteria, an uncoupled damage evolution was chosen, i.e., the Cockcroft-Latham fracture criteria, cf. Section 2.2.6.1.

Regarding element erosion for describing fracture and crack propagation in the material, the SMM presents three possibilities [39]:

1. Critical damage: An integration point fails when the damage variable D reaches its critical value $D_c < 1$.
2. Critical temperature: An integration point fails when the temperature reaches a critical temperature T_c.
3. Critical stress: Fracture occurs if the maximum principal stress σ_I stays larger than the critical stress σ_C during a critical time interval Δt_C.

The three fracture criteria described above can be combined, such that if one of the applied criteria is reached in an integration point, the stress tensor is set to zero and the load-carrying capacity of the integration point is gone. The element is eroded when a user-defined number of integration points of a finite element has failed. For hexahedral elements in Abaqus, the element is eroded when one integration point fails [40]. In this thesis a combination of uncoupled damage evolution and the temperature based fracture criteria was used.

3 Experimental Study

To verify the numerical results presented in Chapter 7, an experimental study of ballistic impacts was conducted with the main goal of identifying the ballistic limit curve for the target material. 7.62 mm APM2 bullets were fired into an AlMgSi target plate at multiple initial velocities. The introductory section in this chapter presents the properties of the target and bullet materials. The subsequent sections are dedicated to the tensile tests of the target material and a preliminary numerical study. Further, two sections present the experimental setup and experimental results from the ballistic impact study. Lastly, a section is devoted to investigation of the target plate's macro- and microstructure.

3.1 Target and Bullet Materials

30 mm thick plates of a homogenised aluminium alloy (AlMgSi) were used as targets during the ballistic impact experiments. The material was provided as a DC-cast (direct chilled) extrusion ingot with a diameter of 100 mm, produced at the laboratory of casting facilities at Hydro Aluminium R&D Sunndal [41]. The ingot was cut into 30 mm plates in the laboratory at the Department of Structural Engineering at NTNU. The dimensions of the target plate are shown in Figure 3.1.

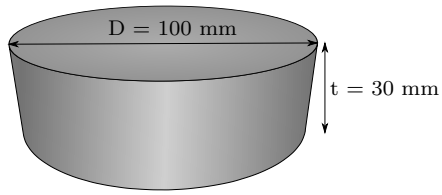

Figure 3.1: *Geometry of the AlMgSi target plate.*

Some physical constants and common model parameters, as well as the chemical composition of the AlMgSi-alloy are given in Tables 3.1 and 3.2, respectively. The homogenisation procedure, presented in Table 3.3, changed the mechanical properties of the material while maintaining the grain structure, and resulted in an approximately T4-tempered AA6060 aluminium alloy [42]. The AlMgSi-alloy is assumed to be strain rate independent at room temperature (RT), but some strain rate dependence may occur during the ballistic impacts due to high temperatures in the impact zone. This is further discussed in Section 6.1.

Table 3.1: *Physical constants and model parameters for the AlMgSi-alloy, adopted from Holmen et al. [42].*

E [MPa]	ν [-]	ρ [kg/m^3]	α [K^{-1}]	C_p [J/kgK]	$\dot{p}_0$ [s^{-1}]	c [-]	χ [-]	T_r [K]	T_m [K]	m [-]
70000	0.3	2700	$2.3 \cdot 10^{-5}$	910	$5 \cdot 10^{-4}$	0.001	0.9	293	893	1.0

Table 3.2: *Chemical composition in weight% of the AlMgSi-alloy, adopted from Westermann et al. [41].*

Fe	Mg	Si	Al
0.2	0.5	0.4	Balance

Table 3.3: *Homogenisation procedure for the AlMgSi-alloy, adopted from Westermann et al. [41].*

Heating rate [C°/h]	Holding temperature [C°]	Holding time [h]	Cooling rate to RT [C°/h]
100	585	2.5	300

Table 3.4: *Yield strength and work-hardening properties of the AlMgSi-alloy, adopted from Westermann et al. [41].*

σ_0 [MPa]	Q_1 [MPa]	C_1	Q_2 [MPa]	C_2	$\sigma_{0.2}$ [MPa]
66.26	62.00	32.36	126.46	4.21	71.21

The yield strength and work-hardening parameters for a Voce hardening rule with two terms are presented in Table 3.4, and is obtained from Westermann et al. [41]. The main reason for using this particular alloy is due to its isotropic material behaviour, which yields a clean material response that are especially beneficial when studying ductile fracture at the micro level. In addition, an isotropic material is needed for using the Gurson model in the numerical analyses.

Only the hardened steel core of the 7.62 mm APM2 bullet was used during the impact tests. It has a mass of 5 ± 0.25 g, a calibre-radius-head of 3 and a Rockwell C hardness of 63. The geometry of the hardened steel core, and the accessory parts of the APM2 bullet not used in these experiments, are presented in Figure 3.2. By using only the steel core of the bullet, a cleaner material response is ensured, such that implementation of an additional fracture criterion for the brass jacket is avoided. The reader is referred to Børvik et al. [43] for further information regarding the bullet material.

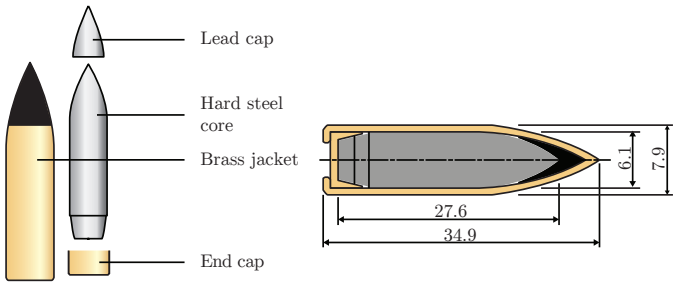

Figure 3.2: *Geometry of the 7.62 mm APM2 bullet. Adopted from Holmen et al. [42].*

3.2 Tensile Tests

3.2.1 Experimental Setup

To verify the material data given by Westermann et al. [41], tensile tests were executed at the Departement of Structural Engineering at NTNU by The Foundation for Scientific and Industrial Research (SINTEF). The geometry of the smooth test specimens is shown in Figure 3.3. Three tests were carried out at room temperature (T=293K), and all specimens were cut out from the AlMgSi extrusion ingot delivered by Hydro.

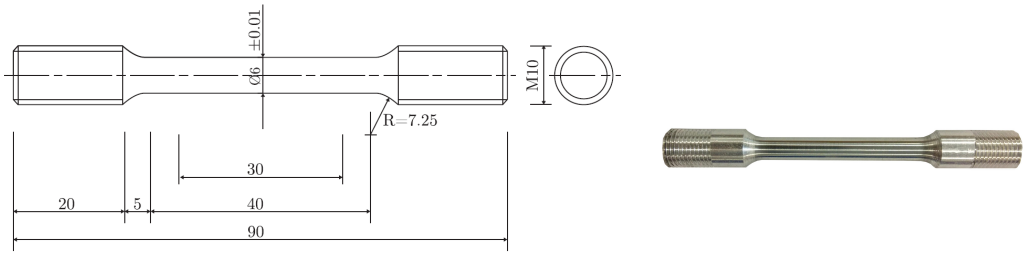

(a) *Nominal geometry. Dimensions in mm. Adopted from Westermann et al. [41]*

(b) *Actual test spciemen.*

Figure 3.3: *Tensile test specimen.*

The test specimens were mounted in a Zwick Roell Z030 - 30kN test machine. An AEROEL XLS 13XY laser micrometer was used to continously measure the diameter reduction of the specimen in two perpendicular directions during loading. These two orthogonal lasers resulted in a box of laser light of $13 \cdot 13 \cdot 0.1$ mm^3 around the minimum specimen cross section [41]. The test setup is shown in Figure 3.4. To ensure that the diameter measurements were taken at the minimum cross-sectional area, the laser micrometer was able to move vertically such that the whole specimen length could be investigated. The measured diameters from the two lasers are denoted D_1 and D_2 in this thesis, cf. Section 2.2.1. The cross-head velocity of the test machine was 1.2 $^{\text{mm}}/_{\text{min}}$,

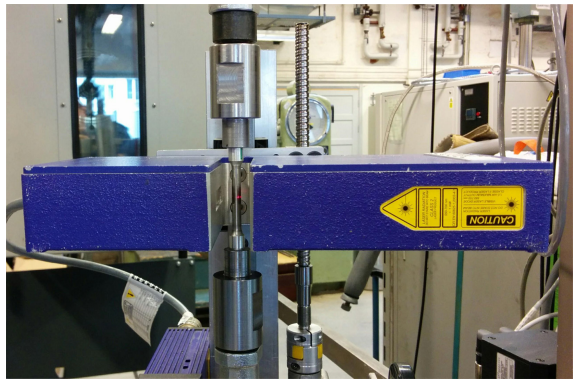

Figure 3.4: *Tensile machine with laser micrometer.*

which corresponds to a nominal strain rate of $5 \cdot 10^{-4}$ s^{-1} over the 40 mm gauge length of the specimen.

3.2.2 Experimental Results

Based on the measured diameters and the equations presented in Section 2.2.1, the equivalent stress-plastic strain curves for the three tensile tests were established. A large amount of similar tests on the same material have been conducted earlier, e.g. by Westermann et al. [41]. The results, as well as data from Westermann et al., are presented in Figures 3.5 and 3.6. Note that the curves in Figure 3.5 have been corrected using the Bridgman correction expressed in Equation 2.8.

As seen in Figure 3.6 there are large deviations between the three tests conducted for this thesis, namely tests number 1, 2 and 3. In addition the test results show bad correspondance with the data from Westermann et al., represented by tests number 4, 5 and 6, performed by SINTEF at an earlier point in time. The reason for these discrepancies is unknown. The previous tests performed on the exact same material showed negligible deviations [44]. This indicates that something did go wrong either during preparation of the test specimens or during the actual test.

The fact that there is negligible discrepancy between the earlier tests, while our tests show large deviations not only from the Westermann et al. data but also between themselves, may indicate that an error was made while preparing the specimens. A calibration error in the test machine is believed to give small discrepancies between the given tests, which was not the case. This consolidates the information given by Børvik. Based on this we have chosen to use the data from Westermann et al. [41], presented in Figure 3.5, throughout this thesis.

Figures 3.7, 3.8 and 3.9 illustrate the three test specimens after fracture. As seen in the figures, both test specimen 1 and 2 have a relatively clean shear fracture mode, while test specimen 3 exhibits a cup-and-cone type fracture. Close examination of the necking area

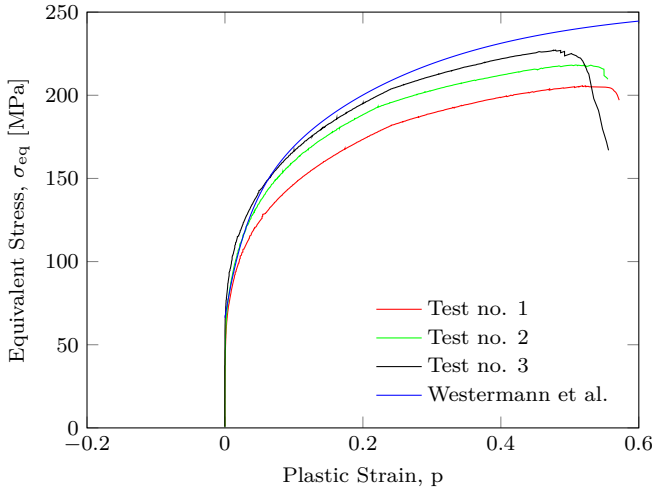

Figure 3.5: *Equivalent stress vs. plastic strain for the three tensile tests compared to the Voce curve from Westermann et al. [41].*

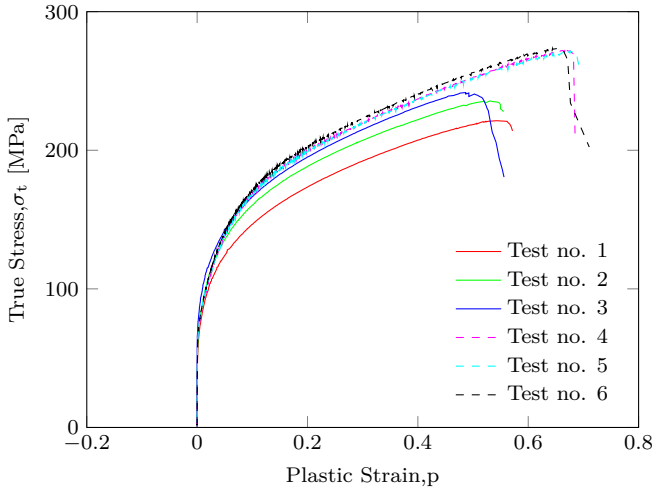

Figure 3.6: *True stress vs. plastic strain for the three tensile tests, compared with data given by Westermann et al. Tests 1, 2 and 3 represent the tests conducted for this thesis, while tests 4, 5 and 6 represent data from Westermann et al. [41].*

reveals that test 3 has less area where the surface structure of the material has changed, compared to the two other tests. The significance of this is unknown.

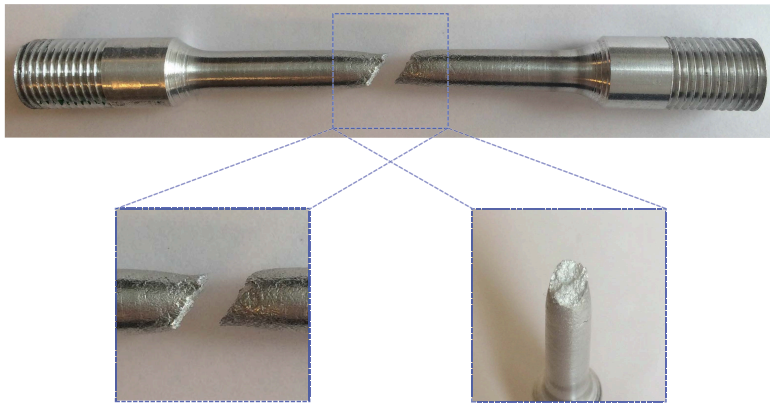

Figure 3.7: *Test specimen 1 after fracture.*

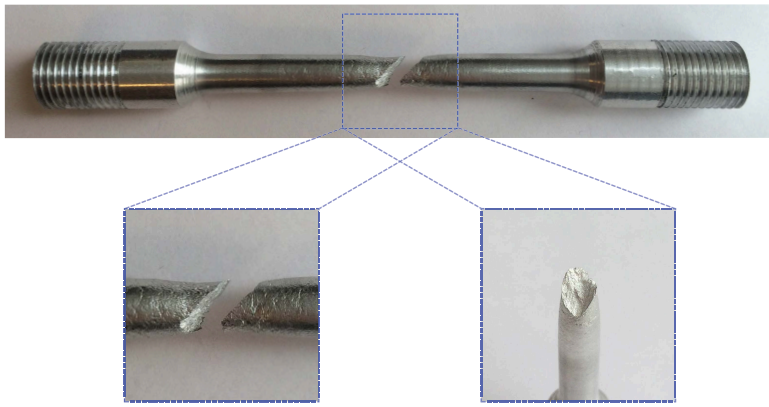

Figure 3.8: *Test specimen 2 after fracture.*

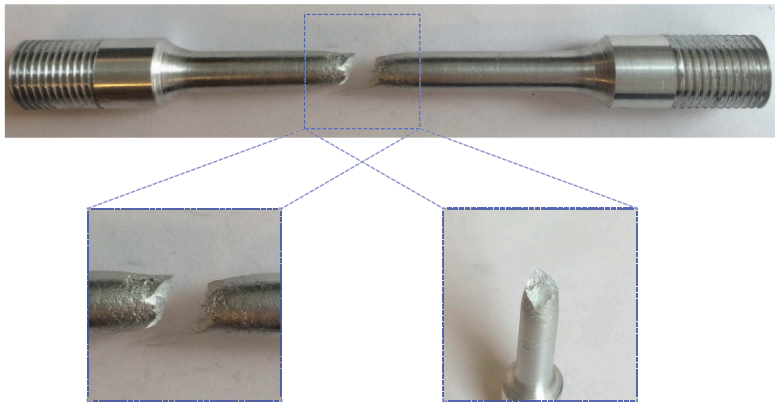

Figure 3.9: *Test specimen 3 after fracture.*

3.3 Preliminary Study

A preliminary study concerning the plate thickness was conducted due to limitations regarding both initial velocity and material. Only a certain amount of the AlMgSi-material was available, and it was therefore desirable to use as little material as possible, but still have a ballistic limit velocity within the range of the firing velocities available for this particular experimental setup. The impact velocity was adjusted such that the bullet impacted the aluminium plate at different velocities to obtain the ballistic limit of the material for various plate thicknesses.

The non-linear finite element code IMPETUS Afea Solver was used to model the ballistic impact. Only half of the bullet and target were modelled to save computational time (CPU-time), as shown in Figure 3.10. A tiny pinhole with a diameter of 1 mm was used in the target centre as a simplification, to avoid implementation of a fracture criterion this early in the study.

As seen in Figure 3.10, the regions that exhibit large plastic deformations have a finer mesh. These regions were modelled by using fully integrated third-order 64-node hexahedra, while first-order 8-node hexahedra were used for the outer region to save CPU-time. The bullet was modelled as a rigid body with density $\rho = 7850$ kg/m^3, and Figure 3.11 shows the mesh with third-order 64-node hexahedra. Figure 3.12 shows the target and bullet assembly, before and during impact.

A node-to-surface penalty contact formulation with a penalty factor of 10^{15} was implemented with the keyword `*CONTACT` in IMPETUS. The penalty factor of 10^{15} leads to a contact pressure of 1 GPa if the penetration is 0.001 mm. The thermal properties of the material were included to account for thermal softening of the material, due to high temperatures in the impact zone. The MJC material model, cf. Section 2.2.5, was used. Friction was omitted in these simulations, but will be investigated in Section 6.1.

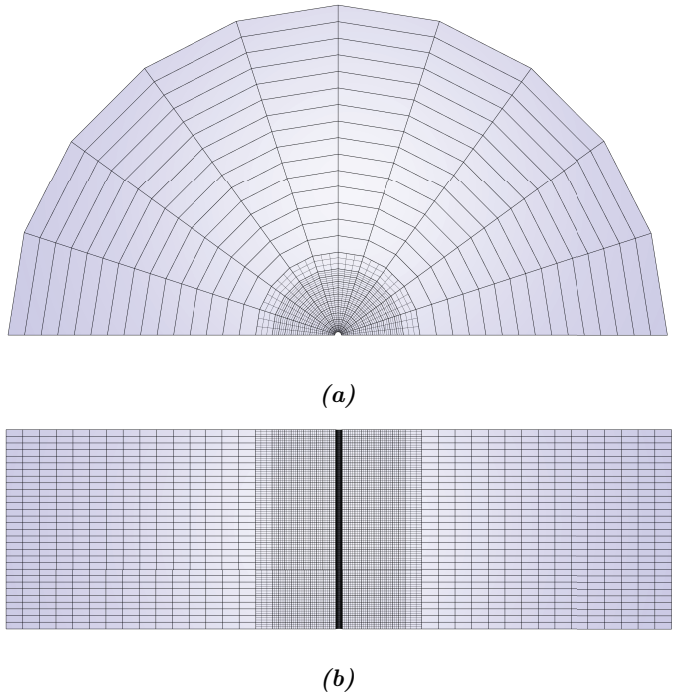

(a)

(b)

Figure 3.10: *Target mesh for a 30 mm thick plate: (a) showing target from above and (b) showing the cross-section.*

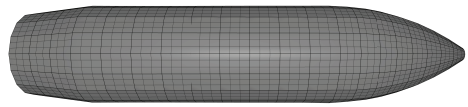

Figure 3.11: *Bullet mesh, adopted from Holmen [38].*

Regarding the use of boundary conditions, a symmetry plane was established. The periphery of the target was initially fixed, and a small study was conducted to investigate the effect of the periphery boundary condition. The results showed a negligible influence, but the boundary condition was applied in the final preliminary study model to obtain good correspondence with the actual test setup in the laboratory. The reader is referred to Holmen and Johnsen [33] for a more thorough study on the topic.

The Recht-Ipson model, presented in Section 2.1.3, was used to estimate the ballistic limit curves from the numerical results. Figure 3.13 presents the ballistic limit curves for the two considered plate thicknesses. As seen in the figure, the 25 mm and 30 mm plates have predicted ballistic limits of 383 $^{m}/_{s}$ and 428 $^{m}/_{s}$, respectively. Based on the range of the modified Mauser rifle used in the experiments, cf. Section 3.4, the 30 mm was considered the best choice.

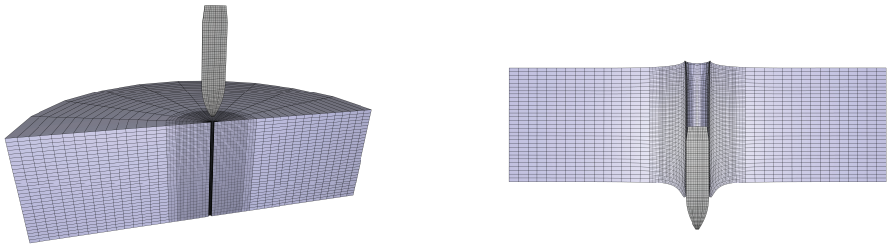

(a) *(b)*

Figure 3.12: *3D solid element model of both bullet and target with mesh for a 30 mm thick plate: (a) before impact and (b) during impact.* $v_i = 700$ m/s *and* $v_r = 551.1$ m/s.

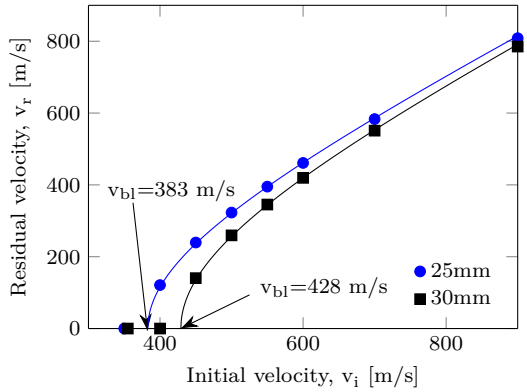

Figure 3.13: *Predicted ballistic limit curves for plate thicknesses 25 mm and 30 mm, respectively. The solid lines represent the Recht-Ipson model fitted to the data points shown.*

3.4 Experimental Setup

The ballistic impact tests were conducted in a compressed gas-gun facility at the Departement of Structural Engineering at NTNU. A 7.62 x 63 mm smooth-bored Mauser rifle with a barrel length of 1 m, located inside an impact chamber of 16 m^3, was used to fire the APM2 bullets. The setup is illustrated in Figure 3.14. The rifle was mounted in a rigid rack to ensure precise impact points, and was fired from a safe distance using a magnetic trigger. The velocity area for the Mauser rifle is in the range of $300 \text{m/s} < v_i < 1150 \text{m/s}$, when using only the hardened steel core of the bullet.

A Phantom V1610 high-speed camera with a frame rate of 70000 fps was used to capture the penetration process. The camera was triggered when the bullet penetrated a metal sheet placed in front of the muzzle of the barrel. Figure 3.15 shows several of the men-

tioned parts of the experimental setup. A more detailed description of the ballistic test rig is presented in Børvik et al. [45, 46].

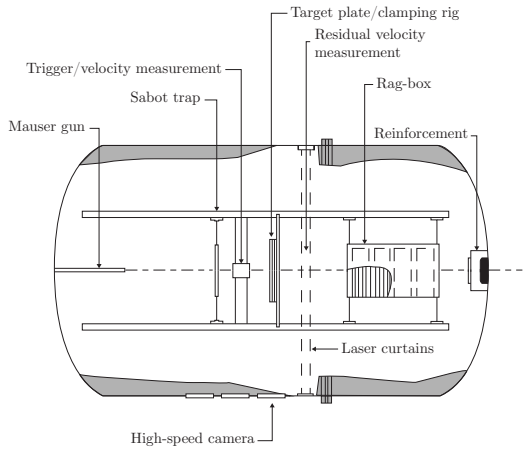

Figure 3.14: *Schematic of the experimental setup, adapted from Børvik et al. [45].*

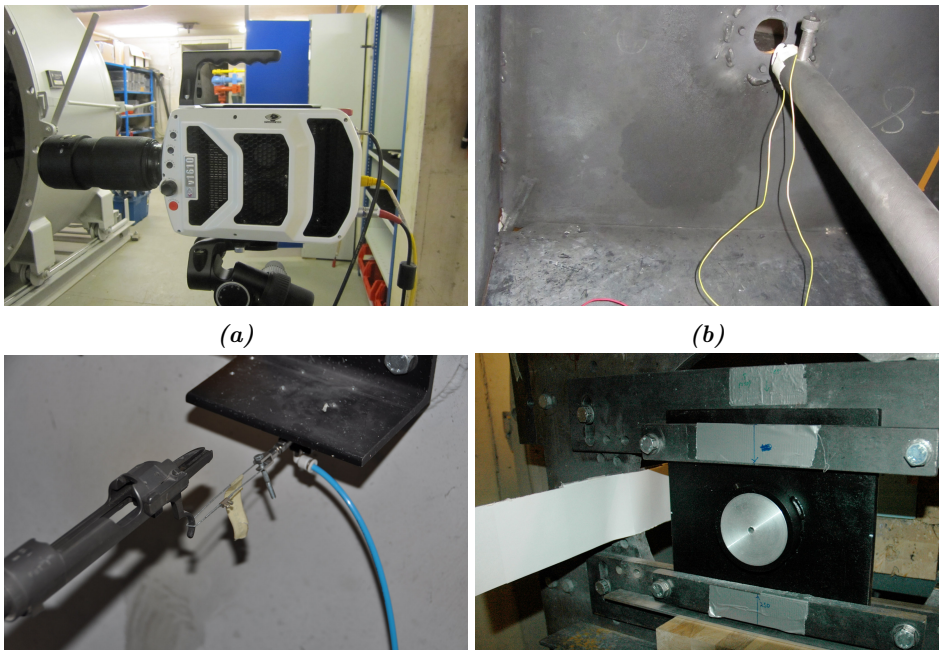

Figure 3.15: *(a)The high-speed camera, (b) the trigger device for the high-speed camera, (c) the remote, magnetic trigger for the rifle, and (d) target plate and steel frame attached to the clamping rig. (a)-(c) are adopted from Holmen and Johnsen, and Orthe and Thorsen [33, 47].*

The target plate was fixed in a rigid steel frame that was specially designed and produced at NTNU for these tests, shown in Figure 3.16(a). The frame was attached to a clamping rig by four screws, which ensured fixed horizontal boundaries, as shown in Figure 3.15(d). The target plates tended to expand during the tests due to large plastic deformations. This made it difficult to loosen and adjust the plates to the desired points of impact. All plates were therefore turn-milled to be more operable.

To fire the hardened steel core of the APM2 bullets, a specially designed plastic sabot of 0.39 ± 0.005 g, shown in Figure 3.16(b), was used to fasten the core in the cartridge. A press was needed to properly unite the parts.

(a) *(b)*

Figure 3.16: *(a) AlMgSi target plate and steel frame, and (b) plastic sabot, hardened steel core in sabot and cartridge.*

The impact velocities of the bullets were tuned by adjusting the amount of powder in the cartridge. Different initial velocities were desirable for identifying the ballstic limit curve of the target material. The diameter of the sabot was almost identical to the bullet casing diameter, and inconsistencies could form when uniting the parts. In addition, the bottom of the sabot was quite thin, which resulted in some failed sabots during assembly.

Figure 3.17 shows the impact locations on the target plates. The locations were chosen such that the total amount of 20 shots were spread among the four target plates, without getting any interaction or influence from the other locations. The tests were conducted as presented in Table 3.5.

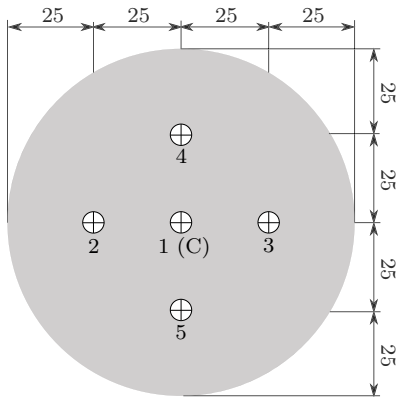

Figure 3.17: *Schematic of the target impact locations. Dimensions in mm.*

3.5 Experimental Results

This section presents the results obtained from the ballistic experiments. A total amount of 18 out of 19 shots were successful, and the results from these are presented in Table 3.5. The fifth test gave no measurements due to an error in the camera triggering device. Pictures of the target plates after testing, as well as close up photos of all entry and exit holes, are presented in Appendices A and B, respectively.

Table 3.5: *Tabulated results from ballistic experiments. Impact locations are illustrated in Figure 3.17.*

Plate	Impact location	Test no.	Gunpowder [grain]	v_i [$^m/_s$]	v_r [$^m/_s$]	Comment
1	1 (Center)	1	40.0	790.5	591.6	OK
	2	2	30.0	562.9	243.5	OK
	3	3	28.0	572.9	248.2	OK
	4	8	27.0	477.0	0.0	No exit
	5	9	45.0	788.0	609.5	Projectile split in three
2	1 (Center)	4	26.0	512.6	0.0	No exit
	2	5	27.0	-	-	No measurements
	3	6	32.0	647.4	399.5	OK
	4	10	45.0	810.7	640.3	OK
	5	11	50.0	1028.7	891.8	OK
3	1 (Center)	7	34.0	637.0	372.8	OK
	2	12	37.0	764.4	573.7	OK
	3	13	35.0	605.9	345.4	OK
	4	14	36.0	639.8	392.0	OK
	5	15	29.0	531.6	128.3	OK
4	1 (Center)	16	36.5	701.3	477.4	OK
	2	17	36.5	718.7	513.7	OK
	3	18	36.5	721.9	513.7	OK
	4	19	36.5	731.7	525.8	OK

The ballistic limit curve, presented in Figure 3.18, was obtained by using a least-squares method and the Recht-Ipson model presented in Section 2.1.3. The Recht-Ipson parameters were determined to:

$$a = 0.9851$$
$$p = 2.1072$$
$$v_{bl} = 517.5 \text{ m/s}$$

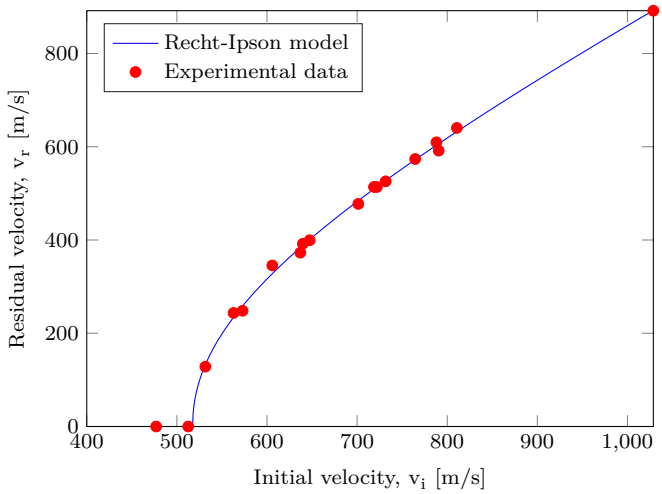

Figure 3.18: *Ballistic limit curve for the AlMgSi plates.*

The a-parameter is very close to unity, which indicates that the plates mainly failed by ductile hole growth without any plugging. This is in good correspondance with the observed failure mode for the relatively ductile AlMgSi target material. A p-parameter of $p \approx 2$ shows that no plug or fragments were knocked out of the plates. The ballistic limit at 517.5 m/s is much higher than what was expected based on the preliminary study, cf. Section 3.3, which resulted in a ballistic limit velocity of 428.0 m/s. Possible reasons for this discrepancy of approximately 90 m/s are friction and strain rate dependency at high temperatures, which are further discussed in Section 6.1.

Figures 3.19, 3.20 and 3.21 show the penetration process for three different shots with different residual velocities. Test number 15, shown in Figure 3.19, had an initial velocity close to the ballistic limit, while tests number 1 and 11 had velocities well above the ballistic limit velocity.

A general tendency was that all shots went relatively straight, with a negligible pitch angle. If the pitch angle had been larger than 3% - 5%, it could have reduced the penetration capacity of the bullet [48]. Note that some fragmentation occur on the back side of the plates for all tests, though more is seen for higher initial velocities. It is although hard to determine if these fragments originate from the target plates or the

plastic sabot. According to Børvik [44], this fragmentation is negligible compared to similar tests conducted on other materials.

Figures 3.19(b)-(c), 3.20(b)-(c) and 3.21(b)-(c) show the entry and exit holes in the target plates. When investigating the entry holes, it can be seen that more severe deformation occur during impact for tests with high initial velocity. For instance, it is seen that test number 11 exhibits much more deformation than test number 15.

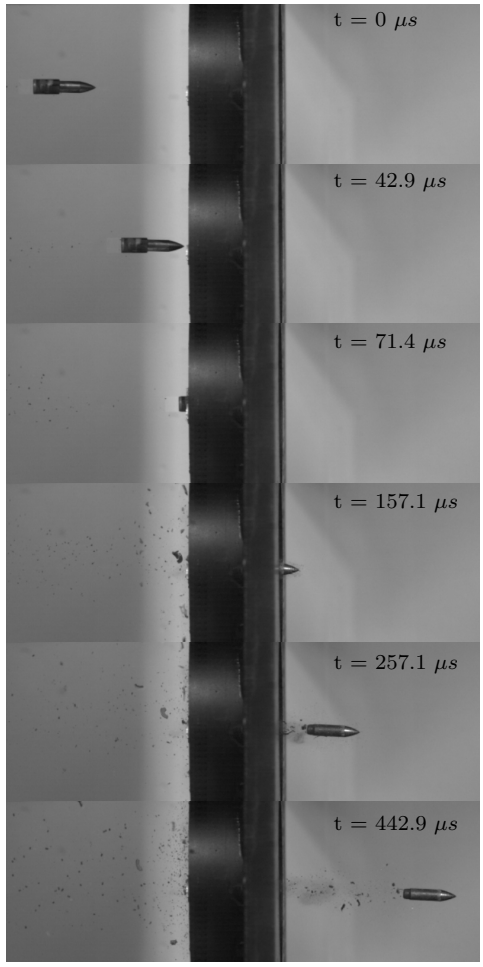

(a) *Time-lapse.*

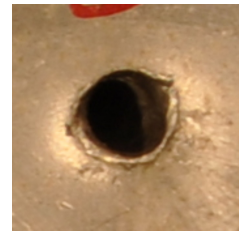

(b) *Entry hole.*

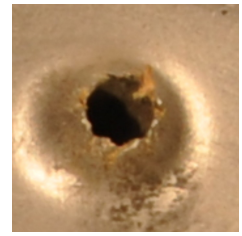

(c) *Exit hole.*

Figure 3.19: *Time-lapse, entry and exit hole for test number 15, presented in Table 3.5.* $v_i = 531.6^{m}/_{s}$, $v_r = 128.3^{m}/_{s}$.

The tendency for the exit holes is that high residual velocities yield local deformation with more rifts along the edge. When comparing the exit holes for tests number 15 and 11, shown in Figures 3.19(c) and 3.21(c), it is seen that more deformation occur around

the exit hole for test number 15 than for test number 11. This indicates that low residual velocities yield deformation in a larger area around the hole than higher residual velocities, which exhibit more local deformation. Test number 1, shown in Figure 3.20(c) has an exit hole that is somewhat in between the two others. Considering the residual velocity of test 1, this deformation seems reasonable. Generally, it can be established that all three tests yield ductile hole growth, and that this is the dominating failure mechanism for the AlMgSi-alloy.

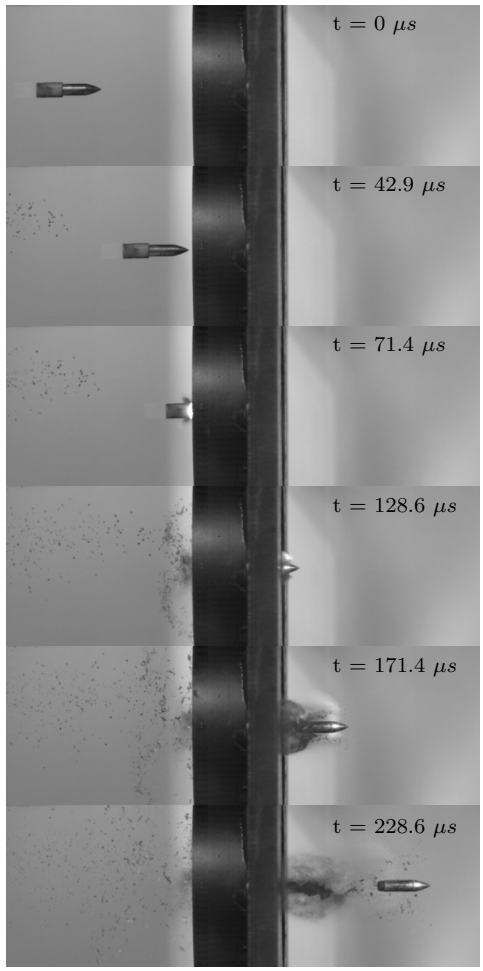

(a) *Time-lapse.*

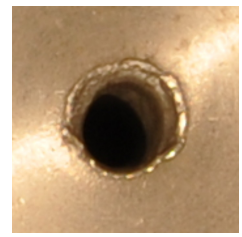

(b) *Entry hole.*

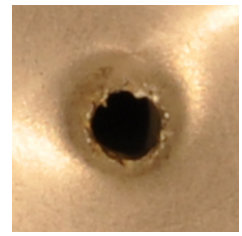

(c) *Exit hole.*

Figure 3.20: *Time-lapse, entry and exit hole for test number 1, presented in Table 3.5.* $v_i = 790.5^{m}/_{s}$, $v_r = 591.6^{m}/_{s}$.

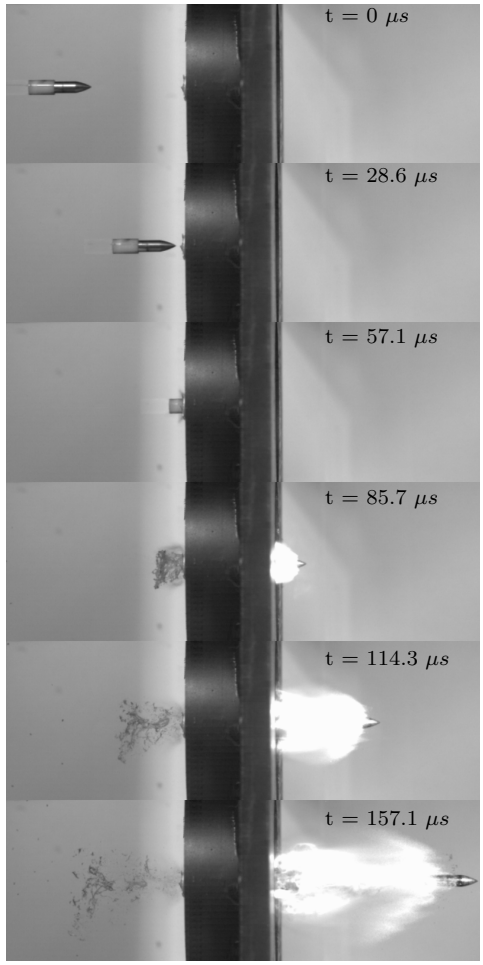

(a) *Time-lapse.*

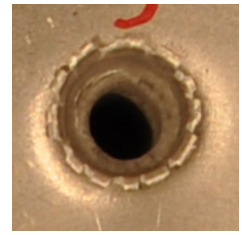

(b) *Entry hole.*

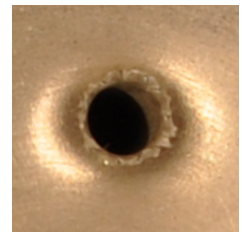

(c) *Exit hole.*

Figure 3.21: *Time-lapse, entry and exit hole for test number 11, presented in Table 3.5.* $v_i = 1028.7^{\text{m}}/_{\text{s}}$, $v_r = 891.8^{\text{m}}/_{\text{s}}$.

3.6 Investigation of Macro- and Microstructure

To investigate the surface and grain structure of the bullet holes, plate number 2 was cut in half to reveal the cross section of the hole perpendicular to the trajectory. Half of the plate is shown in Figure 3.22. Both macroscopy and light optical microscopy were used to examine the surface for the left- and rightmost bullet holes shown in the picture.

For the macroscopy, one half of the bulk material was investigated in a Leitz Wild Photomacroscope M400. No further sample preparation was required for the macroscopy

technique [49].

In order to use light optical microscopy for examining the grain structure around the holes, samples were cut from the bulk material and mounted in epoxy. The preparation of the samples consisted of mechanical grinding to ASTM mesh 4000 and polishing with 3 μm and 1 μm diamond paste. The samples were further chemically polished for 4 minutes using a 10% OP-U dissolution, followed by 1 minute of polishing using plenty of water. Finally, the samples were anodized in a 5% HBF4 aqueous at 20V for 120 seconds to reveal the microstructure under polarized light. To investigate the microstructure, a Leica MEF4M light optical microscope equipped with a sub-parallel λ-plate was used [49].

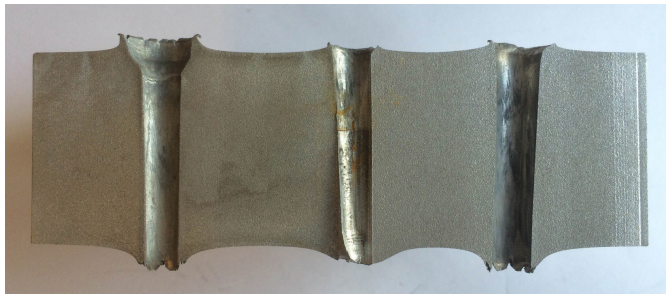

Figure 3.22: *Cross section of plate 2 after experimental tests. Test data is presented in Table 3.5. The leftmost hole, the center hole and the rightmost hole correspond to tests number 11, 4 and 10, respectively.*

Figure 3.23 shows the two epoxy test samples made for studying the microscopic structure of the material. Both samples are taken from plate number 2, where test sample 1 corresponds to test number 10 and test sample 2 corresponds to test number 11 presented in Table 3.5.

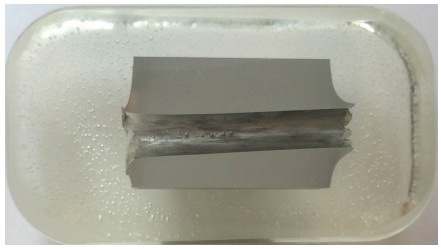

(a) *Test sample 1.* $v_i = 810.7^{\text{m}}/_{\text{s}}$, $v_r = 640.3^{\text{m}}/_{\text{s}}$.

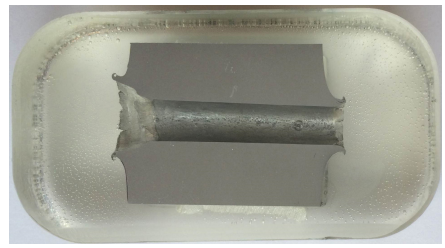

(b) *Test sample 2.* $v_i = 1028.7^{\text{m}}/_{\text{s}}$, $v_r = 891.8^{\text{m}}/_{\text{s}}$.

Figure 3.23: *Epoxy test samples for microscopic study.*

Figures 3.24 and 3.25 present photos of the bullet holes obtained from the macroscopy. Each figure displays an overview of the bullet hole as well as three photos taken at 20x magnificiation. These magnified photos, taken from the entry, middle and exit parts of

the hole, show the macrostructure in more detail. As seen in Figure 3.24, there are severe deformations near both entry and exit. The surface of the hole is relatively smooth, which indicates ductile hole growth. This is as expected for the ductile AlMgSi material and this plate thickness, and was confirmed by the experiments. In addition, it can be seen that the hole shows signs of petalling near the exit side. Note that this is not the dominant fracture mode for the whole trajectory, but the large deformations at the exit will result in a local petalling deformation mode where some rifts appear.

Test sample 2, presented in Figure 3.25, has a similar surface to test sample 1. Since both tests were conducted at high initial velocities this was as expected. The dominant failure mechanism is ductile hole growth, but this test shows more severe deformations near the front side of the plate. As seen in the leftmost of the magnified pictures, a band has formed across the surface in the trajectory. This may be due to the high kinetic energy of the bullet, which is believed to be supported in Figure 3.21(a), where a flash of light is seen as the bullet exits the target. In addition, it can be observed that the trajectory path gets narrower farther away from the entry. This tendency can also be seen for sample 1, although not as clearly. This is most likely caused by askew cutting during preparation.

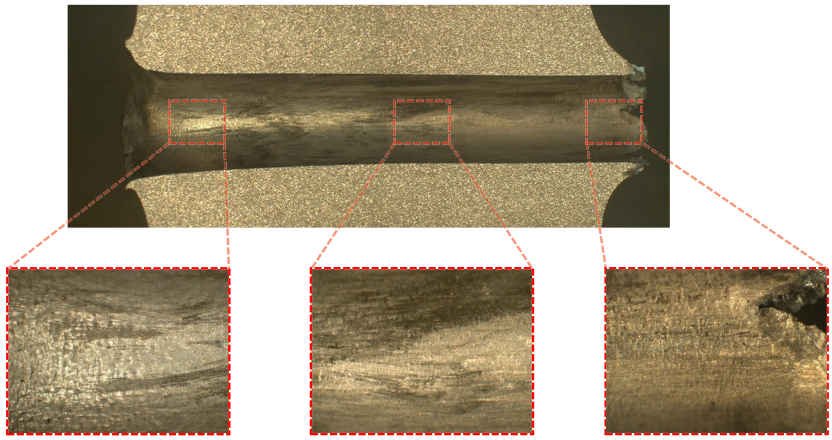

Figure 3.24: *Macrostructure of test sample 1. Photos at bottom are taken at 20x magnification.*

The optical micrograph of the grain structure in the bulk material is shown in Figure 3.26. It can be seen that the alloy has relatively large grains, with an approximate size of 65 μm. In addition, the area fraction of constituent particles is rather low [41].

Figures 3.27 and 3.28 show the microsctructure of the bulk material close to the trajectory path for samples 1 and 2, respectively. The upper rows show the microstructure at 2.5x magnification, while the lower rows show the microstructure at 10x magnification. The lower edge in the pictures correspond to the edge of the bullet hole. It can be seen that both samples get severe deformations in the grain structure close to the edge, and the deformation is clearest in the area up to 1.5 mm from the edge. The grains have been considerably deformed, compared to the grain structure shown in Figure 3.26. At the entry and exit of the hole it is seen that the material has large deformations, that have resulted in the distinct shapes seen in the figures.

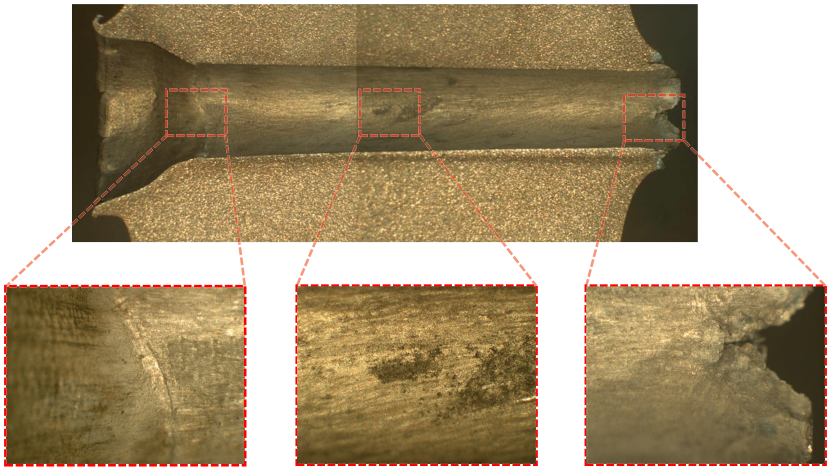

Figure 3.25: *Macrostructure of test sample 2. Photos at bottom are taken at 20x magnification.*

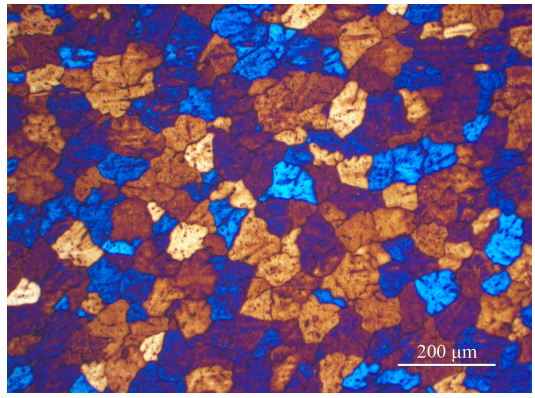

Figure 3.26: *Microstructure of the bulk material.*

Although it was expected that some of the material would have melted due to plastic dissipation, signs of this was not found in the microscopy. If the material had melted, recrystallization would have occurred in the melted region, which would have been clearly visible in the images. The recrystallized structure would look similar to the grain structure shown in Figure 3.26. There is a possibility though, that some material may have melted very locally in the trajectory region, but since the recrystallization process only occurs if the temperature is above the melting temperature of the material for approximately 0.5 seconds, this is not visible in the microscopy [49]. Since the penetration process only takes roughly 90 μs, this could mean that the recrystallization does not have time to occur. In addition, the impact zone is quite small compared to the target, which means that the target will cool down the impact area rather quickly due to high heat transfer capacity. If the material had melted this could possibly be seen in a SEM microscope. Based on the images in Figures 3.27 and 3.28 one cannot confirm that the material melted.

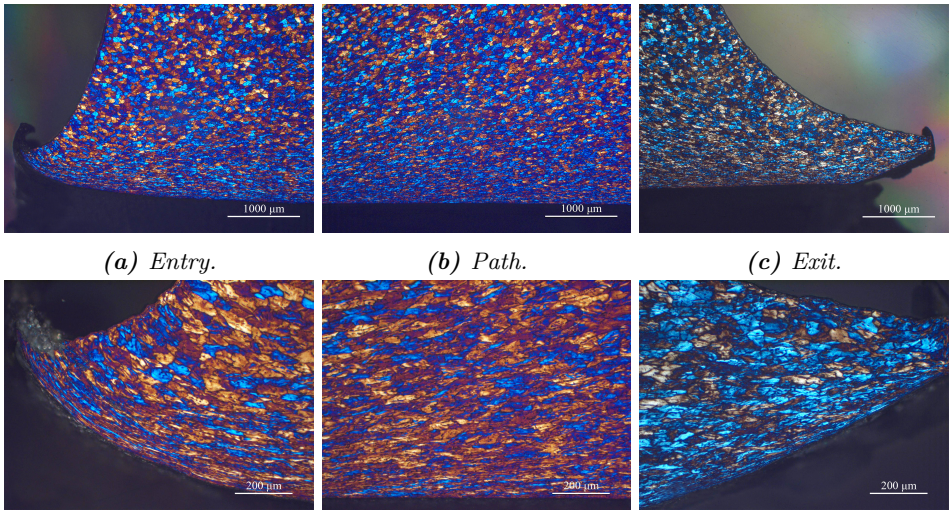

(a) Entry. *(b) Path.* *(c) Exit.*

(d) Entry. *(e) Path.* *(f) Exit.*

Figure 3.27: *Microstructure at three different locations in the trajectory path for two different magnifications for test sample 1. The upper row has a 2.5x magnification, while the lower row correspond to a 10x magnification. The leftmost pictures show the entry, the middlemost the path and the rightmost the exit of the bullet hole.*

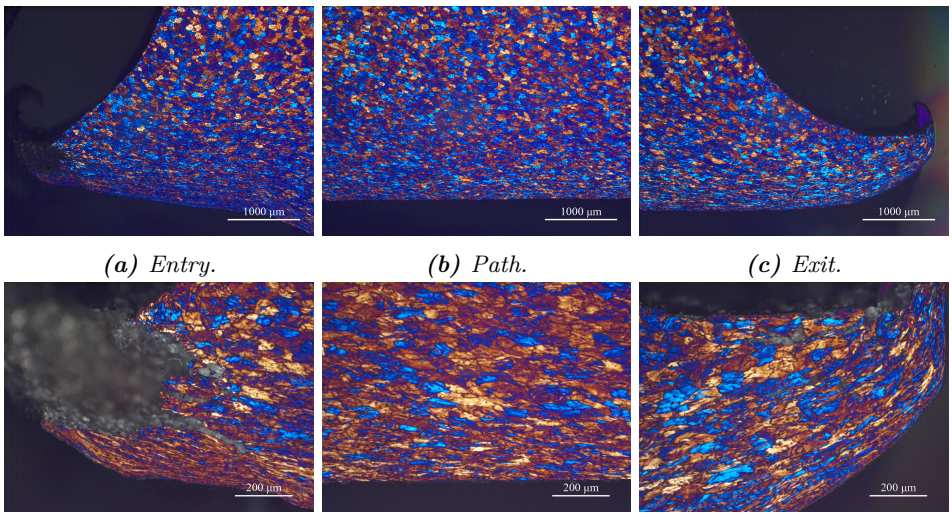

(a) Entry. *(b) Path.* *(c) Exit.*

(d) Entry. *(e) Path.* *(f) Exit.*

Figure 3.28: *Microstructure at three different locations in the trajectory path for two different magnifications for test sample 2. The upper row has a 2.5x magnification, while the lower row correspond to a 10x magnification. The leftmost pictures show the entry, the middlemost the path and the rightmost the exit of the bullet hole.*

4 Micromechanical Modelling

This chapter presents the computational cell study, conducted to investigate coalescence of voids on a microscale level. First, a section is dedicated to the numerical unit cell models studied in this thesis; the axisymmetric cell, the plane strain tension cell and the plane strain shear cell models. Further, two sections present the results from analyses using these models. Lastly, a discussion of the three two-dimensional models, as well as a comparison with three-dimensional cell data, is presented.

4.1 Numerical Micromechanical Cell Models

Numerical micromechanical unit cell models were made in Abaqus to study the growth and coalescence of voids on a microscale level. It was desirable to apply different triaxialities to be able to calibrate a fracture model that can be used for large scale simulations. All analyses were run for triaxiality ratios, σ^*, in the range between 0.65 and 2.00. According to Hopperstad [50], low triaxialities are expected for the experimental tests. Due to an asymptote in $\sigma^* = 1/3$ it was not possible to get good numerical results for triaxialities close to this value. In addition, the Gurson model overestimates the rate of void growth for triaxialities of $\sigma^* = 1/3$ and lower [13]. Therefore, $\sigma^* = 0.65$ was chosen as the lowest triaxliality in this thesis. The reader should note that further in this chapter the plane strain tension model and the plane strain shear model is referred to as the plane strain model and shear model, respectively.

One half and one quarter of the cells were modelled to save computational time for the axisymmetric and the two plane strain models, respectively. The initial radius of the void for the axisymmetric model is $r_0 = 0.1957$, while both the plane strain and shear models have an initial void radius of $r_0 = 0.0798$. Note that these radii correspond to spherical and cylindrical voids, respectively, and are relative to the initial cell radius and height, $R_0 = 1$ and $H_0 = 1$. All three models have the same initial void volume fraction of $f_0 = 5 \cdot 10^{-3}$, obtained from Westermann et al. [41]. The meshes used for all three models are illustrated in Figure 4.1. The entire shear cell was modelled, including a particle inside the void modelled as an elastic inclusion with ordinary steel material parameters. The main reason for this is to properly show the shear deformation mode. Note that the particle is not included in the mesh presented in Figure 4.1(b).

The axisymmetric model was made as a deformable axisymmetric part, while the plane strain and shear cells were made as 2D deformable parts. In all three models, the upper edge of the cell was constrained, to ensure periodic boundary conditions. The reader is referred to Section 2.3 for further information regarding the array of microscopic cells. For the shear cell, additional constraints were applied along the vertical edges in both

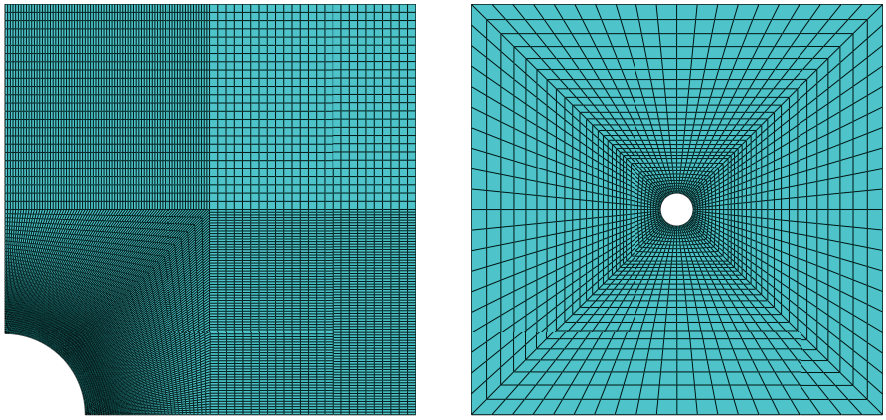

(a) *Axisymmetric and plane strain tension unit cells.*

(b) *Plane strain shear unit cell, excluding the particle.*

Figure 4.1: *Mesh for the unit cell models.*

the horizontal and vertical directions, to ensure that the egdes remained straight during deformation until coalescence. Figure 4.2 illustrates the shear unit cell with nodes along the vertical edges. The following constraint equations were applied for each node pair:

$$u_1^{right} - u_1^{left} - u_1^A + u_1^B = 0 \tag{4.1}$$

$$u_3^{right} - u_3^{left} = 0 \tag{4.2}$$

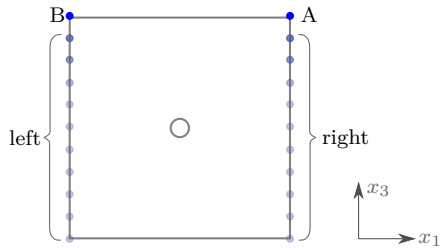

Figure 4.2: *Illustration of node pair constraints for the shear unit cell.*

Figure 4.3 shows the boundary and loading conditions for the different cells. The axisymmetric cell, seen in Figure 4.3(a), have symmetry boundary conditions along the left and bottom edges. Note that the axisymmetric cell, which represents both generalized tension and generalized compression, was established using a Python script made by Dæhli [51]. User subroutines in Fortran were used to describe the material behaviour, using a von Mises yield criterion with a Voce hardening rule, as well as the displacement of the reference node shown in the figure [51]. Note that for some analyses of the axisymmetric cell

in generalized tension and compression, the GTN model was applied in the matrix using the built-in GTN model in Abaqus. These analyses are presented in Sections 4.2.1.1 and 4.2.2.1.

The deformation of the axisymmetric cell is driven by a displacement applied in a reference node north-east of the upper right corner of the cell, as shown in Figure 4.3(a). The upper right corner node was constrained to the reference node by the multi-point constraint subroutine.

The boundary conditions of the plane strain cell is identical to the axisymmetric cell. Unlike the axisymmetric model, loading was applied by surface tractions on the upper and right edges using the static Riks algorithm, as illustrated in Figure 4.3(b). The ratio between the tractions in the x_1- and x_3-directions was calculated such that the triaxiality was held at a constant value during deformation.

For the shear unit cell, periodic boundary conditions were applied on the vertical edges. In addition, the bottom edge was fixed. A displacement was applied on the upper edge, as shown in Figure 4.3(c), to get a shear deformation mode.

One major difference between the shear cell model and the two other models is the use of a particle inside the void. This was done to ensure void growth and coalescence. The shear cell model yield a triaxiality approximately equal to zero [50]. For low triaxialities the void will simply close as a result of shear deformation unless a particle is included in the void. This is shown in Figure 4.4.

Figure 4.5 shows the mesh of the shear unit cell closest to the void, including the particle. A surface-to-surface contact formulation with Coloumb friction of $\mu = 0.1$ was used between the cell matrix and the particle, and a surface-to-surface algorithm with self contact was used for the matrix.

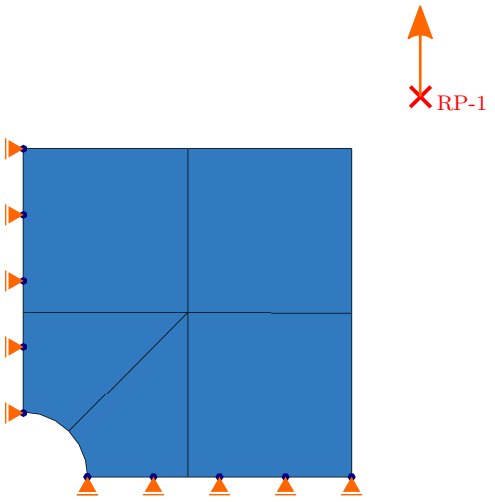

(a) Axisymmetric unit cell. RP-1 annotates the reference node.

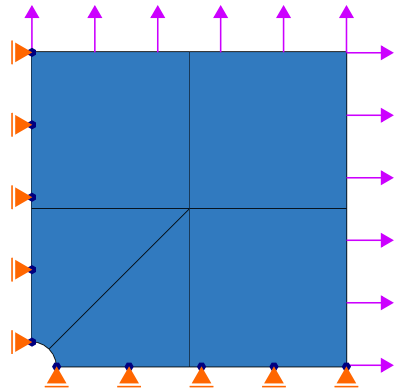

(b) Plane strain tension unit cell.

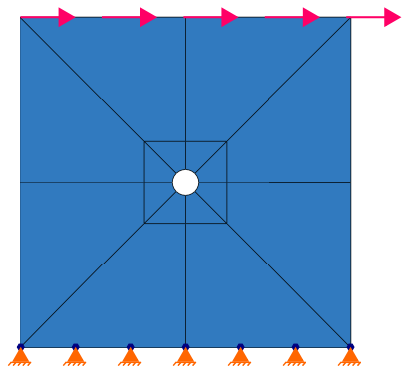

(c) Plane strain shear unit cell.

Figure 4.3: *Boundary and loading conditions for the three unit cells.*

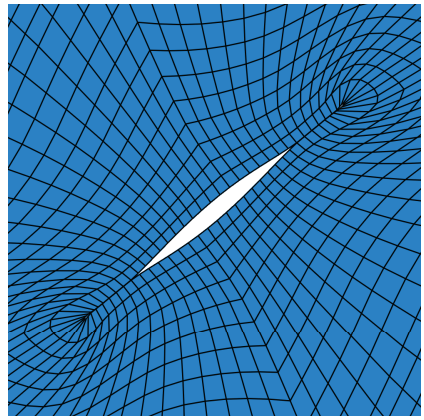

Figure 4.4: *Section showing the deformed void of the shear unit cell without a particle.*

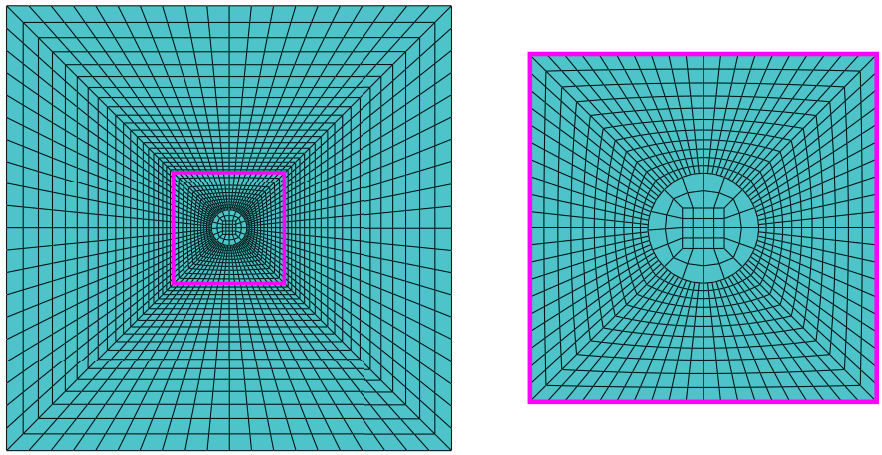

Figure 4.5: *Mesh closest to the void of the shear unit cell, including the particle.*

4.2 Axisymmetric Cell

This section presents the results from the axisymmetric unit cell analyses. The reader is referred to Section 2.3.2.1 for some fundamental theory on the simplified axisymmetric unit cell. Analyses were performed for two different loading cases; generalized tension and generalized compression, which correspond to Lode parameters $\mu_\sigma = -1$ and $\mu_\sigma = 1$, respectively. Some results from the two loading cases with the GTN model used in the matrix are presented in Sections 4.2.1.1 and 4.2.2.1.

4.2.1 Generalized Tension

For generalized tension, the cell is deformed by applying a displacement in the reference node, as illustrated in Figure 4.3(a). The deformation process for $\sigma^* = 2$ is shown in Figure 4.6. As seen in the pictures, the aspect ratio of the cell changes during deformation. When coalescence occurs, the vertical edges remain fixed in the horizontal direction while the cell continues to deform in the vertical direction and the void takes on an oblate shape. Hence, coalescence is defined once a uniaxial deformation mode occurs, cf. Figure 4.7. Picture number three from the left, in Figure 4.6, is taken right after coalescence.

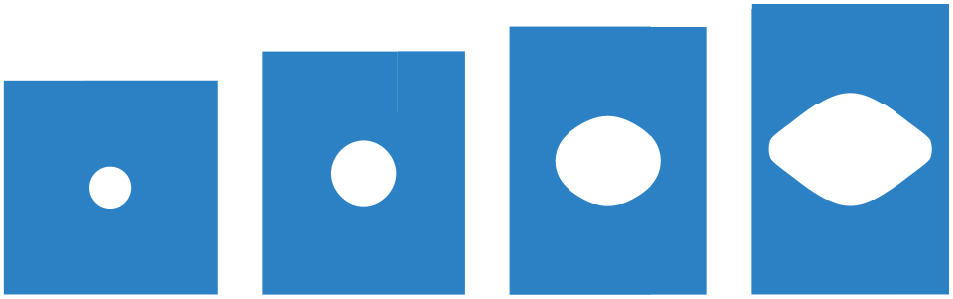

Figure 4.6: *Deformation of the axisymmetric unit cell in generalized tension for triaxiality ratio* $\sigma^* = 2$.

Figure 4.7 shows the magnitude of the macroscopic strain in the x_1-direction, $\|E_{11}\|$, versus the macroscopic equivalent strain, E_{eq}, for different triaxiality ratios. As seen in the figure, all curves have an ascending gradient before they flatten out at a given value of $\|E_{11}\|$. The crosses mark the points of coalescence, i.e., when we get a uniaxial deformation mode. Figure 4.8 shows the point of coalescence in a void volume fraction versus equivalent strain plot. For all triaxiality levels, an exponential growth in void volume fraction is observed. The void volume fraction curve has a distinct bend near the point of coalescence for low triaxialities.

The relationship between the macroscopic stress and the macroscopic equivalent strain is plotted in Figure 4.9. It is seen that coalescence occurs after the point of maximum equivalent stress. The stress-strain response is determined by material strain hardening

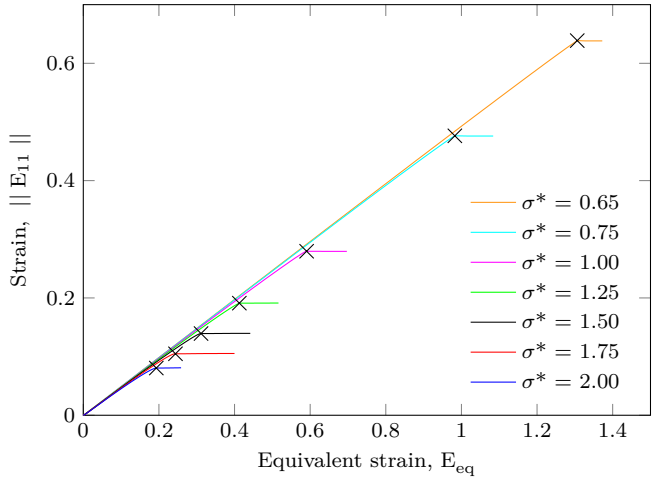

Figure 4.7: *Strain in the x_1-direction vs. equivalent strain for generalized tension. The crosses represent the points of coalescence.*

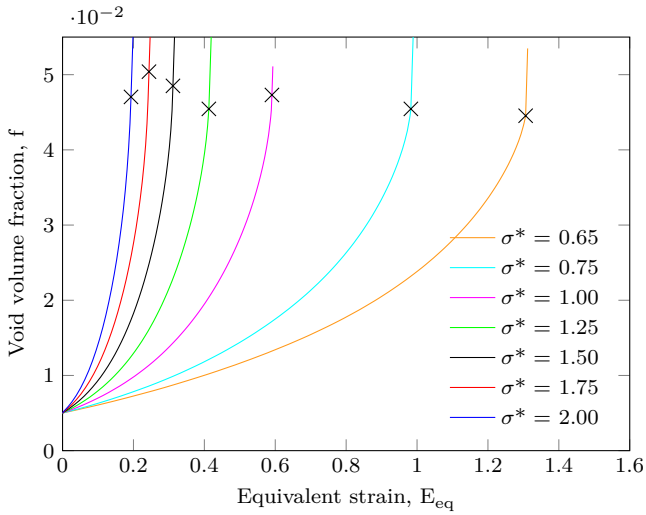

Figure 4.8: *Void volume fraction vs. equivalent strain for generalized tension. The crosses represent the points of coalescence.*

and softening induced by the void. At high triaxialities, the softening of the void is more prominent, causing lower fracture strain values.

Figure 4.10 shows the critical void volume fraction for the given triaxiality ratios. As seen in the figure, the value is relatively constant for all triaxialities. This indicates that the critical void volume fraction is relatively independent of the triaxiality ratio for $\mu_\sigma = -1$.

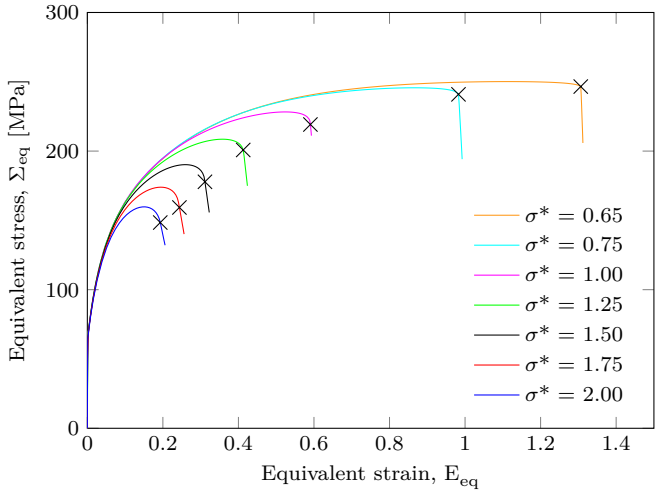

Figure 4.9: *Equivalent stress vs. equivalent strain for generalized tension. The crosses represent the points of coalescence.*

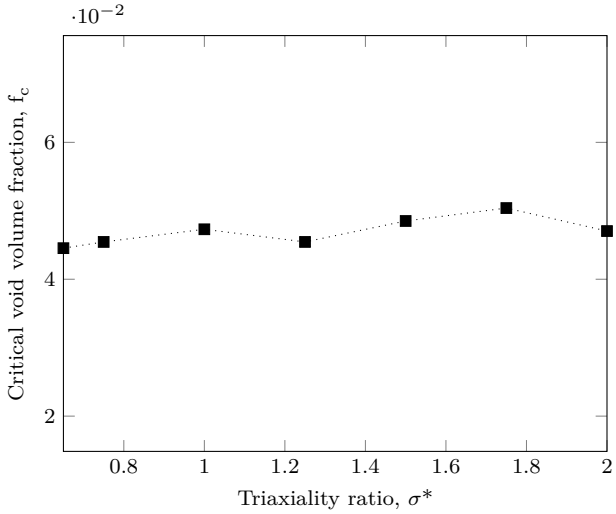

Figure 4.10: *Critical void volume fraction vs. triaxiality ratio for generalized tension.*

The critical equivalent strain is plotted for all triaxialities in Figure 4.11. It is seen that low triaxialities yield high critical strains, while higher triaxiality ratios have relatively low critical strains.

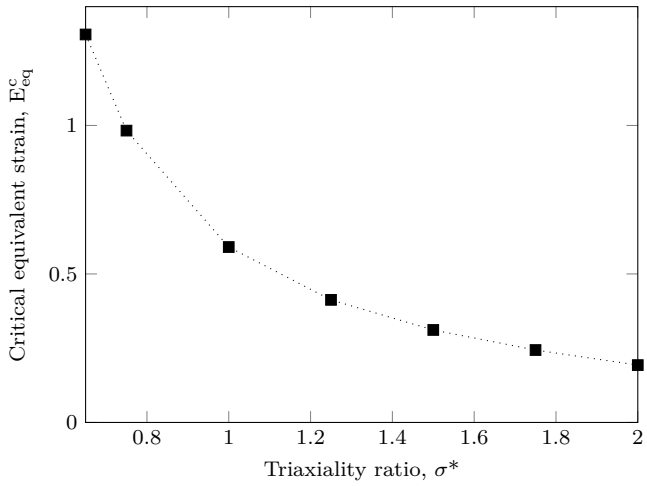

Figure 4.11: *Critical equivalent strain vs. triaxiality ratio for generalized tension.*

4.2.1.1 Gurson-Tvergaard-Needleman in the Matrix

The Gurson-Tvergaard-Needleman porous plasticity model, presented in Section 2.2.7.1, was used in the matrix for the axisymmetric unit cell in generalized tension. This was done to achieve a more realistic material behaviour, as the AlMgSi-alloy is considered a porous material. A typical volume element is therefore assumed to consist of numerous smaller voids and particles, in addition to the large primary void. The critical equivalent strain, E^c_{eq}, obtained from the analyses presented in Section 4.2.2 with a von Mises matrix material, was considered high. Implementation of GTN in the matrix was believed to decrease the critical equivalent strain. Standard Tvergaard parameters, $q_1 = 1.5$ and $q_2 = 1.0$, as well as a void volume fraction of $5 \cdot 10^{-4}$, was used in the matrix. This void volume fraction constitute $1/10$ of the large primary void with initial void volume fraction of $f_0 = 5 \cdot 10^{-3}$.

Figure 4.12 illustrates the void volume fraction in the unit cell matrix for $\sigma^* = 2$, after coalescence. As seen, the void volume fraction is large along the horizontal ligament. The highest value is observed to be approximately equal to the critical void volume fraction presented in Figure 4.10.

The critical primary void volume fraction with GTN in the matrix is presented in Figure 4.13, together with the results from the von Mises analyses in Figure 4.10. The general tendency is lower critical void volume fractions with GTN in the matrix, but the value is not constant for all triaxialities, such as for von Mises. Note that the curves only represent the void volume fraction of the large void, i.e., they do not include the void volume fraction in the matrix. Ergo, the tendency seen for the curve with GTN in the matrix is not entirely correct. The void volume fraction in the matrix may be large, such that the total void volume fraction for the different triaxiality ratios may be relatively

constant. It is difficult to account for the void volume fraction in Abaqus, hence this has not been verified.

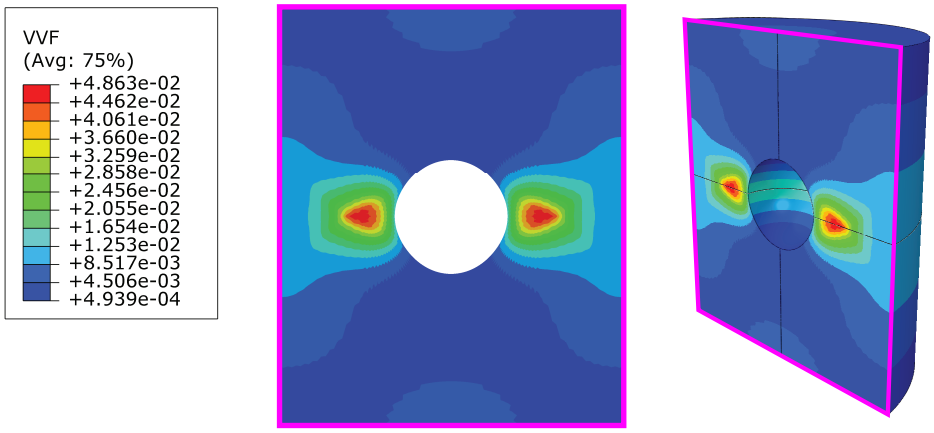

Figure 4.12: *Void volume fraction for the axisymmetric unit cell in generalized tension with GTN in the matrix for triaxiality ratio $\sigma^* = 2$.*

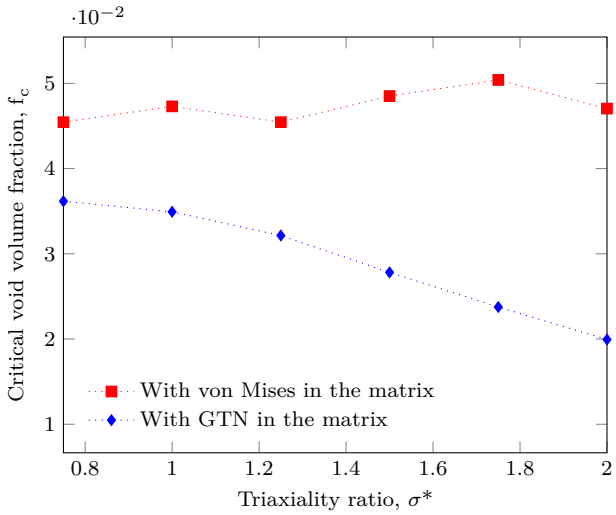

Figure 4.13: *Critical void volume fraction vs. triaxiality ratio for generalized tension with GTN in the matrix.*

Figure 4.14 shows a comparison of the critical equivalent strain for analyses with and without GTN in the matrix. By including GTN, we get lower values for the critical equivalent strain, as expected. Lower critical strain yields earlier onset of coalescence, i.e., less deformation, which is believed to be more realistic for the AlMgSi-alloy.

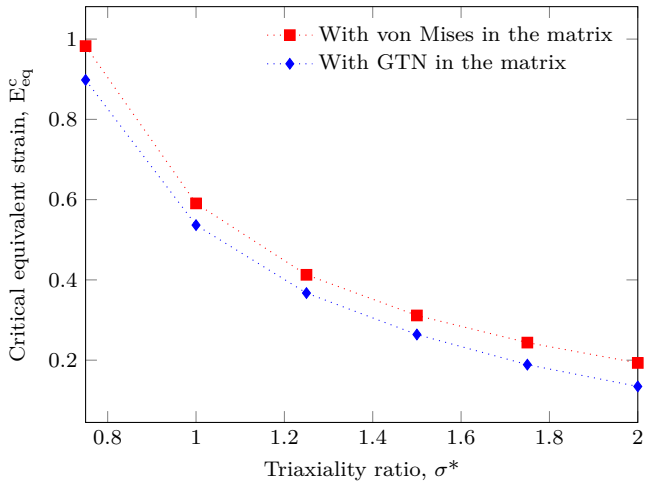

Figure 4.14: *Critical equivalent strain vs. triaxiality ratio for generalized tension with GTN in the matrix.*

4.2.2 Generalized Compression

As for generalized tension, cf. Section 4.2.1, the deformation is controlled by applying a displacement in the reference node. For generalized compression, the cell is stretched in the opposite direction of generalized tension. The stages of deformation for triaxiality ratio $\sigma^* = 2$ are shown in Figure 4.15. Compared to the deformation in generalized tension, cf. Figure 4.6, a uniaxial deformation mode is not reached. Hence, no distinct point of coalescence can be established by studying the deformation. This is further illustrated in Figure 4.16, that show the magnitude of the macroscopic strain in the x_3-direction, $\|E_{33}\|$, versus the equivalent strain, E_{eq}, for different triaxiality ratios. The curves do not flatten out as for generalized tension, which means that coalescence cannot be defined on the same basis for generalized compression.

Figure 4.15: *Deformation of the axisymmetric unit cell in generalized compression for triaxiality ratio $\sigma^* = 2$.*

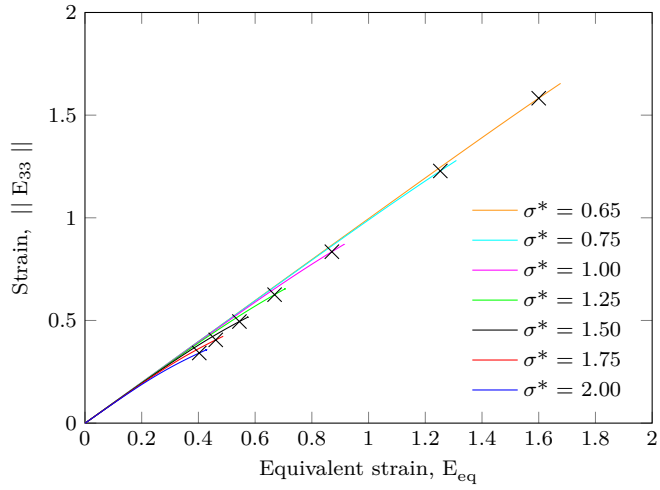

Figure 4.16: *Strain in the x_3-direction vs. equivalent strain for generalized compression. The crosses represent the points of coalescence.*

For generalized compression, a coalescence criterion was established by studying the gradient of the ligament thickness, where the ligament represents the vertical edge of the half-axisymmetric unit cell. Coalescence was defined at the point where a characteristic bend occurs. These points are illustrated with crosses in Figure 4.17. The same tendency is seen on the gradient of the ligament for generalized tension near the point of coalescence.

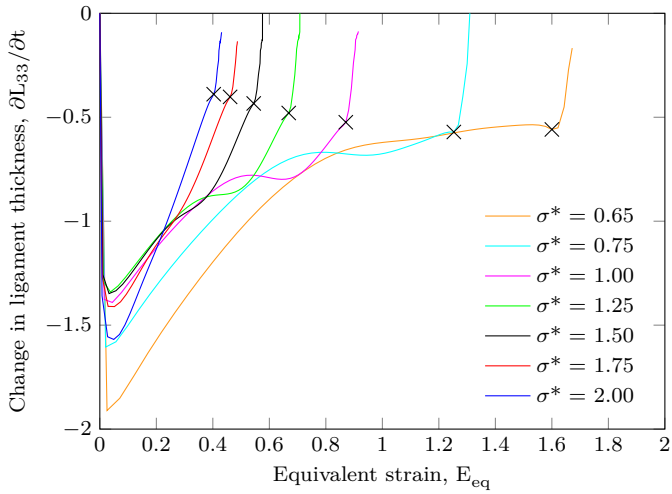

Figure 4.17: *Change in ligament thickness vs. equivalent strain for generalized compression. The crosses represent the points of coalescence.*

Figure 4.18 shows the void volume fraction versus equivalent strain. No distinct bend near the point of coalescence can be spotted in the curves for generalized compression. The equivalent stress versus equivalent strain curves in Figure 4.19 show that the point of coalescence is defined at higher strains for generalized compression than for generalized tension. The difference is especially clear for high triaxialities.

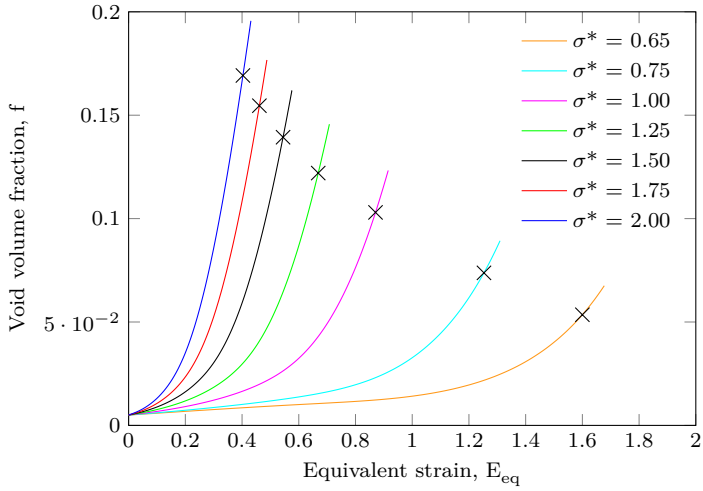

Figure 4.18: *Void volume fraction vs. equivalent strain for generalized compression. The crosses represent the points of coalescence.*

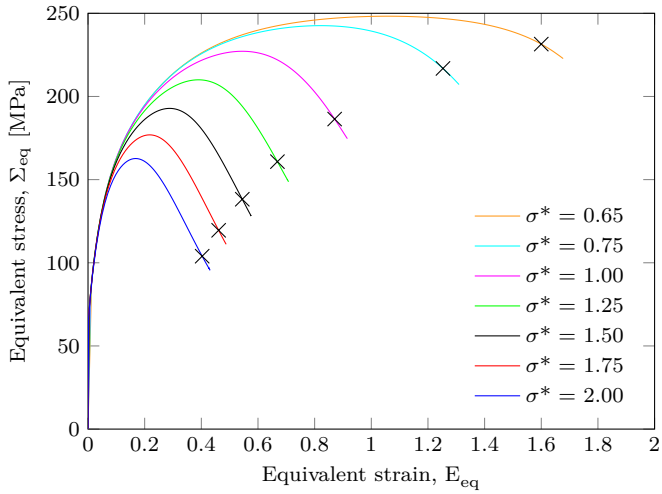

Figure 4.19: *Equivalent stress vs. equivalent strain for generalized tension. The crosses represent the points of coalescence.*

The critical void volume fractions corresponding to given triaxiality ratios are shown in Figure 4.20. It is seen that the value increases with higher triaxialities. This indicates that the critical void volume fraction is highly dependent on the triaxiality ratio for $\mu_\sigma = 1$. The critical equivalent strain is plotted for all triaxialities in Figure 4.21. As for generalized tension, low triaxialities yield high critical strains, while higher triaxiality ratios have a relatively low critical strain.

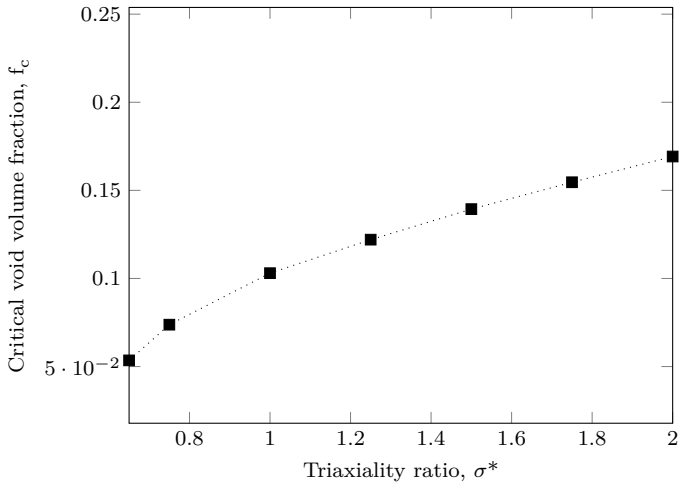

Figure 4.20: *Critical void volume fraction vs. triaxiality ratio for generalized compression.*

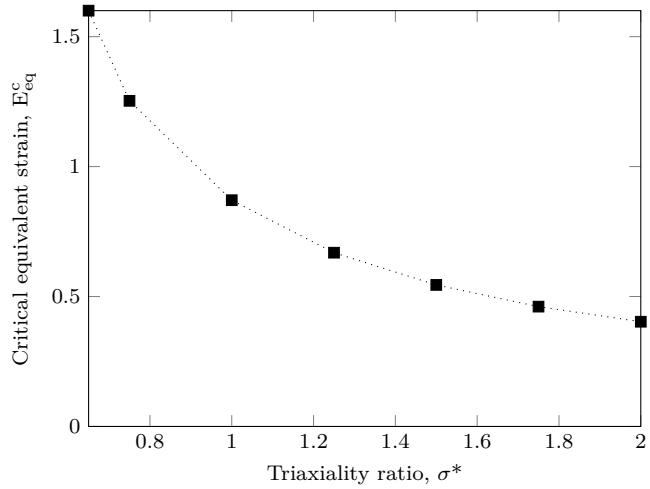

Figure 4.21: *Critical equivalent strain vs. triaxiality ratio for generalized compression.*

4.2.2.1 Gurson-Tvergaard-Needleman in the Matrix

As for generalized tension, GTN was used for generalized compression to achieve a more realistic material behaviour. Standard Tvergaard parameters and a void volume fraction of $5 \cdot 10^{-4}$ were used. Note that the GTN extension has a singularity when the void volume fraction reaches a critical value $f_C = {}^1/_{q_1}$, cf. Section 2.2.7.1. At this critical value, the yield surface collapses to a point and the analyses abort. Coalescence has therefore been defined where the local void volume fraction in the matrix reaches the critical value $f_C = {}^1/_{q_1}$. Note that this void volume fraction is unrealistically large [52].

The void volume fraction is shown in Figure 4.22 for the deformed unit cell with $\sigma^* = 2$. As seen in the figure, high void volume fractions occur in the vertical ligament, and coalescence of secondary voids in these regions is very likely. This indicates that coalescence between cells, and eventually failure, will initiate along this ligament.

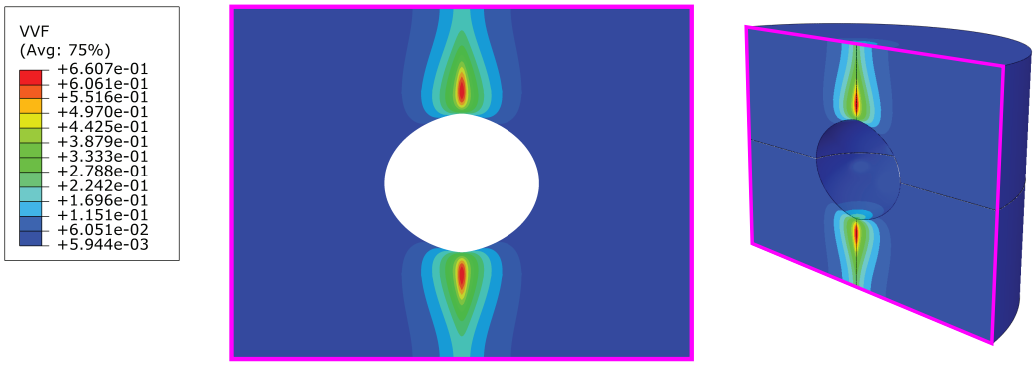

Figure 4.22: *Void volume fraction for the axisymmetric unit cell in generalized compression with GTN in the matrix for triaxiality ratio $\sigma^* = 2$.*

Figure 4.23 presents the critical void volume fraction both with and without GTN in the matrix. It is seen that the value decreases with increasing triaxiality ratio, as for generalized tension with GTN in the matrix. As described in Section 4.2.1.1 this tendency is not entirely correct, since only the void volume fraction of the primary void is accounted for. Despite this, it can be established that GTN in the matrix lowers the critical void volume fraction, also in the case of generalized compression.

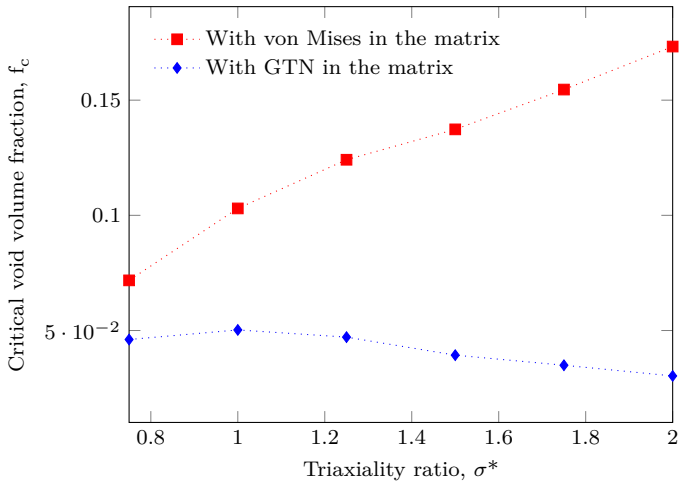

Figure 4.23: *Critical void volume fraction vs. triaxiality ratio for generalized compression with GTN in the matrix.*

As expected, the effects of increased triaxiality on the critical equivalent strain for generalized compression and generalized tension, seen in Figures 4.24 and 4.14, are similar when GTN is included in the matrix. The figures reveal, however, a larger difference between the von Mises and GTN curves for generalized compression.

This discrepancy is believed to be a result of the high void volume fraction in the matrix. This may indicate that secondary voids is of greater importance for generalized compression than for generalized tension. These secondary voids may yield coalescence at lower strains since GTN collapses when $f_c = {}^1/_{q_1}$. The analyses with GTN in the matrix cannot be run past this point and coalescence is therefore defined earlier with GTN in the matrix for generalized compression. The curves in Figure 4.24 can therefore not be compared directly. By studying Figures 4.12 and 4.22 it is seen that the void volume fraction in the matrix is approximately ten times higher for generalized compression than for generalized tension.

Figure 4.25 shows some microscopic measures for the critical element in the matrix having the largest void volume fraction. The element is located in the critical area along the vertical ligament, shown in Figure 4.25. The development of the void volume fraction in the element is presented in Figure 4.25(c). A void volume fraction of 0.66 is considered high. Figure 4.25(b) shows the local Lode parameter which is seen to be relatively constant and approximately equal to the macroscopic value of one. The triaxiality decreases in the element as the cell is deformed. This is shown in Figure 4.25(a). The rapid growth in void volume fraction is most likely due to the large local plastic strain. By studying Figure 4.25(d) it is seen that the local plastic strain increases faster than the macroscopic strain.

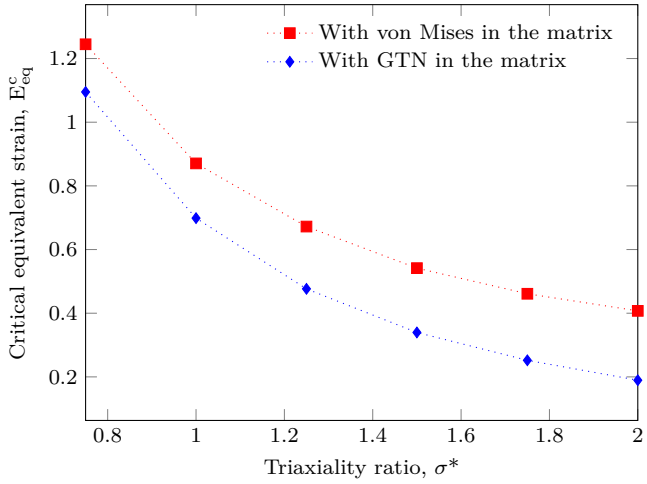

Figure 4.24: *Critical equivalent strain vs. triaxiality ratio for generalized compression with GTN in the matrix.*

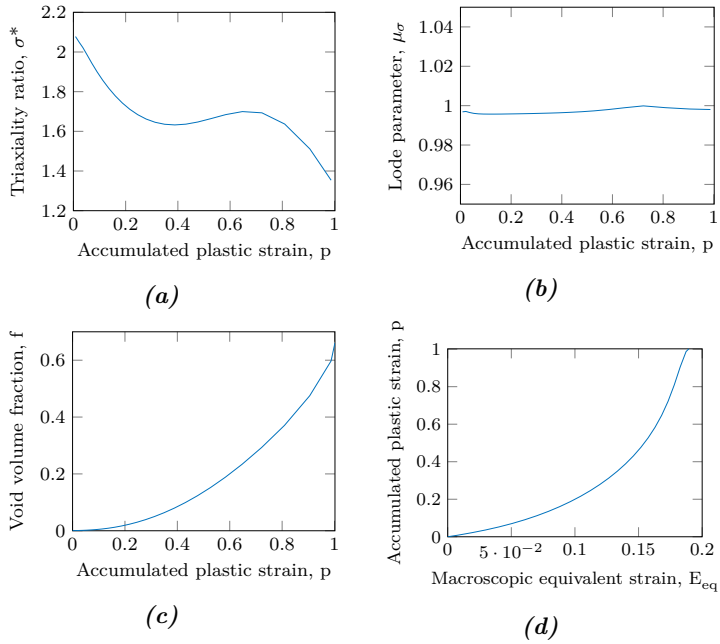

Figure 4.25: *Local measures for the critical element in the matrix for generalized compression with GTN in the matrix. The macroscopic triaxiality ratio equals* $\sigma^* = 2$.

4.3 Plane Strain Cells

This section presents the results from the two plane strain unit cells; the plane strain tension cell and the plane strain shear cell. Fundamental theory on the plane strain unit cell is presented in Section 2.3.2.2. Note that the plane strain cells correspond to a Lode parameter, μ_σ, equal to zero, and hence generalized shear.

4.3.1 Plane Strain Tension Cell

The structure of the plane strain tension cell is quite similar to the axisymmetric cell, described in Section 4.1. One important difference is the applied load, which for the plane strain cell consists of surface tractions that ensure $\mu_\sigma = 0$, and hence plane strain conditions. The surface tractions are shown in Figure 4.3(b). Equation 2.59 in Section 2.3.2.2 was used to calculate the tractions in the x_1- and x_3- directions for the given triaxiality ratios.

Figure 4.26 illustrates the deformation of the plane strain unit cell in tension for triaxiality ratio $\sigma^* = 2$. The third picture from the left is taken right after coalescence, when the cell is in a uniaxial deformation mode. As for the axisymmetric cell in generalized tension there is a disctinct point of coalescence. This is clearly seen in the curves presented in Figure 4.27. Therefore, the same coalescence criterion was used for the plane strain cell as for the axisymmetric cell in generalized tension.

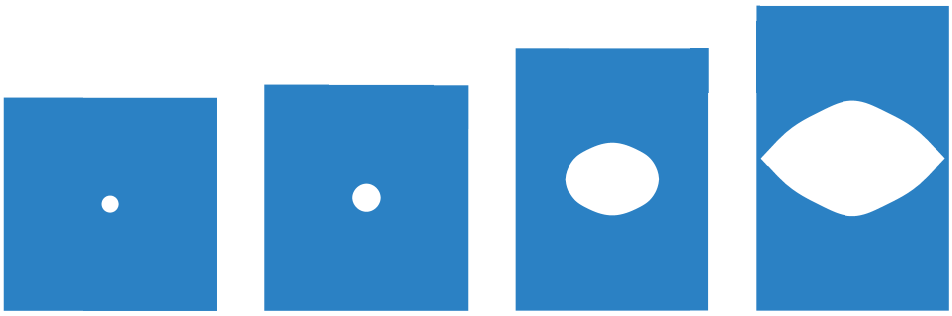

Figure 4.26: *Deformation of the plane strain unit cell in tension for triaxiality ratio* $\sigma^* = 2$.

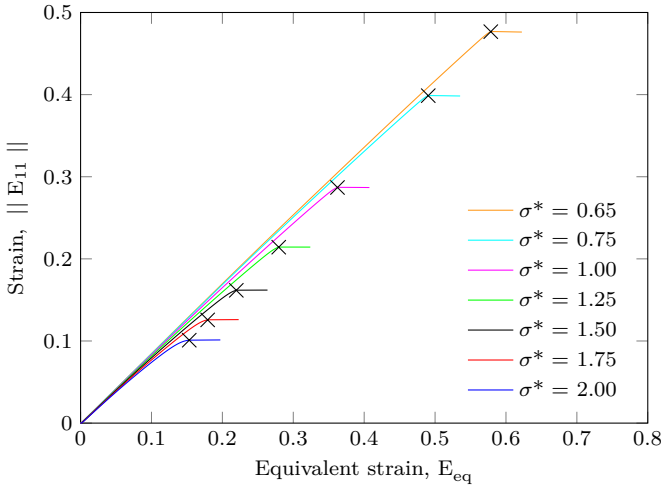

Figure 4.27: *Strain in the x_1-direction vs. equivalent strain for the plane strain cell in tension. The crosses represent the points of coalescence.*

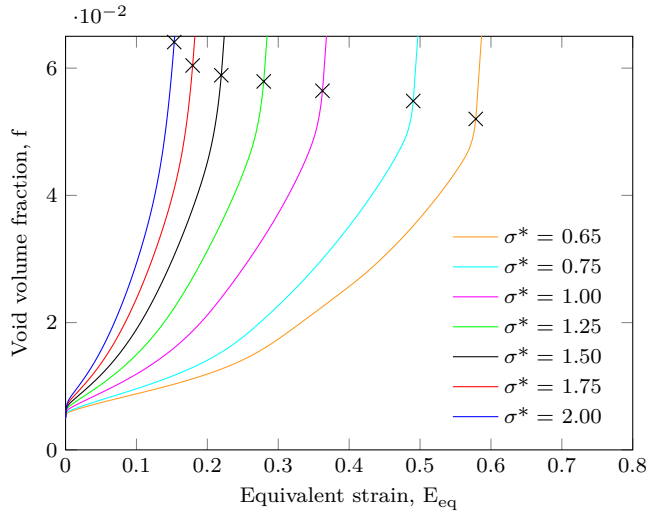

Figure 4.28: *Void volume fraction vs. equivalent strain for the plane strain cell in tension. The crosses represent the points of coalescence.*

The void volume fraction versus equivalent strain curves for the plane strain cell are presented in Figure 4.28. It is seen that the shape of the plane strain curve has a distinct kink at the point of coalescence for low triaxialities. The same tendency is spotted in the equivalent stress versus equivalent strain curve in Figure 4.29. Figures 4.30 and 4.31 present the critical void volume fraction and critical equivalent strain versus triaxiality

ratio, respectively. The critical void volume fraction is observed to be relatively constant, with a slightly increasing value for increased triaxiality ratio. The equivalent strain has an exponentially decreasing curve for increased triaxiality, which is as expected.

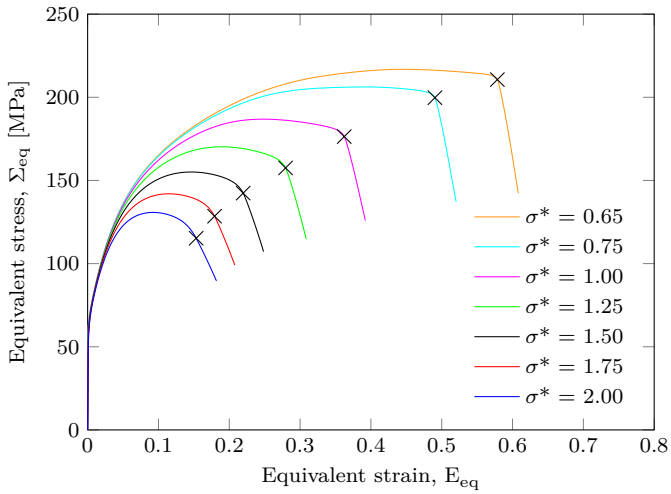

Figure 4.29: *Equivalent stress vs. equivalent strain for the plane strain cell in tension. The crosses represent the points of coalescence.*

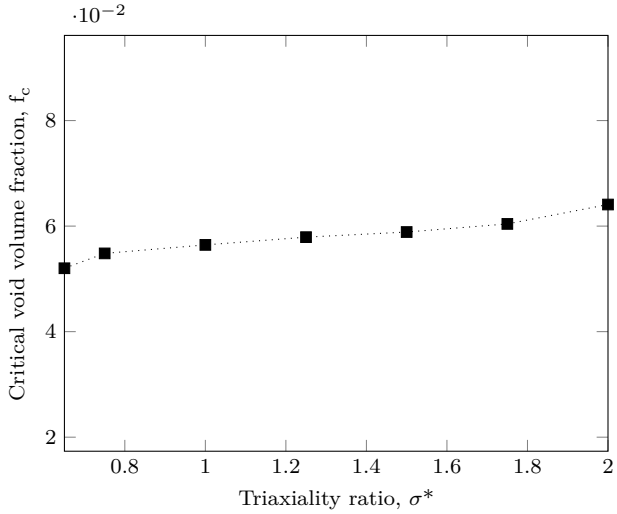

Figure 4.30: *Critical void volume fraction vs. triaxiality ratio for the plane strain cell in tension.*

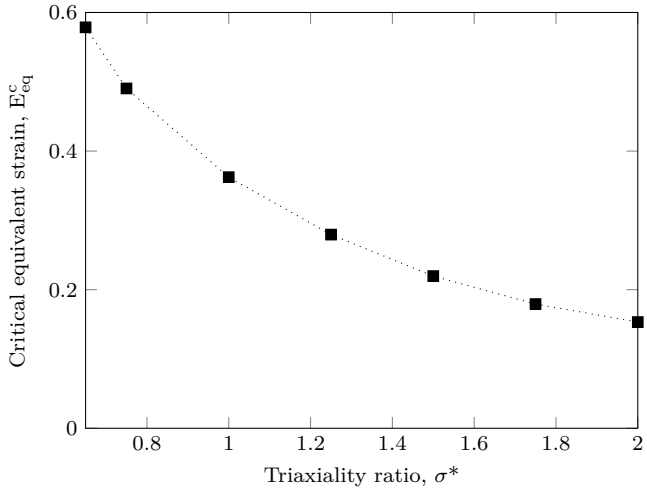

Figure 4.31: *Critical equivalent strain vs. triaxiality ratio for the plane strain cell in tension.*

4.3.2 Plane Strain Shear Cell

A plane strain shear unit cell model was established to achieve information on coalescence for very low triaxialities. The shear cell yield a triaxiality ratio $\sigma^* \simeq 0$ [50], and will therefore only give one additional point to the critical equivalent strain curves presented in the previous section.

The deformation of the shear unit cell is illustrated in Figure 4.32. The growth of the void is more evident in Figure 4.33, that shows the section closest to the particle. As mentioned in Section 4.1, the vertical edges remain linear before coalescence. When approaching coalescence, a shear band form around the middle of the vertical edges. This is clearly seen in the rightmost picture in Figure 4.32. Regarding the void growth, it is seen that the void deforms along a shear band similar to what is presented in Figure 2.5 in Section 2.2.3.

Figure 4.32: *Deformation of the shear unit cell. Triaxiality ratio* $\sigma^* \simeq 0$.

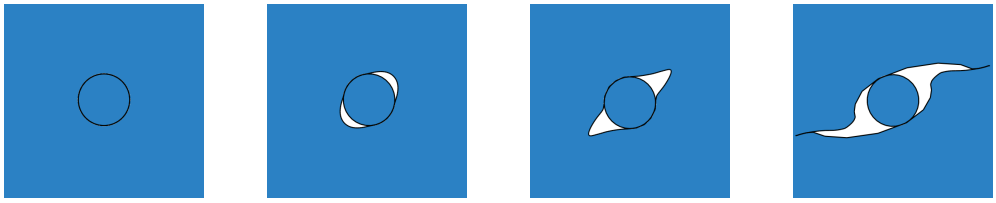

Figure 4.33: *Void growth for the shear unit cell. The pictures show a magnification of the section closest to the particle.*

The coalescence criterion for the shear cell was established on the basis of the formed shear band, as shown in Figure 4.34. The displacement in the x_1-direction was extracted for two nodes along the vertical edge. These nodes are marked with red dots in the figure. Coalescence is defined when Δ is larger than 10 % of the side length, i.e., $\Delta > 0.2$ yield coalescence. The equivalent strain is calculated by using the following expression

$$E_{eq} = \frac{1}{\sqrt{3}}\gamma \tag{4.3}$$

where γ is the shear strain, illustrated in Figure 4.34.

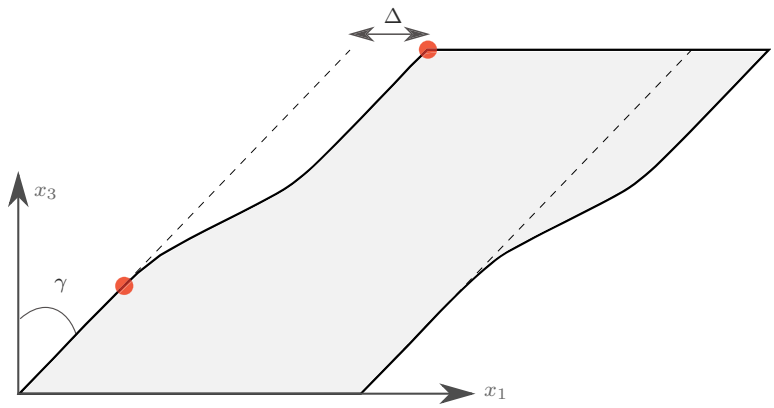

Figure 4.34: *Coalescence criterion for the shear cell.*

Figure 4.35 illustrates the critical equivalent strain for the plane strain cells. The value for $\sigma^* = 0$ is given from the shear cell analysis, and the remaining represents the plane strain cell analyses. As seen in the figure, the critical equivalent strain for $\sigma^* = 0$ is situated below higher triaxiality ratios, and does not follow the same exponential path as the results from the plane strain cell. This is in agreement with a study by Nahshon and Hutchinson [18].

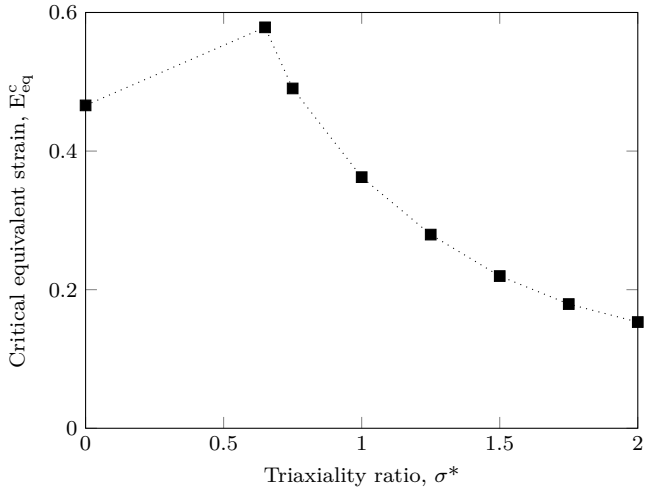

Figure 4.35: *Critical equivalent strain vs. triaxiality ratio for the two plane strain cells.*

4.4 Discussion

By studying the deformation of the different cells it is seen that the cells subjected to tension get similar deformation modes. Coalescence is fairly easy to define, both from the deformation itself and by studying the development of strains. The axisymmetric cell in generalized compression on the other hand, does not yield a deformation mode similar to the other axisymmetric loading case, and coalescence cannot be defined on the same basis. The shear cell yields a typical shear deformation mode, and cannot be directly compared with the other unit cell deformations.

By including GTN in the matrix for both axisymmetric loading cases, the critical void volume fraction and the critical equivalent strain decreases. This is considered realistic since a larger volume fraction in the matrix will yield coalescence for lower strains. When comparing the change in the critical equivalent strain for the same loading cases with GTN in the matrix, presented in Figures 4.14 and 4.24, relatively good correspondence is observed. For both loading cases, the curve with GTN in the matrix is situated below the von Mises curve and have the same shape. There is however larger discrepancy between the curves for generalized compression.

The reason for this discrepancy may be that high void volume fractions occur in the unit cell matrix relatively early in the deformation process, for generalized compression. This is clearly shown in Figure 4.22. This means that secondary voids form in the matrix before coalescence of primary voids occur. In reality, it is believed that secondary voids coalesce in the matrix where the void volume fraction is approximately equal to 0.66. One reason for the rapid growth in void volume fraction in the matrix is the values of the GTN parameters q_1 and q_2. As mentioned, standard Tvergaard parameters were used for these

analyses. It was discovered that by decreasing q_1, the secondary void growth decreased and the cell could be stretched further. This may indicate that the use of the standard Tvergaard parameters is not optimal for generalized compression. In addition, it may seem like secondary voids are more significant for generalized compression, as discussed in Section 4.2.2.1.

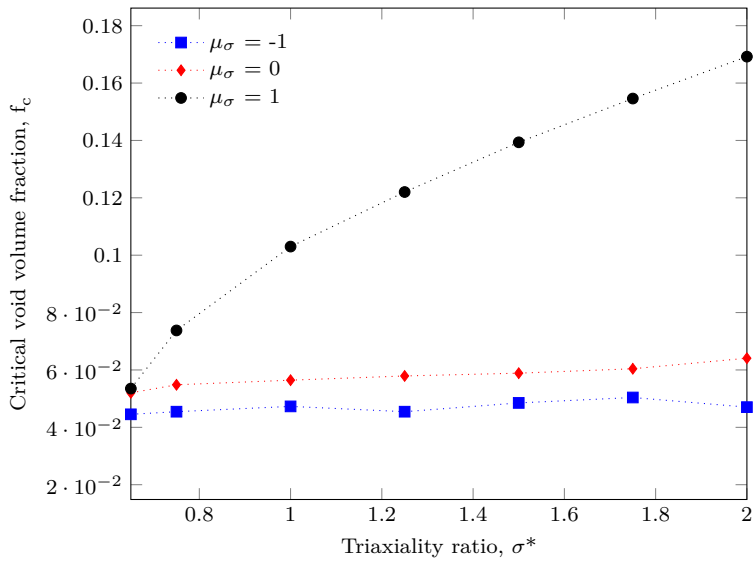

Figure 4.36: *Critical void volume fraction vs. triaxiality ratio for generalized tension ($\mu_\sigma = -1$), plane strain ($\mu_\sigma = 0$) and generalized compression ($\mu_\sigma = 1$), with von Mises in the matrix.*

Figure 4.36 presents the critical void volume fraction for generalized tension, plane strain and generalized compression unit cells with a von Mises matrix material. As seen in the figure, both generalized tension and plane strain yield a relatively constant critical value, while generalized compression have an increasing value with increasing triaxiality ratios. These discrepancies for high triaxialities may be due to a physical phenomenon for generalized compression, or discrepancies between the coalescence criteria.

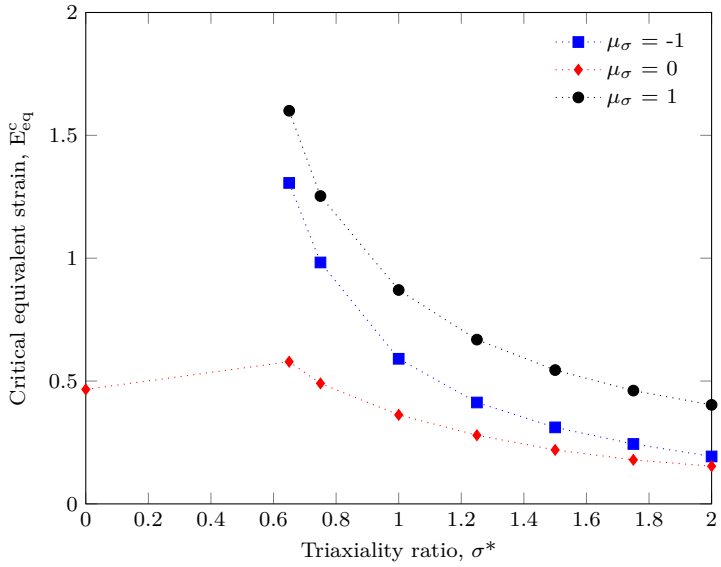

Figure 4.37: *Critical equivalent strain vs. triaxiality ratio for generalized tension ($\mu_\sigma = -1$), plane strain tension ($\mu_\sigma = 0$) and generalized compression ($\mu_\sigma = 1$), with von Mises in the matrix.*

When comparing the critical equivalent strain versus triaxiality ratio curves for the three cells, presented in Figure 4.37, it is seen that the plane strain cell yield much lower critical equivalent strains than the other cases. A triaxiality of $\sigma^* = 0.65$ results in an equivalent strain of approximately 0.6 for the plane strain cell, while the axisymmetric cell give 1.3 and 1.6 for generalized tension and compression, respectively. The tendency of the curves are the same for all loading cases. This is as expected, based on a preliminary study by Dæhli [51] using 3D cells. One major difference is that the curve for generalized shear is situated below the generalized tension curve.

Figure 4.38 compares the 2D cell analyses presented in this chapter with data obtained from 3D unit cell analyses. As seen in the figure, there are only small discrepancies between the 2D and 3D curves for generalized tension and compression. The 2D curve for plane strain is observed to be situated below the curves for the axisymmetric cell. This is not in accordance with Dæhli's study, where the curve for $\mu_\sigma = 0$ is situated between $\mu_\sigma = -1$ and $\mu_\sigma = 1$. Note that the value given by the 2D shear cell is almost identical to the 3D cell.

The reason why the 2D curve for $\mu_\sigma = 0$ is situated below the curve for $\mu_\sigma = -1$ is believed to be due to the properties of the plane strain cell. As mentioned in Section 4.1 the plane strain cell has a cylindrical void, while the axisymmetric and 3D unit cell voids are spherical. Gao and Kim [19] studied the effect of different void shapes, and concluded that the shape of the void had a significant influence on the critical equivalent strain. Since the void in our plane strain cell has a different shape than the axisymmetric

cells, the data cannot be directly compared. The plane strain cell corresponds to an infinitely long hexahedron with an infinitely long cylindrical void. The cells can therefore not be assembled in an array, and hence the plane strain cell cannot be considered a real computational cell. The data from the 2D plane strain cell is not comparable with the 3D cell in this case.

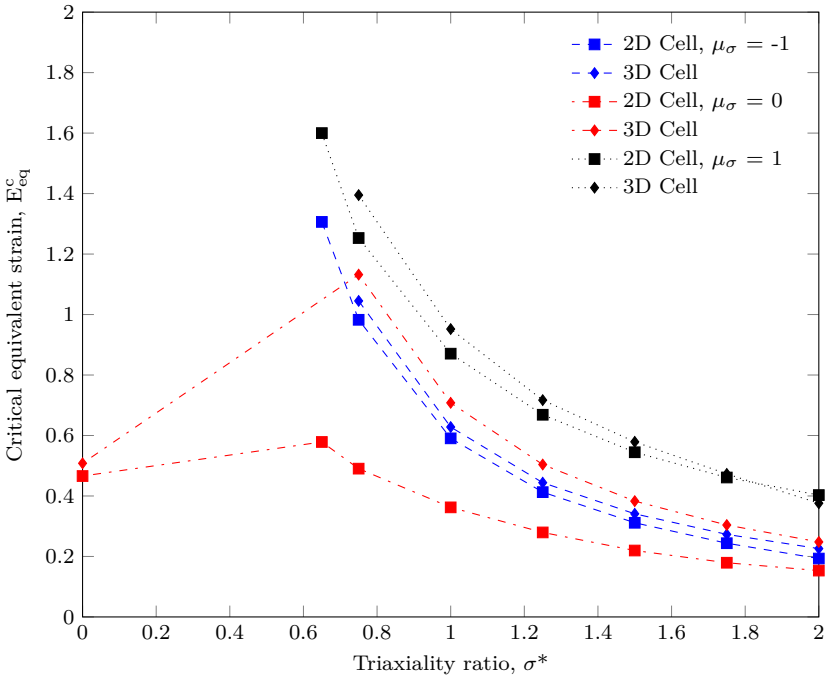

Figure 4.38: *Comparison of critical equivalent strain vs. triaxiality ratio for generalized tension ($\mu_\sigma = -1$), generalized shear ($\mu_\sigma = 0$) and generalized compression ($\mu_\sigma = 1$) in 2D and 3D, with von Mises in the matrix. The 3D cell data is obtained from Dæhli [51].*

Regarding the point given by the shear cell analysis, it is seen that the value is below what could be expected, based on the exponential trend of the curve. As mentioned, this tendency is in agreement with earlier published studies [18, 53, 54]. The values given from the generalized shear cells in 2D and 3D, with triaxiality $\sigma^* = 0$, are in accordance. The same cannot be seen for other triaxialities.

5 Calibration of Fracture Models

In this chapter, three different fracture models are calibrated with the main purpose of connecting the results from the microscopic unit cell study, presented in Chapter 4, with macroscopic fracture models. First, a section is dedicated to calibration of the Cockcroft-Latham fracture model, based on both computational cells and tensile tests. Further, two sections present calibration of the Johnson-Cook fracture model from the computational cells, as well as a comparison of the CL and JC models for tensile tests. Additionally, calibration of the Gurson-Tvergaard-Needleman fracture model to the computational cell data is presented. Lastly, a section is devoted to discussion of the results.

5.1 The Cockcroft-Latham Fracture Model

The Cockcroft-Latham fracture model was calibrated using both results from the computational cell study, as well as data from tensile tests adopted from Westermann et al. [41].

5.1.1 Calibration based on Computational Cells

Figures 5.1 and 5.2 illustrate the fracture surfaces obtained by using a least-square algorithm to fit the Cockcroft-Latham fracture model to the computational cell data. Note that $H(p_f)$ is defined as in Equation 2.33. The surface in Figure 5.1 represents all investigated Lode parameters, while the data for $\mu_\sigma = 0$ have been excluded in Figure 5.2. The reason why a comparison of fracture surfaces with and without the data for $\mu_\sigma = 0$ was conducted, has to do with the properties of the two-dimensional plane strain unit cell. This is discussed in Section 5.5.

By investigating the figures, it is seen that the two cases yield close to identical fracture surfaces. The surface including the data for $\mu_\sigma = 0$ is observed to have better correspondence with the cell data for high triaxialities, while the data excluding $\mu_\sigma = 0$ show better agreement for low triaxialities. This is a result of the downward translation of the fracture surface, due to lower critical equivalent strains for $\mu_\sigma = 0$ than for $\mu_\sigma = -1$ and $\mu_\sigma = 1$.

Equations 2.32 and 2.33 in Section 2.2.6.1 were used to calibrate the fracture parameters. Some deviation is observed between the cases, with $W_c = 318.9$ MPa including $\mu_\sigma = 0$ and $W_c = 364.3$ MPa excluding $\mu_\sigma = 0$. This discrepancy indicates that by including $\mu_\sigma = 0$ we obtain both lower W_c and an overall lower critical equivalent strain E^c_{eq}. Based on the results presented in Chapter 4, this is as expected.

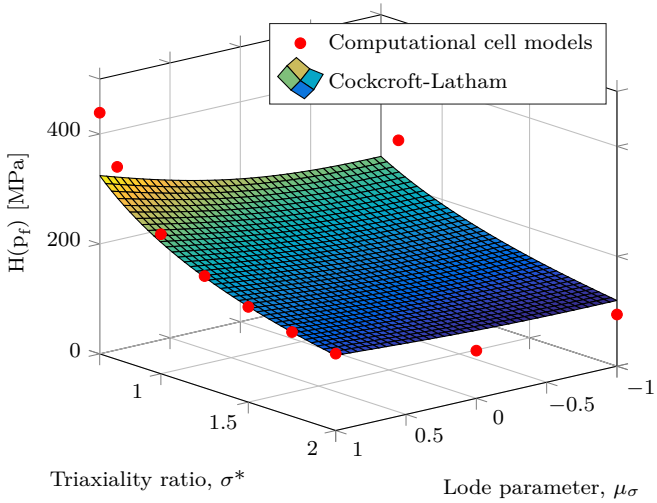

Figure 5.1: *Fracture surface for the Cockcroft-Latham fracture model calibrated to the computational cell data with a von Mises yield criterion.* $W_c = 318.9$ *MPa.*

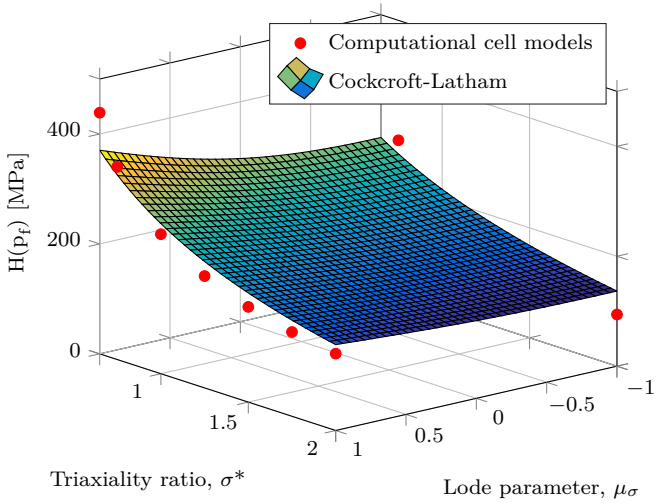

Figure 5.2: *Fracture surface for the Cockcroft-Latham fracture model calibrated to the computational cell data with von Mises yielding, excluding the data for* $\mu_\sigma = 0$. $W_c = 364.3$ *MPa.*

5.1.2 Calibration based on Computational Cells with GTN

The Cockcroft-Latham fracture model was also calibrated to the computational cell data with GTN in the matrix. The three-dimensional fracture surface is shown in Figure 5.3. Note that this calibration does not include values for generalized shear, i.e., $\mu_\sigma = 0$.

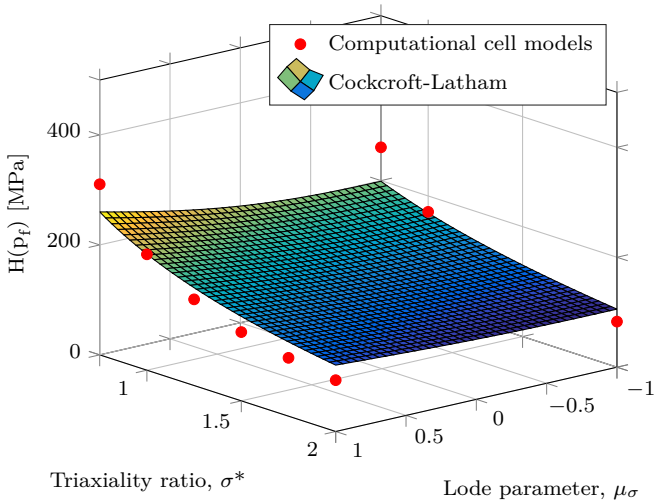

Figure 5.3: *Fracture surface for the Cockcroft-Latham fracture model calibrated to the computational cell data with GTN in the matrix.* $W_c = 281.7$ *MPa.*

The shape of the fracture surfaces is almost identical for all cases; the only difference being the elevation of the surface which is controlled by the fracture parameter W_c. Implementation of GTN in the matrix results in a lower fracture parameter $W_c = 281.7$ MPa, which is as expected based on the results presented in Chapter 4. Comparison with the fracture surfaces shown in Figures 5.1 and 5.2, reveals that the surface for GTN calibration is translated downwards. This corresponds to lower critical equivalent strains. As for the fracture surface with the von Mises yield criterion excluding $\mu_\sigma = 0$, better correspondence with the cell data is seen for lower triaxialities. Note that the computational cells with GTN in the matrix does not include triaxiality $\sigma^* = 0.65$.

5.1.3 Calibration based on Tensile Tests

To calibrate the Cockcroft-Latham fracture model to the experimental tensile test data, a model was made of the test specimen illustrated in Figure 3.3 in Section 3.2.1 using IMPETUS Afea Solver. One eighth of the three-dimensional specimen was modelled to save computational time. Figures 5.4 and 5.5 illustrate the mesh of the whole specimen and the cross-sectional mesh at two locations, respectively. Note that the specimen shown in Figure 5.4 is mirrored about the x-, y- and z-axes. 64-node cubic hexahedral elements were used in the gauge section, and linear 8-node hexahedral elements for the remaining parts. The analysis was performed using an explicit integration scheme with time scaling. To ensure quasi-static loading conditions as in the real experiments the kinetic energy was checked, and observed to be considerably lower than the plastic work. This indicates that there were no unwanted dynamic effects in the analysis, and the time scaling used was therefore considered reasonable.

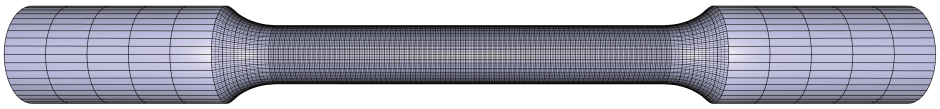

Figure 5.4: *Mesh of the tensile specimen in IMPETUS.*

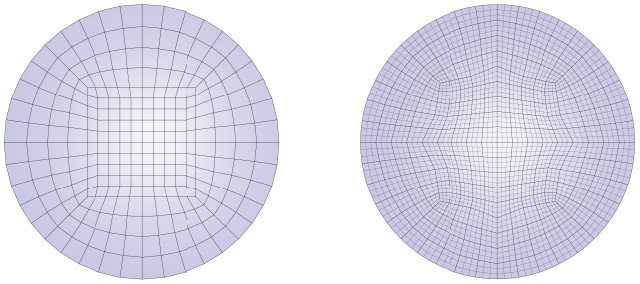

(a) *Grip section.* ***(b)*** *Gauge section.*

Figure 5.5: *Mesh of the tensile specimen cross-section at two different locations.*

Figure 5.6 shows a comparison of the force-displacement data obtained from the IMPETUS analysis and the experimental data. As seen, the correspondence between the two curves is good. The purpose of this comparison was to establish the point of fracture, as this was needed further to calibrate the Cockcroft-Latham fracture model.

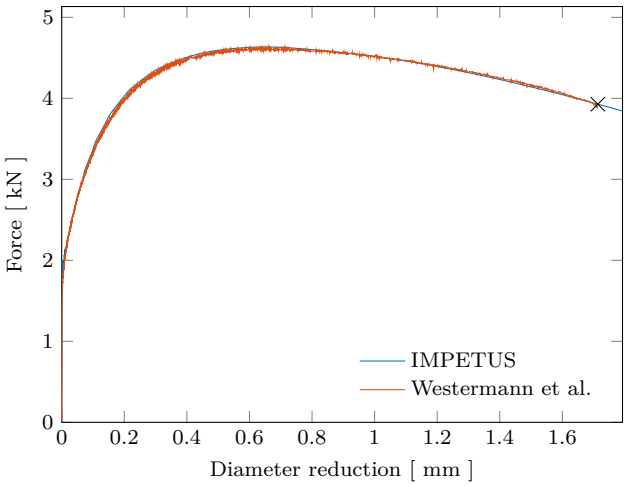

Figure 5.6: *Comparison of data from tensile test in IMPETUS and experimental data given by Westermann et al. [41]. The point of fracture is marked by a cross.*

The curve presented in Figure 5.7 shows the development of the maximum principal stress in the critical element in the tensile specimen. The critical element is shown in Figure

5.8. The point of fracture, obtained from the force-displacement curve in Figure 5.6, was used to determine failure in the IMPETUS model. The area below the curve represents the fracture parameter W_c, which for the tensile test equals $W_c = 174.1$ MPa. This value is considerably lower than the values obtained from the computational cell study.

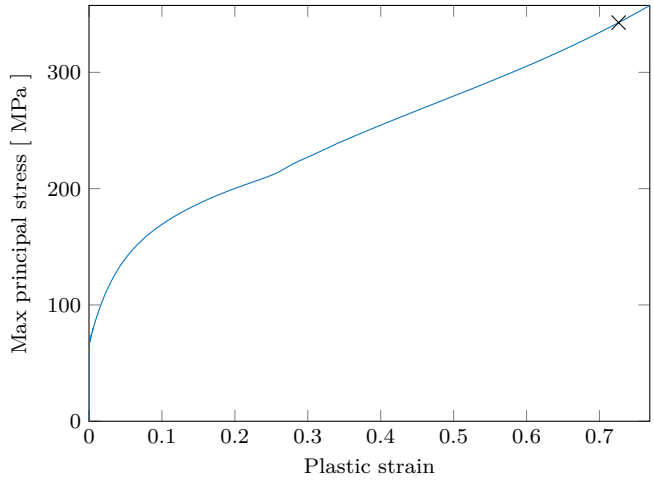

Figure 5.7: *Development of the maximum principal stress in the critical element from the tensile test in IMPETUS. The area below the curve yield a fracture parameter $W_c = 174.1$ MPa. The point of fracture is marked by a cross.*

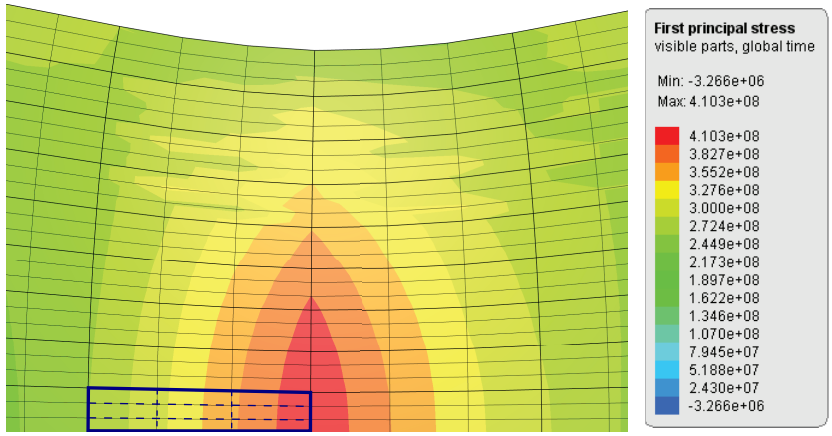

Figure 5.8: *Critical element in the necked region during tensile test analysis in IMPETUS.*

5.2 The Johnson-Cook Fracture Model

The Johnson-Cook fracture model was calibrated using results from the computational cells, both with and without GTN in the matrix. One of the main objectives of this thesis was to calibrate the fracture models without extensive material testing. Therefore, no calibration was done using tensile test data, since the JC model needs to be calibrated using a variety of tensile tests to achieve data for several triaxialities and Lode parameters.

5.2.1 Calibration based on Computational Cells

Figures 5.9 and 5.10 illustrate the fracture surface for the Johnson-Cook fracture model with and without data for $\mu_\sigma = 0$, respectively. The surfaces were obtained by using a least-square algorithm. By investigating the surfaces, it is clear that the data for the plane strain cell have considerable influence on the shape of the fracture surface.

As seen in Figure 5.9, which include data from all three computational cells, the JC fracture surface is highly dependent on the Lode parameter. By studying Equations 2.35 and 2.36 in Section 2.2.6.2, it is seen that the Johnson-Cook model is symmetric about $\mu_\sigma = 0$. If the data from $\mu_\sigma = 0$ is excluded, as in Figure 5.10, the fracture surface is seen to be independent of the Lode parameter. The surfaces show equally good correspondence with the cell data for $\mu_\sigma = -1$ and $\mu_\sigma = 1$ for all triaxialities, which is as expected.

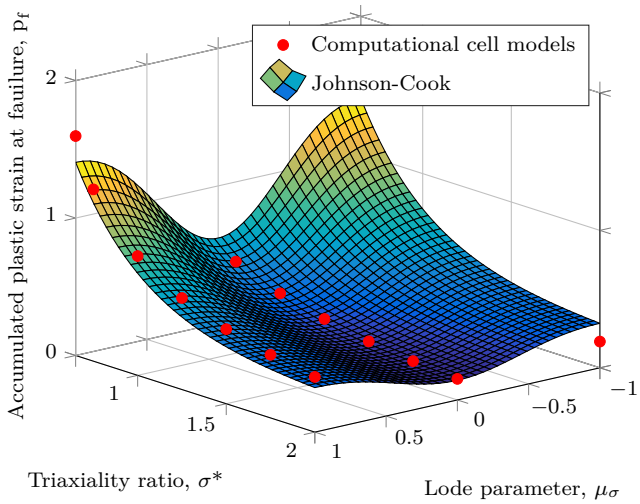

Figure 5.9: *Fracture surface for the Johnson-Cook fracture model calibrated to the computational cell data with a von Mises yield criterion. Fracture parameters:* $D_1 = 0.2894$, $D_2 = 5.9502$, $D_3 = -2.5746$, $D_4 = D_5 = 0$ *and* $D_6 = 0.5592$.

The fracture parameters for the two cases are presented in Table 5.1. The major difference is seen in the value of D_6, which is equal to zero if the data for $\mu_\sigma = 0$ are excluded. This

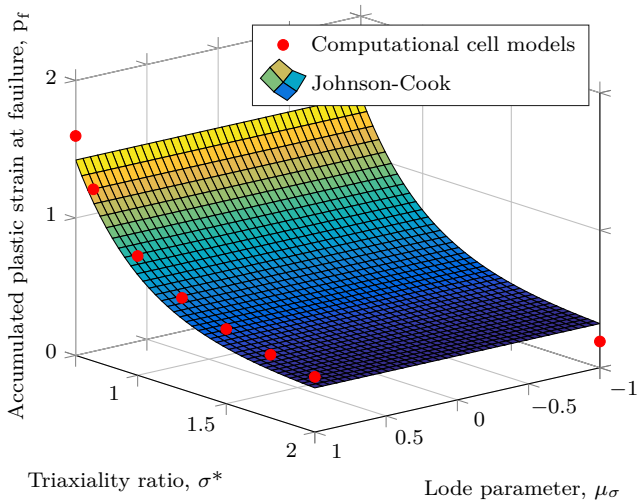

Figure 5.10: *Fracture surface for the Johnson-Cook fracture model calibrated to the computational cell data with a von Mises yield criterion, excluding the data for* $\mu_\sigma = 0$. *Fracture parameters:* $D_1 = 0.2894$, $D_2 = 5.9502$, $D_3 = -2.5746$ *and* $D_4 = D_5 = D_6 = 0$.

verifies the Lode independence mentioned above. Note that the parameters connected to the temperature and strain rate terms in the Johnson-Cook model, D_4 and D_5, are set to zero since the computational cells are modelled using temperature and strain rate independent data. Hence, the fracture surface is independent of these parameters.

Table 5.1: *Johnson-Cook fracture parameters from calibration to the computational cells.*

	D_1	D_2	D_3	D_4	D_5	D_6
With $\mu_\sigma = 0$	0.2894	5.9502	-2.5746	0	0	0.5592
Without $\mu_\sigma = 0$	0.2915	6.5091	-2.6940	0	0	0

5.2.2 Calibration based on Computational Cells with GTN

The fracture surface for calibration of the JC model to the computational cell data with GTN in the matrix is shown in Figure 5.11. Note that the calibration was done to the axisymmetric cells only, ergo $\mu_\sigma = 0$ has not been included.

By studying the fracture surface, it is seen that the surface is similar to the one with the von Mises yield criterion, excluding $\mu_\sigma = 0$, shown in Figure 5.10. The same tendency is seen as for CL regarding lower critical strains and lower values for the JC fracture parameters with GTN in the matrix. Note that even though the fracture surfaces in both Figures 5.10 and 5.11 are Lode independent, the slopes and the accumulated plastic strains at failure are different. The discrepancies observed in the slopes may be due to

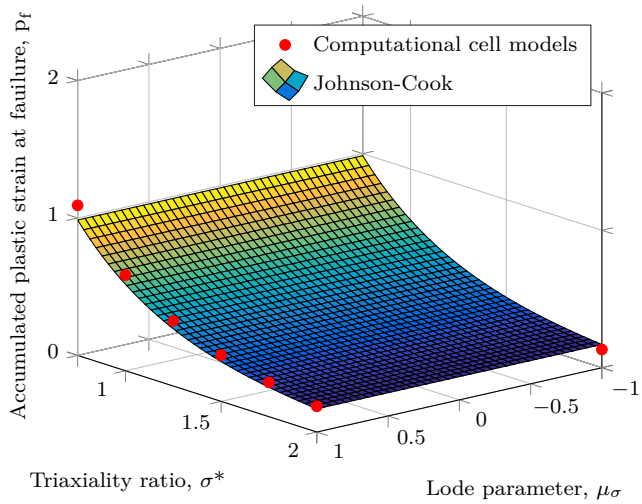

Figure 5.11: *Fracture surface for the Johnson-Cook fracture model calibrated to the computational cell data with GTN in the matrix, excluding the data for* $\mu_\sigma = 0$*. Fracture parameters:* $D_1 = 0.1023$*,* $D_2 = 4.1555$*,* $D_3 = -2.0653$ *and* $D_4 = D_5 = D_6 = 0$*.*

the fact that $\sigma^* = 0.65$ was not included for the analyses with GTN in the matrix. The fracture parameters are presented in Table 5.2.

Table 5.2: *Johnson-Cook fracture parameters from calibration to the computational cells with GTN in the matrix.*

	D_1	D_2	D_3	D_4	D_5	D_6
GTN without $\mu_\sigma = 0$	0.1023	4.1555	-2.0653	0	0	0

5.3 Tensile Test Comparison

To compare the CL and JC fracture models, tensile tests were conducted using IMPETUS and the calibrated fracture parameters. The force-displacement curves from the tensile tests are presented in Figure 5.12.

As shown in the figure, CL with $W_c = 174.1$ MPa, obtained from calibration to the tensile tests, shows good correspondence with the experimental results from Westermann et al. [41]. This is as expected, since the calibration was done against the data from Westermann et al. Both the curve for CL with $W_c = 364.3$ MPa and JC with a von Mises yield criterion in the computational cell matrix have fracture occurring at a later time. This is due to the magnitude of the fracture parameters, which yield larger critical equivalent strains. There is, although, relatively good correspondence between the models. This is as anticipated, since both models have been calibrated to the same computational cell data.

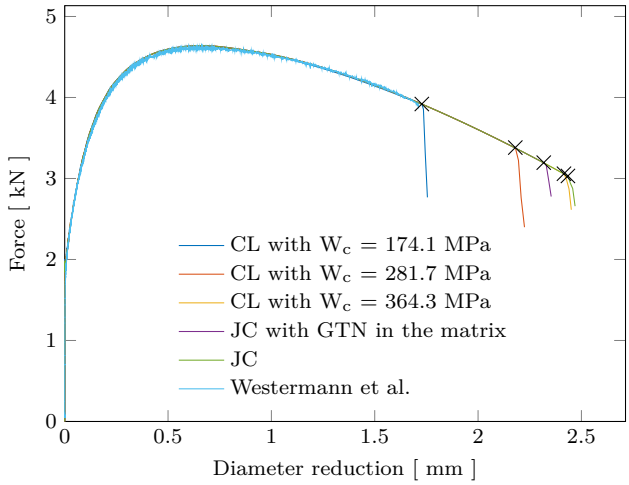

Figure 5.12: *Comparison of the Cockcroft-Latham and Johnson-Cook fracture models for tensile tests, with experimental data from Westermann et al. [41]. The crosses represent the points of failure.*

Investigation of the curves reveals that the JC curves have failure occuring at a later time than CL both with von Mises and GTN in the computational cell matrix. The small discrepancies observed with von Mises is probably due to different definitions of the fracture surface. The curves for GTN in the matrix are observed to have failure at lower strains for both fracture models. As mentioned, this in accordance with the tendency seen in the computational cell study in Chapter 4. There is although larger discrepancies between CL and JC with GTN in the matrix than with von Mises. One possible reason for this is that the triaxiality ratio $\sigma^* = 0.65$ was not included in the analyses with GTN, which may lead to a larger difference for lower triaxialities, such as for a tensile test.

5.4 The Gurson-Tvergaard-Needleman Model

The GTN model was calibrated to the computational cell data with the main goal of using GTN in the ballistic impact analyses in IMPETUS and Abaqus. The GTN parameters, presented in Equation 2.39 in Section 2.2.7.1, were only calibrated for an axisymmetric cell in generalized tension.

The analyses were run using a one-element axisymmetric model made in Abaqus, with an 8-node quadratic axisymmetric element with full integration. The Voce parameters of the AlMgSi-alloy were used, as well as an initial void volume fraction of $f_0 = 5 \cdot 10^{-3}$. The GTN model in Abaqus was used to vary the void growth parameters q_1 and q_2. The element, with boundary and loading conditions, is shown in Figure 5.13. As seen, the left and bottom edges were fixed, while surface tractions were applied on the top and right edges, using the static Riks algorithm in Abaqus. Constraints were applied on the top

and right edges, by constraining all nodes to the top right node, to ensure straight edges during deformation. Note that unlike the unit cell models presented in Chapter 4, this model does not include a primary void in the centre.

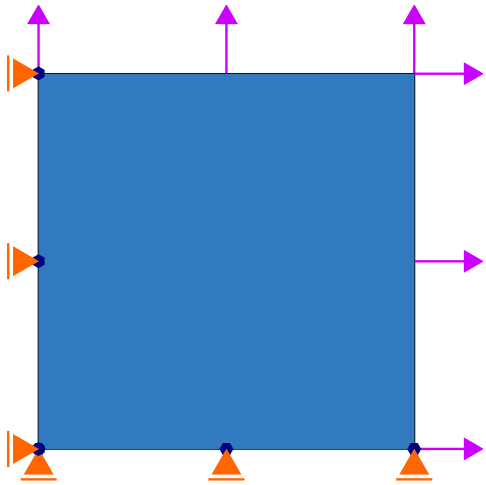

Figure 5.13: *Boundary and loading conditions for the one-element model used in calibration of the GTN parameters.*

Figure 5.14 illustrates the deformed cell for triaxiality ratio $\sigma^* = 2$, using standard Tvergaard parameters $q_1 = 1.5$ and $q_2 = 1.0$. The third picture from the left is taken right after coalescence. It is observed that the deformation is similar to the deformation of the axisymmetric unit cell in generalized tension, presented in Figure 4.6 in Section 4.2.1. Considering that the one-element model also is an axisymmetric model in generalized tension makes this deformation reasonable. Coalescence has therefore been defined on the same basis for this one-element model, i.e., once a uniaxial deformation mode occurs.

Figure 5.14: *Deformation of the one-element model with GTN in the matrix for triaxiality ratio* $\sigma^* = 2$. $q_1 = 1.5$ *and* $q_2 = 1.0$.

5.4.1 Calibration of the Gurson-Tvergaard-Needleman Model

To get good correspondence between the GTN model and the computational cell data, the GTN parameters were varied separately to investigate the influence of each parameter. It was concluded that it was most important to get good correspondence with the cell data for low triaxialities, since very low triaxialities are expected for the experimental tests.

By studying Equation 2.42 in Section 2.2.7.1, it is seen that both parameters influence the void growth. The equation contains a hyperbolic sine function that includes the second GTN parameter q_2 and the triaxiality ratio σ^*, which means that the value of q_2 governs the change in void growth for different triaxialities. It can also be seen that several combinations of q_1 and q_2 may give relatively good correspondence with the cell data for a given triaxiality. Note that what may be a good combination for low triaxialities not necessarily yield good correspondence for high triaxialities, and vice versa. It is therefore desirable to find a combination of the parameters that give good match with the cell data for all triaxialities, with the main focus on the lower triaxialities.

Figure 5.15 illustrates the void volume fraction versus equivalent strain for various values of q_1 for triaxiality ratio $\sigma^* = 1$ and $q_2 = 1.00$. As seen in the figure, lower values of q_1 give better correspondence with the computational cell data. Quite large discrepancies are seen between the curves for $q_1 = 1.75$ and $q_1 = 0.80$. Observations reveal that the Tvergaard parameters of $q_1 = 1.50$ and $q_2 = 1.00$ are not optimal for this computational cell study.

The curve for $q_1 = 1.16$ is considered the best option, due to good correspondence with the cell data for low strains as well as an intersection close to the point of coalescence. Note that the void volume fraction presented in the figure represents the average value of the void volume fraction in all nine integration points.

By studying the curves in Figure 5.15 it is seen that the computational cell curve has a rather gentle incline up to the point of coalescence, and a low value of q_1 is therefore desirable. Figure 5.16 illustrates the effect of the q_2 parameter for triaxiality ratio $\sigma^* = 1$. The lowest value for q_1 presented in Figure 5.15 was chosen to better illustrate the effect of a change in q_2. By increasing q_2, more rapid increase in the slope is seen and quite good correspondence with the cell data can be achieved. This is as expected, based on Equation 2.42. For a value of $q_1 = 0.80$, the curve for $q_2 = 1.15$ is considered to have the best fit to the cell data.

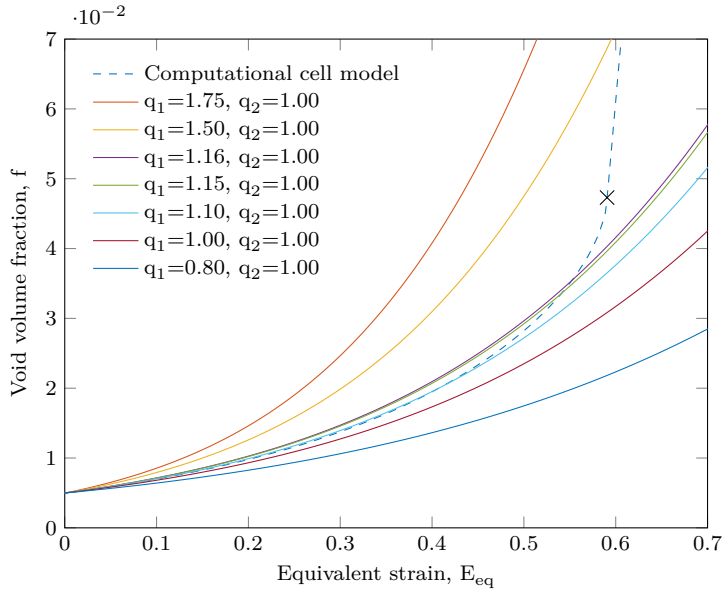

Figure 5.15: *Influence of GTN parameter q_1 for triaxiality ratio $\sigma^* = 1$.*

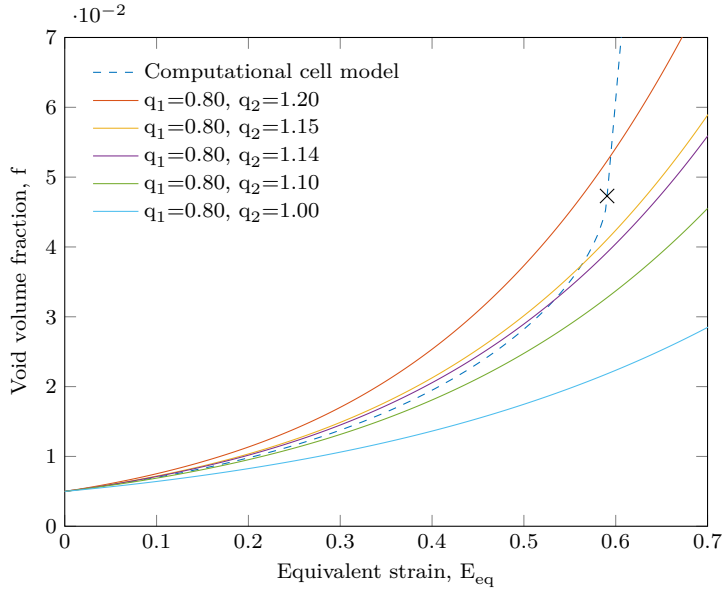

Figure 5.16: *Influence of GTN parameter q_2 for triaxiality ratio $\sigma^* = 1$.*

Based on the curves presented in Figures 5.15 and 5.16, the following combinations of GTN parameters were considered the best fit for $\sigma^* = 1$; $q_1 = 1.16$ and $q_2 = 1.00$ and $q_1 = 0.80$ and $q_2 = 1.15$. Figure 5.17 illustrates the development in void volume fraction for triaxiality ratios in the range $0.75 < \sigma^* < 2.00$ for $q_1 = 1.16$ and $q_2 = 1.00$. The dashed lines represent the computational cell data for the given triaxiality. It is seen that all curves lie on the left side of the corresponding computational cell curves before coalescence, and relatively good correspondence is achieved for all triaxialities. This is considered good. Note that triaxiality ratio $\sigma^* = 0.65$ has not been included, because coalescence could not be reached within acceptable straining.

Figure 5.18 shows the void volume fraction for all triaxialities for $q_1 = 0.80$ and $q_2 = 1.15$. Only small discrepancies are observed, and all curves lie on the left side of the computational cell curves before coalescence.

When comparing the curves presented in Figures 5.17 and 5.18 it is seen that the overall best fit was obtained with GTN parameters of $q_1 = 1.16$ and $q_2 = 1.00$. The main arguments for this are better correlation for higher triaxialities, as well as intersection points closer to the point of coalescence for low triaxialities.

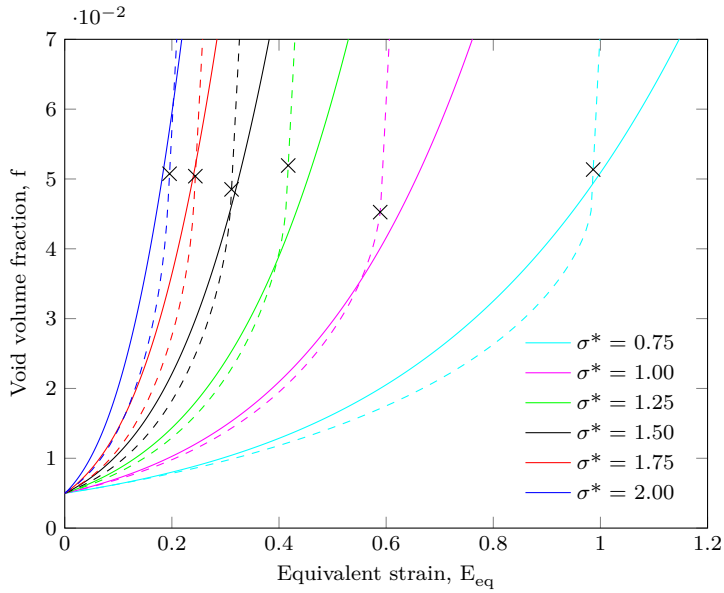

Figure 5.17: *Development in void volume fraction with GTN parameters* $q_1 = 1.16$ *and* $q_2 = 1.00$*, compared to computational cells, for triaxialities in the range* $0.75 < \sigma^* < 2.00$.

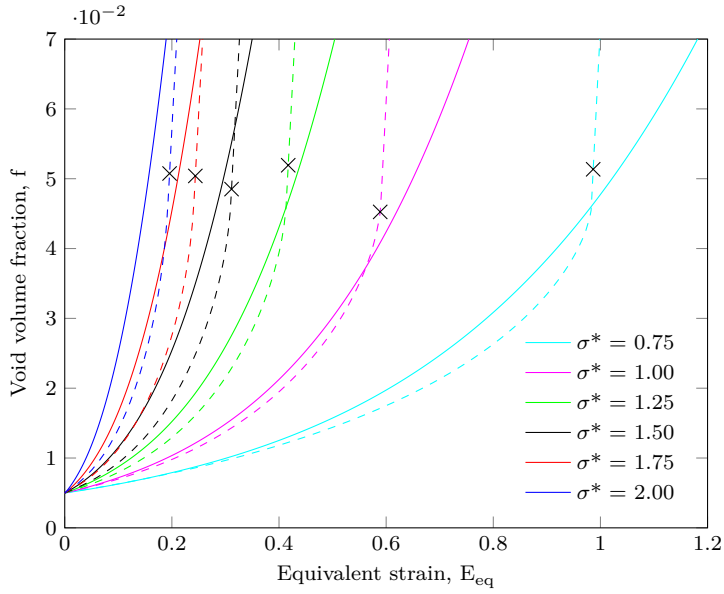

Figure 5.18: *Development in void volume fraction with GTN parameters* $q_1 = 0.80$ *and* $q_2 = 1.15$*, compared to computational cells, for triaxialities in the range* $0.75 < \sigma^* < 2.00$*.*

5.4.2 Calibration of the Modified Gurson Model with Shear Softening

The perforation process is believed to be highly sensitive to shear, such that to properly model the penetration of the AlMgSi-target using an ogival shaped bullet, the effects of shear softening should be included. The modified Gurson model, presented in Section 2.2.7.2, was calibrated to the computational cell data to obtain the value of the shear constant k_s. The shear constant was found using the following expression proposed by Nahshon and Hutchinson [18]

$$k_s = \frac{1}{E^c_{eq}} \ln\left(\frac{f_c}{f_0}\right) \tag{5.1}$$

Naturally, the model was calibrated using only the plane strain shear cell data. The shear cell analysis resulted in a critical equivalent strain of $E^c_{eq} = 0.4659$, and a critical void volume fraction for $\mu_\sigma = 0$ equal to $f_c = 0.0578$. Note that the critical void volume fraction is the average value for all tested triaxialities for the plane strain cell. With an initial void volume fraction $f_0 = 0.005$, this resulted in a shear parameter $k_s = 5.25$. An appropriate value for the shear constant lies in the range $1 \leq k_s \leq 3$ for many structural alloys [18]. The value obtained from these computational cell analyses is above the suggested range. Since only small discrepancies are seen between the 2D and 3D shear cells, as presented in Figure 4.38, the value for the shear constant is assumed to be sufficiently accurate.

5.5 Discussion

Table 5.3 presents the calibrated fracture parameters for the three fracture models studied in this thesis.

Table 5.3: *Fracture parameters for the Cockcroft-Latham, Johnson-Cook and Gurson-Tvergaard-Needleman fracture models, calibrated to both computational cell data (CC) and tensile tests. The calibration to computational cells with GTN does not include $\mu_\sigma = 0$.*

	CL	JC					GTN	
	W_c [MPa]	D_1	D_2	D_3	D_4	D_5	D_6	q_1	q_2
CC with $\mu_\sigma = 0$	318.9	0.2894	5.9502	-2.5746	0	0	0.5592	-	-
CC without $\mu_\sigma = 0$	364.3	0.2915	6.5091	-2.6940	0	0	0	1.16	1.00
CC with GTN	281.7	0.1023	4.1555	-2.0653	0	0	0	-	-
Tensile test	174.1	-	-	-	-	-	-	-	-

By studying the calibration of CL to the computational cell data, it is seen that although the values for $\mu_\sigma = 0$ do not affect the shape of the fracture surface, they have an influence on the fracture parameter W_c. By including data for $\mu_\sigma = 0$ we get a decrease in the fracture parameter from $W_c = 364.3$ MPa to $W_c = 318.9$ MPa. Lower value for the critical plastic work W_c yield failure at lower strains.

When comparing the fracture parameters obtained from the computational cell study and the tensile test, it is seen that W_c for the cell data is approximately twice the value of W_c from the tensile tests. The parameter obtained from the tensile tests is considered to be more realistic due to the fact that the tensile test calibration is based on actual experimental test data, while the simplified cell models only have Voce hardening given by material tests.

According to Hopperstad, a triaxiality ratio of approximately $\sigma^* = 1/3$ can be expected for tensile tests [50]. Low triaxialities are also anticipated for the ballistic impacts. As seen in Figure 4.38, $\sigma^* = 0$ yield low critical strain. Despite the fact that the tensile test is not directly comparable with the ballistic impacts, a fracture parameter of $W_c = 174.1$ MPa seems reasonable.

As mentioned, the fracture parameters obtained from the computational cell study are considered somewhat high, compared to the tensile tests. This may be due to several reasons. First, the computational cell models are two-dimensional simplified models. Furthermore, the cells are modelled including one large primary void, which is not believed to be as realistic for the AlMgSi-alloy. A more reasonable model is believed to include secondary voids in the matrix, and one way of adding this is by including GTN in the matrix. It was shown that GTN in the matrix resulted in lower critical equivalent strains, hence it reduced the value of W_c. This value of $W_c = 281.7$ MPa is believed to be more realistic than with the von Mises yield criterion, but the calibration will not be entirely accurate due to the use of a simplified two-dimensional cell.

The data for $\mu_\sigma = 0$ had significant influence on the fracture surface for the Johnson-Cook model. By excluding the plane strain cell data, the problem becomes independent of the

Lode parameter, and $D_6 = 0$. Only small discrepancies are observed between the other parameters.

The standard Tvergaard parameters were seen to yield relatively poor correspondence with the computational cells, compared to other combinations of q_1 and q_2. It was concluded that several combinations of GTN parameters could give good correspondence with the cell data. Due to a rather gentle incline in the computational cell curve prior to coalescence, lower values of q_1 and q_2 were desirable.

In Chapter 4 it was concluded that a comparison of the two-dimensional axisymmetric and plane strain cells would not be correct, due to the difference in void shapes. Therefore the values from the plane strain cells, i.e., $\mu_\sigma = 0$, has not been included in further analyses in this thesis, except for the GTN model with shear softening. It was, although, included in the calibration of the CL and JC fracture models in this chapter, to investigate the influence of $\mu_\sigma = 0$. When referring to different fracture parameters in Chapters 6 and 7, the values presented in Table 5.4 apply.

Table 5.4: *Cockcroft-Latham, Johnson-Cook and Gurson-Tvergaard-Needleman fracture parameters used in the numerical analyses in Chapters 6 and 7.*

Fracture criterion	Fracture parameter
Cockcroft-Latham	$W_c = 364.3$ MPa and $W_c = 174.1$ MPa
Johnson-Cook	$D_1 = 0.2915$, $D_2 = 6.5091$, $D_3 = -2.6940$, $D_4 = D_5 = D_6 = 0$
Gurson-Tvergaard-Needleman	$q_1 = 1.16$, $q_2 = 1.00$
Modified Gurson	$k_s = 5.25$

6 Preliminary Numerical Study

In this chapter important parameters are studied, element erosion techniques compared and the size of the FE mesh investigated. These factors are discussed in the final section, and form the basis for the numerical model that is established in Chapter 7.

The IMPETUS analyses presented in this thesis were run on a server at NTNU. The IMPETUS server utilizes both GPU and CPU parallelization, and the specifications are presented in Table 6.1. Analyses in Abaqus were run on the computer cluster Snurre at NTNU, with the specifications shown in Table 6.2. Note that the computer cluster Snurre utilizes only CPU parallelization.

Table 6.1: *IMPETUS server specifications.*

Component	Specification
CPU	Intel Xeon E5 quadcore, 3.70 GHz
GPU	Two Nvidia Tesla Keplar K20C, 5 GB GDDR5, with 2496 cores each
RAM	16 GB DDR3 @ 1866 MHz

Table 6.2: *Computer cluster Snurre specifications.*

Component	Specification
CPU	5 computer nodes each with two six-core Intel X5680 @ 3.33-3.6 GHz
GPU	-
RAM	5 computer nodes each with 24GB

6.1 Pinhole Study

Before a complete model of the ballistic test was created in IMPETUS, a pinhole study was conducted to investigate the effects of friction, temperature and strain rate. The numerical model presented in Section 3.3 is also used in this section, and was modified to include friction, with Coulomb friction factors of $\mu = 0, 0.05$ and 0.10.

The material response of aluminium is almost independent of strain rate at room temperature, but for temperatures above 50% of the melting temperature it has shown significant strain rate dependency [55]. During impact, the maximum temperatures observed in the target plate, for the pinhole model, is larger than 80% of the melting temperature, and depend on the impact velocity of the bullet. Figure 6.1 shows the temperature in one of

the pinhole analyses with initial velocity of 700 m/s, and c, m and μ parameters corresponding to the first row in Table 6.3. The maximum temperature is 819 K and is located in the entry of the penetration channel. In the interior of the penetration channel, the temperature is seen to be about 700 K. Therefore the strain rate parameter c and temperature parameter m in the MJC-model were investigated. Values of $c = 0.001, 0.005$ and 0.010 and $m = 0.5, 1.0, 2.0$ and 4.0 were tested. The ballistic limit curves are shown in Figure 6.2.

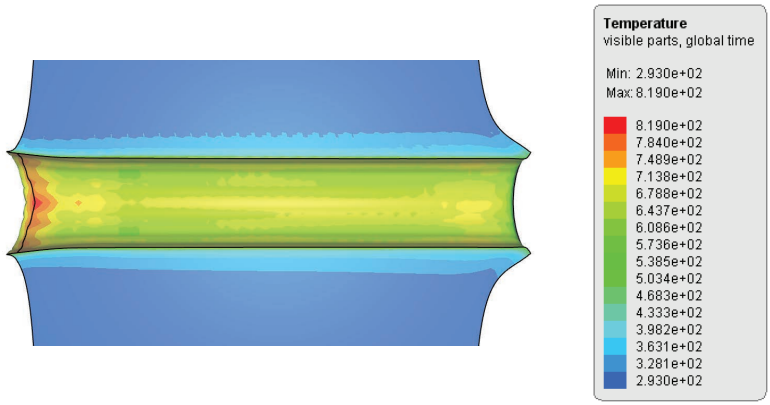

Figure 6.1: *Temperature in the penetration channel, given in Kelvin [K]. v_i = 700 m/s, v_r = 551.1 m/s, $\mu = 0$, $m = 1.0$ and $c = 0.001$.*

Table 6.3 presents the ballistic limit velocities for all tests, which are fitted to the points using the Recht-Ipson model with $a = 1$ and $p = 2$. From Figure 6.2 one can see that the Coulomb friction factor has the most influence on the ballistic limit. There is a 23.9% increase in the ballistic limit between the highest and lowest friction coefficients. A Coulomb friction factor of $\mu = 0.05$ was selected based on a proposed value by Ravid and Bodner [56].

Table 6.3: *Ballistic limit velocities for various combinations of the Coulomb friction factor μ, the temperature parameter m and the strain rate parameter c, for the pinhole study.*

Coulomb friction factor, μ	Temperature parameter, m	Strain rate parameter, c	v_{bl} [m/s]	Rel. Diff.
0	1.0	0.001	429.1	Ref.
0.05	1.0	0.001	494.3	+15.2%
0.10	1.0	0.001	531.8	+23.9%
0	1.0	0.005	443.0	+3.2%
0	1.0	0.010	460.6	+7.3%
0	0.5	0.001	402.8	-6.1%
0	2.0	0.001	437.8	+2.0%
0	4.0	0.001	439.2	+2.4%

The strain rate parameter has a minor influence on the ballistic limit velocity, with a

7.3% increase for the highest strain rate parameter $c = 0.010$. According to Hopperstad and Børvik [44, 50], $c = 0.010$ is too large for this AlMgSi-alloy. Therefore, $c = 0.001$ was chosen based on material data at room temperature. Note that the strain rate parameter might be higher for temperatures close to the melting temperature. The temperature parameter has almost no influence on the ballistic limit for $m \geq 1$. Only 2.4% increase is seen between $m = 1$ and $m = 4$. For $m = 0.5$, a decrease of 6.1% was observed in the ballistic limit. $m = 1$ was selected and is used in the following models. Temperature dependency of these parameters are not tested, and may lead to deviations from the experimental results.

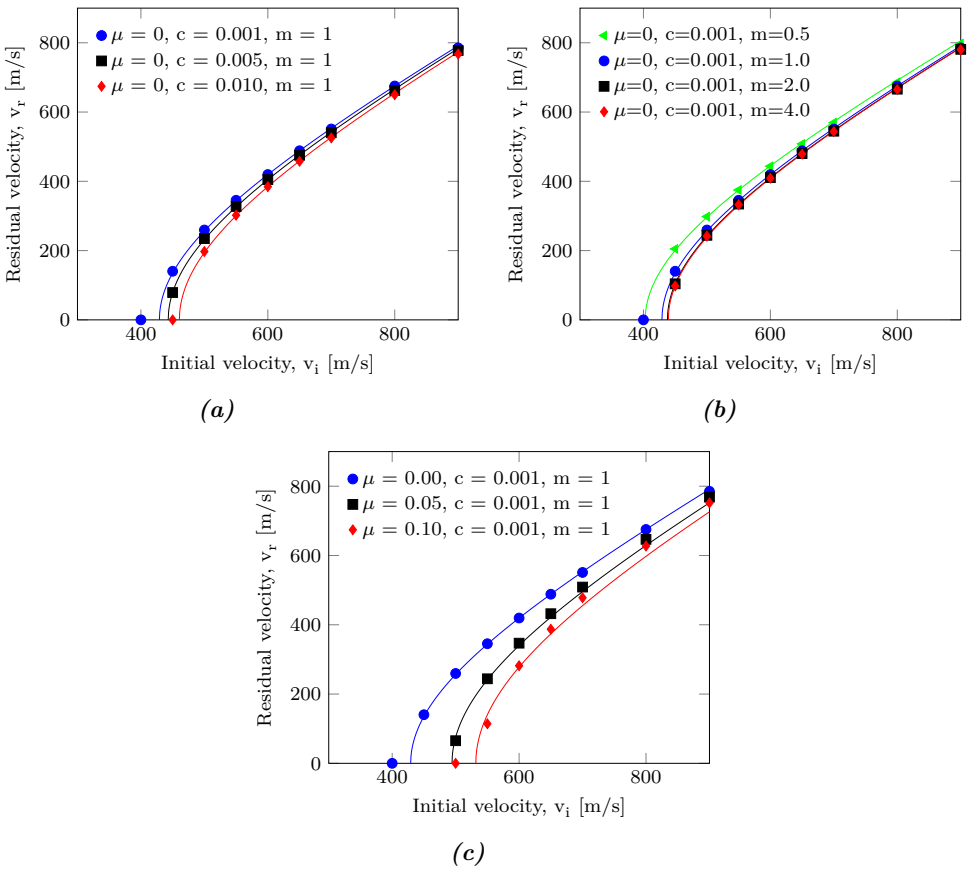

Figure 6.2: *Ballistic limit curves for the pinhole study: (a) Strain rate parameter c is varied, (b) temperature parameter m is varied, (c) Coulomb friction factor μ is varied.*

6.2 Element Erosion Study

In this section the element erosion techniques introduced in Section 2.4.2.1 are studied and discussed. A preliminary numerical model in IMPETUS was established for this purpose only. The Cockcroft-Latham criterion was utilized to compare the techniques, using the two parameters presented in Table 5.4.

6.2.1 Numerical Model

The preliminary numerical model does not include a pinhole, and a failure criterion is therefore needed to perforate the target. As mentioned above, the Cockcroft-Latham criterion was implemented using the `*PROP_DAMAGE_CL` command in IMPETUS. Half of the target was modelled, a symmetry condition was used and the periphery was fixed. The bullet mesh used in the pinhole study is identical to the one presented in Section 3.3.

The target mesh, shown in Figure 6.3, was created in Abaqus and made compatible with IMPETUS using MATLAB. As seen in the figure, the mesh was refined in the impact zone. 60 elements were used over the thickness in a radius of 4 mm from the centre of the impact zone, resulting in an element size of $0.5 \cdot 0.5 \cdot 0.5$ mm^3. Cubic hexahedra were applied in the centre with a radius of 12 mm, while linear hexahedra were used further away from the impact zone.

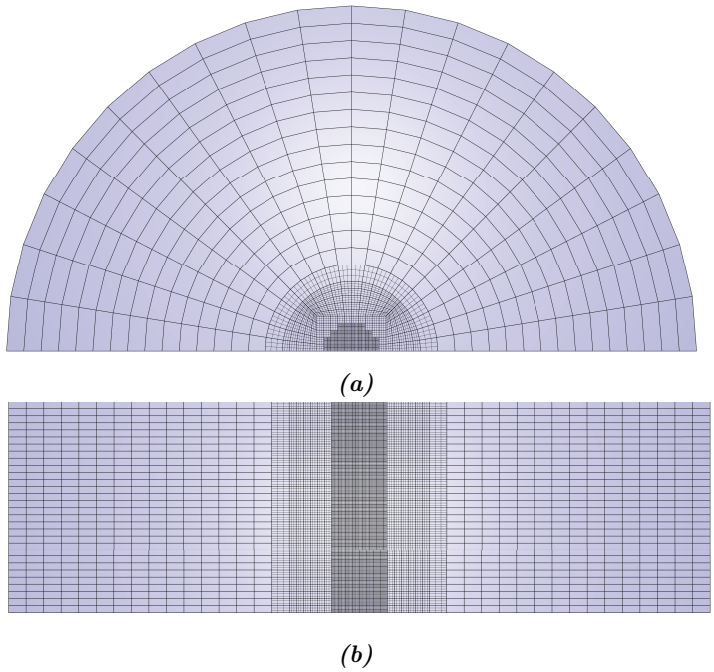

Figure 6.3: *Target mesh: (a) showing target from above and (b) showing the cross-section.*

The contact between the target and bullet was implemented using the new and unverified penalty contact algorithm in IMPETUS, with the keyword `*CONTACT_SUPER`. A penalty factor of 10^{15} was used. The modified Johnson-Cook material model was applied with the material parameters introduced in Sections 3.1 and 6.1. The penetration process is considered extremely fast, and therefore the process is assumed adiabatic and the temperature increase is calculated using a Taylor-Quinney coefficient of $\chi = 0.9$.

6.2.2 Erosion Techniques

The element erosion techniques introduced in Section 2.4.2.1 is repeated below. In this thesis techniques 1, 2 and 3 were studied. Technique 4 is believed to behave similar to technique 3 for an ogival shaped bullet and was therefore omitted.

1. Failed element is not eroded at material failure but loses its deviatoric properties and are still able to take hydrostatic stresses.
2. Failed element is eroded at material failure.
3. Node splitting at failure (crack plane orthogonal to max principal strain).
4. Node splitting at failure (crack plane orthogonal to max principal stress).

The initial velocity of the bullet is 700 $^{m}/_{s}$ for all tests in this study. All ballistic limit velocities are predicted based on this initial velocity and the residual velocities from all tests, using the Recht-Ipson model with $a = 1$ and $p = 2$.

Table 6.4 shows the results using erosion technique 1, the pinhole study and only time step erosion. For the bullet to be able to penetrate the target, some of the elements in front of the bullet have to be removed. Therefore an erosion time step needs to be established for erosion techniques 1 and 3. The erosion time step should be small enough such that the element reaches material failure before it is eroded, but big enough for the GPU/CPU-time to be reasonable.

Analyses with only time step erosion was used to study the effect of the erosion time step. For these analyses no damage rule were applied, and hence all elements were eroded due to dropping time steps. This corresponds to an infinite fracture strain. The predicted ballistic limits are nearly identical for the three erosion time steps studied, and an erosion time step of $3 \cdot 10^{-9}$ seconds is considered sufficient for the element size used in this model.

It was established early in the study that technique 1 is not the best option for this particular target thickness. Since the target is relatively thick, the target thickness being larger than the bullet length, the effect of friction cannot be neglected. Friction forces are applied as shear tractions between the bullet and target.

When an element in the target reaches material failure it loses its deviatoric properties and are unable to withstand the friction forces. This results in non-physical deformation if the erosion time step is too small. Friction no longer has any purpose since the failed elements act as a thin sheet of friction free surface in the penetration channel. Analyses

with erosion technique 1 and smaller erosion time steps were tested. This resulted in non-physical deformation in failed elements and a bad energy balance.

From Table 6.4 one can see that the two different CL parameters yield different predicted ballistic limits using erosion technique 1. These results are as expected.

Table 6.4: *Comparison of erosion technique 1, pinhole study and erosion using only time step.*

Erosion technique	Elements over thickness	Element size [mm]	Δt_{erode} [s]	W_c [MPa]	GPU/CPU-time	v_{bl} [m/s]
Pinhole	30	1.0	0	∞	1h 27min	480.7
1	60	0.5	$3 \cdot 10^{-9}$	364.3	4h 18min	466.2
1	60	0.5	$3 \cdot 10^{-9}$	174.1	4h 10min	448.6
Only time step	60	0.5	$3 \cdot 10^{-9}$	∞	3h 48min	480.9
Only time step	60	0.5	$2 \cdot 10^{-9}$	∞	6h 22min	480.5
Only time step	60	0.5	$1 \cdot 10^{-9}$	∞	14h 8min	478.3*

* Bad energy balance, see Section 6.2.2.1.

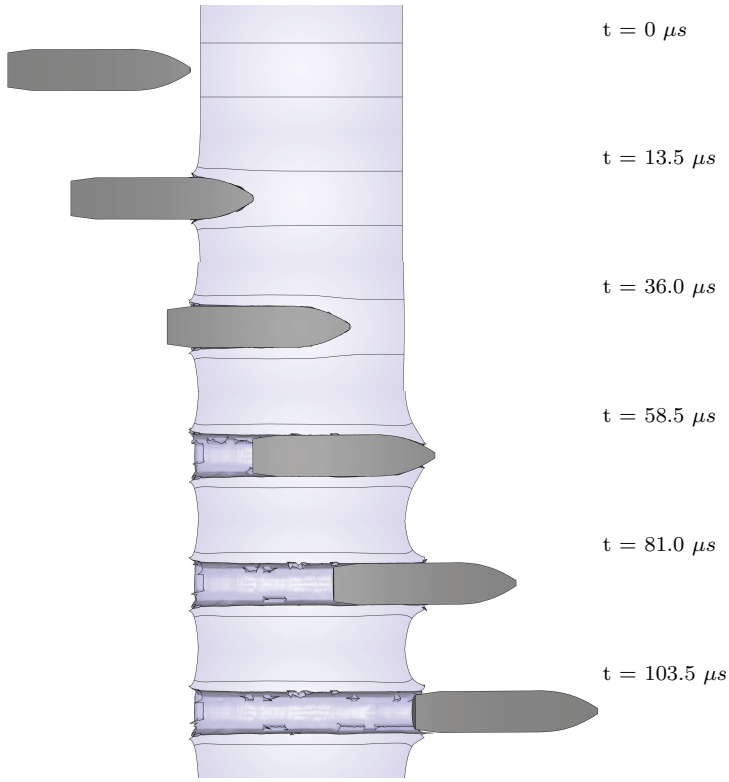

Figure 6.4: *Time-lapse showing the penetration process with erosion technique 1.* $v_i = 700$ $^{m}/_{s}$ *and* $v_r = 537.4$ $^{m}/_{s}$.

Figure 6.4 shows the penetration process for the test in row 3 in Table 6.4, using erosion technique 1. One can see that some of the remaining elements in the penetration channel have sharp pointed edges. This is believed to be because of the above mentioned friction problem. The rest of the penetration channel is relatively smooth.

Table 6.5 summarizes the analyses run with erosion technique 2. Since technique 2 erode elements at material failure, the erosion time step is not needed here and is therefore set to zero. Erosion technique 2 was also tested with two other mesh sizes. Based on the results, technique 2 seems to be more mesh size dependent than techniques 1 and 3. In Figure 6.5, one can see the element boundaries forming a staircase like shape in front of the bullet as it travels through the target. This effect smooths out for decreasing element size.

Table 6.5: *Erosion technique 2.*

Erosion technique	Elements over thickness	Element size [mm]	Δt_{erode} [s]	W_c [MPa]	GPU/CPU-time	v_{bl} [m/s]
2	90	0.33	0	364.3	11h 51min	440.4
2	60	0.50	0	364.3	2h 30min	425.4
2	30	1.00	0	364.3	1h 11min	439.1
2	90	0.33	0	174.1	7h 28min	402.1
2	60	0.50	0	174.1	2h 6min	427.8
2	30	1.00	0	174.1	28min	423.7

Erosion technique 2 also yield different predicted ballistic limits for the two CL parameters, but the limits are lower for technique 2 than technique 1. These lower predicted ballistic limits are probably because of a too coarse mesh. The mesh size dependency will be investigated further in Section 6.3.

Figure 6.5 shows the penetration process for the test in row 5 in Table 6.5. The element boundaries can be seen clearly in the penetration channel and is not as smooth as for erosion technique 1. In the middle of the channel a few elements were eroded even further into the target material. This is probably due to the frictional forces and a too coarse mesh.

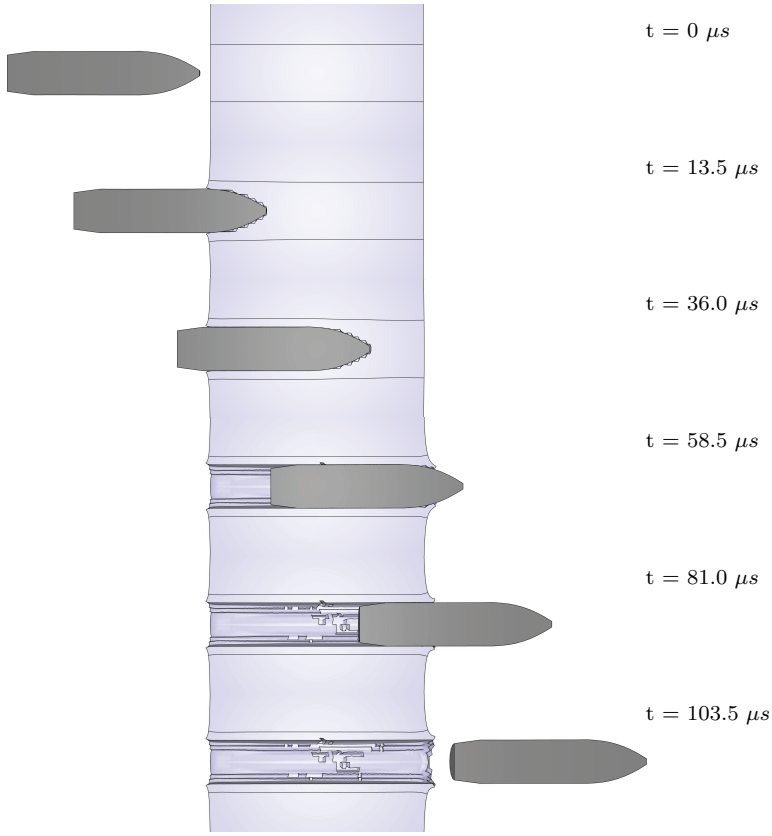

Figure 6.5: *Time-lapse showing the penetration process with erosion technique 2.* $v_i = 700$ m/s *and* $v_r = 554.1$ m/s.

Table 6.6 shows the results from the analyses with erosion technique 3. Also for this technique an erosion time step is needed. The GPU/CPU-time needed to run an analysis without an erosion time step would be too great, if not impossible. Both erosion techniques 1 and 2 can only accumulate damage until the damage parameter is equal to one, but for technique 3 it can become larger. The element boundaries are separated when the damage parameter reaches one, but the element properties are unaffected. This results in nearly no difference between the two CL parameters on the predicted ballistic limits, but a visual difference is seen, as more fragmentation occurs for lower W_c. The GPU/CPU-time is also increased because of more fragmentation.

Erosion technique 3 was tested with a coarser mesh to study the effect of mesh dependency. The increase in mesh size resulted in less fragmentation and larger fragments, but a small difference in the predicted ballistic limit.

The energy balance for tests with erosion time step of $1{\cdot}10^{-9}$ seconds was bad. Holmen [38] proposed to include an erosion criterion based on the geometric strain and geometric strain

Table 6.6: *Erosion technique 3.*

Erosion technique	Elements over thickness	Element size [mm]	Δt_{erode} [s]	ε_{erode}	W_c [MPa]	GPU/CPU-time	v_{bl} [m/s]
3	60	0.5	$3 \cdot 10^{-9}$	10^{20}	364.3	15h 26min	480.7
3	60	0.5	$2 \cdot 10^{-9}$	10^{20}	364.3	22h 24min	478.4
3	60	0.5	$1 \cdot 10^{-9}$	10^{20}	364.3	48h	460.3*
3	30	1.0	$3 \cdot 10^{-9}$	10^{20}	364.3	3h 8min	482.1
3	30	1.0	$2 \cdot 10^{-9}$	10^{20}	364.3	5h 50min	487.0
3	30	1.0	$1 \cdot 10^{-9}$	10^{20}	364.3	16h 55min	484.6*
3	60	0.5	$1 \cdot 10^{-9}$	5	364.3	48h	481.5
3	60	0.5	$1 \cdot 10^{-9}$	5	174.1	72h	475.9

* Bad energy balance, see Section 6.2.2.1.

increment to fix the problem. Including deletion of elements with a greater geometric strain than $\varepsilon_{erode} = 5$ fixed the energy balance. Later it was found that the problems with the energy balance were due to the new and unverified `*CONTACT_SUPER` algorithm in IMPETUS.

The analyses with the `*CONTACT_SUPER` algorithm used much longer GPU/CPU-time than the standard `*CONTACT` algorithm. The tests with an erosion time step of $1 \cdot 10^{-9}$ seconds were rerun using the standard `*CONTACT` algorithm, and a comparison with the corresponding `*CONTACT_SUPER` analyses is presented in Section 6.2.2.1.

In Figure 6.6, the deformation time-lapse of the test in the bottom row of Table 6.6 with erosion technique 3 can be seen. A lot of fragments is seen in the penetration channel, which is not as smooth as for erosion techniques 1 and 2.

A small amount of fragmentation was observed in the experimental tests, and the dominating phenomenon was ductile hole growth. Erosion technique 3 is believed to be better for problems involving thin target plates and brittle materials. Erosion Technique 1 is thought to be the best for ductile materials if frictional forces can be neglected. Erosion technique 2 is assumed to behave better for the target thickness in this thesis, when the mesh size is reduced.

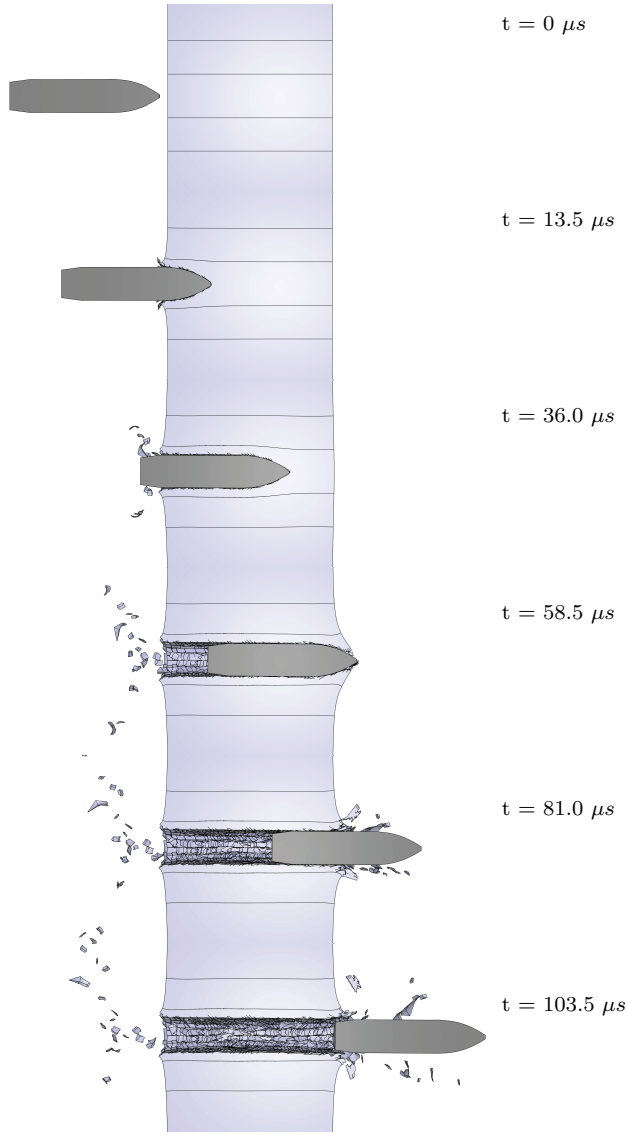

Figure 6.6: *Time-lapse showing the penetration process with erosion technique 3.* $v_i = 700$ $^{m}/_{s}$ *and* $v_r = 513.3$ $^{m}/_{s}$.

In Figure 6.7, the entry and exit holes of the tests presented in Figures 6.4, 6.5 and 6.6 are shown. For erosion technique 1, one can see some elements with sharp edges around the entry and exit holes. These elements have lost their deviatoric properties but not been eroded. For erosion technique 2 one can see that more elements were eroded around both entry and exit holes. Erosion technique 3 yield a lot of fragmentation, and the element boundaries have been separated. One can see this clearly in the entry hole. The exit hole

is not as smooth as for erosion techniques 1 and 2, and crack propagation is seen.

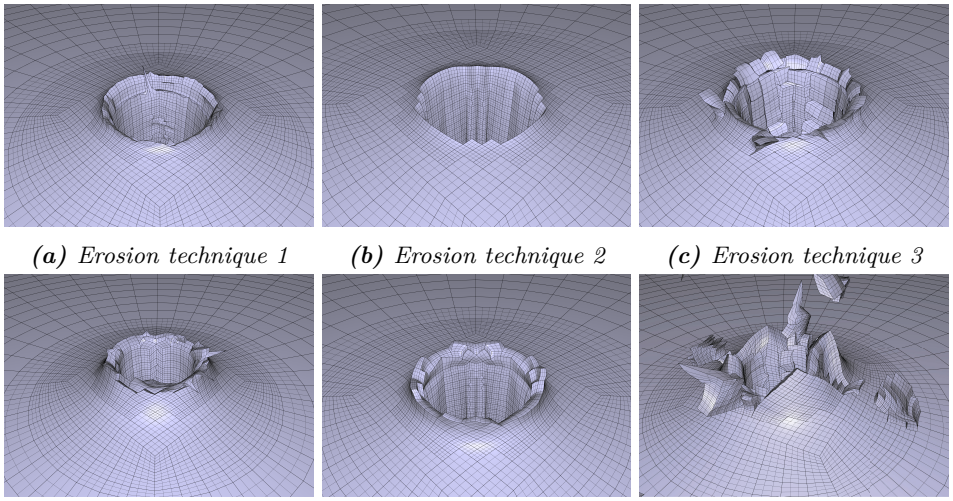

(a) *Erosion technique 1* ***(b)*** *Erosion technique 2* ***(c)*** *Erosion technique 3*

(d) *Erosion technique 1* ***(e)*** *Erosion technique 2* ***(f)*** *Erosion technique 3*

Figure 6.7: *Entry and exit holes with different erosion techniques in IMPETUS; (a), (b) and (c) show the entry holes, (d), (e) and (f) show the exit holes.*

6.2.2.1 Energy Balance

As mentioned earlier the `*CONTACT_SUPER` algorithm caused bad energy balance in the analyses with an erosion time step of $1 \cdot 10^{-9}$ seconds. These were re-tested using the `*CONTACT` algorithm, and a comparison with the results from the `*CONTACT_SUPER` algorithm is presented in Table 6.7. An excellent energy balance is seen for `*CONTACT`. The other analyses run with `*CONTACT_SUPER` is believed to be reasonable and the predicted ballistic limits are within 2 $^{m}/_{s}$ of the `*CONTACT` algorithm.

Table 6.7: *Contact algorithm comparison:* `*CONTACT` *versus* `*CONTACT_SUPER`*.*

Erosion technique	Elements over thickness	Element size [mm]	Contact algorithm	W_c [MPa]	GPU/CPU-time	v_{bl} [m/s]
Only time step	60	0.5	`*CONTACT_SUPER`	∞	14h 8min	478.3
Only time step	60	0.5	`*CONTACT`	∞	8h 23min	485.8
3	60	0.5	`*CONTACT_SUPER`	364.3	48h	460.3
3	60	0.5	`*CONTACT`	364.3	20h 5min	480.4
3	30	1.0	`*CONTACT_SUPER`	364.3	16h 55min	484.6
3	30	1.0	`*CONTACT`	364.3	8h 39min	485.3

From Table 6.7 one can see that the GPU/CPU-time needed to run the analyses with `*CONTACT_SUPER` is almost the double of `*CONTACT`. The predicted ballistic limit for the

bottom tests are almost identical, but for the ones in the middle of Table 6.7 a large difference can be seen.

In Figure 6.8, the energy balance of the middle tests, with erosion technique 3 and 0.5 mm elements, are shown. One can see that the energy balance is not constant with the `*CONTACT_SUPER` algorithm. The "Contact - damping energy" and "Kinetic - energy of free nodes" are also much higher than with the `*CONTACT` algorithm. From this one can conclude that `*CONTACT_SUPER` yields suboptimal results and needs further verification. All further analyses will therefore be run with the standard `*CONTACT` algorithm.

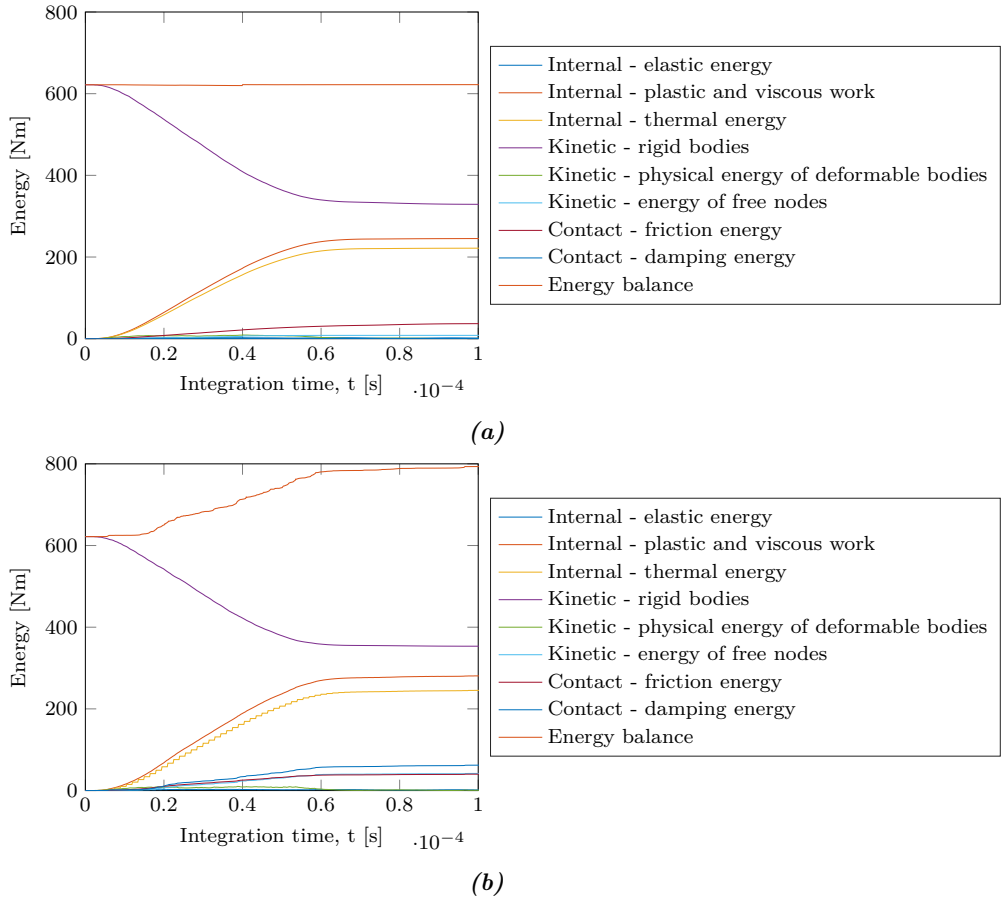

Figure 6.8: *Energy balance: (a) with the `*CONTACT` algorithm, (b) with the `*CONTACT_SUPER` algorithm.*

6.3 Mesh Sensitivity Study

The cubic hexahedral elements in IMPETUS, using erosion technique 2, are compared to linear elements in Abaqus. To reduce the GPU/CPU-time needed to run an analysis a new numerical model was established, modelling only a five degree slice of the bullet and target.

6.3.1 Numerical Model

The numerical model in IMPETUS was modelled in a similar fashion as in Section 6.2.1, where the half model was exchanged with a five-degree model, and a symmetry plane was added. A penalty factor of 10^{15} was used for the standard penalty `*CONTACT` algorithm. The IMPETUS mesh, created in Abaqus, with 150 elements over the thickness is presented in Figure 6.9.

An element size of $0.2 \cdot 0.2 \cdot (\pi r/36)$ mm^3 was used in the inner part of the target with a radius of 10 mm, i.e., 150 elements over the thickness and one in the circumferential direction. A coarser mesh was used farther from the impact zone, and in the centre of the target, cubic elements were used in a radius of 16 mm. The bullet was modelled as a rigid part and the mesh is shown in Figure 6.10.

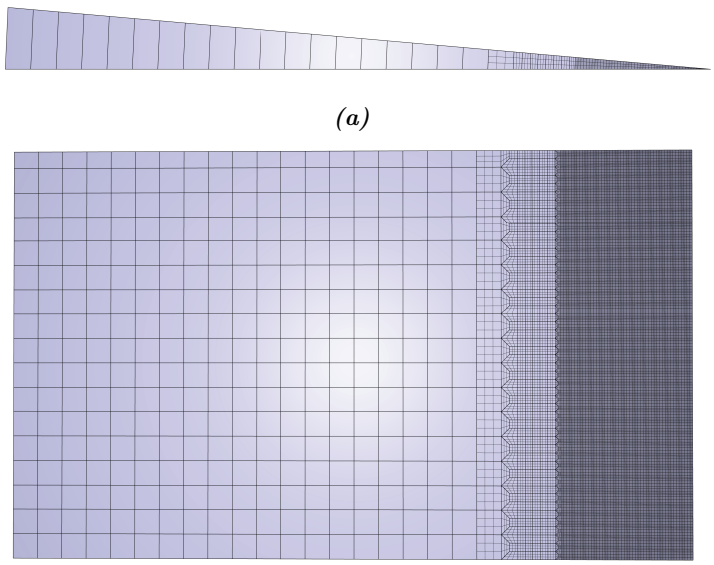

Figure 6.9: *Target mesh in IMPETUS using cubic hexahedrons in the impact area: (a) showing target from above and (b) showing the cross-section.*

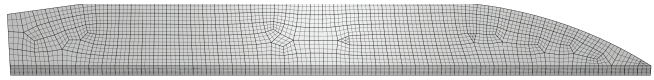

Figure 6.10: *Bullet mesh.*

In Abaqus, the numerical model was made to resemble the IMPETUS model as precisely as possible. The SIMLab Metal Model was used to be able to apply a CL damage criterion, adiabatic heating and a rate dependent MJC material model. To get the bullet to penetrate in Abaqus, a supplementary failure criterion was established. In addition to the CL criterion, an element was deleted if the temperature in the element was higher than 90% of the melting temperature, i.e., $T_c = 804$ K.

A general contact algorithm was used with a Coulomb friction factor of 0.05, as in the IMPETUS model. The bullet was modelled as an analytical rigid surface, and unlike the rigid IMPETUS bullet, the analytical rigid surface has no mesh. Abaqus/Explicit offers only first order linear elements, and these have been used with reduced integration in the target mesh shown in Figure 6.11. The figure shows the Abaqus mesh with 150 elements over the thickness. A three-dimensional picture of the five-degree model in Abaqus is shown in Figure 6.12.

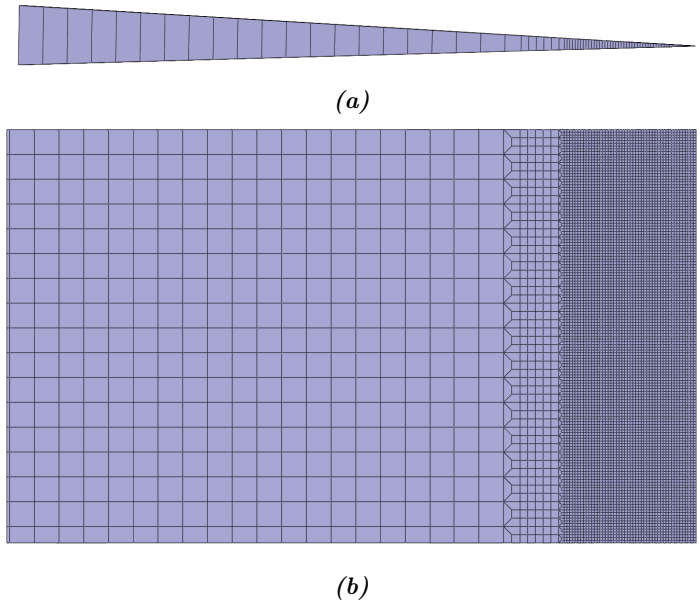

Figure 6.11: *Target mesh in Abaqus using linear hexahedrons in the impact area: (a) showing target from above and (b) showing the cross-section.*

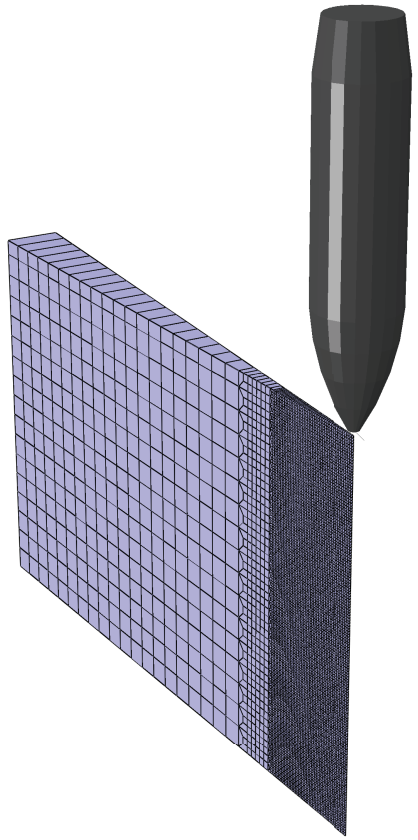

Figure 6.12: *Five-degree model in 3D from Abaqus.*

6.3.2 Results

The results from the mesh sensitivity study are presented in Tables 6.8 and 6.9, and plotted in Figure 6.13 for better visualization. An initial velocity of 700 $^{m}/_{s}$ was used for all tests. The ballistic limit velocities are predicted based on this initial velocity and the residual velocities using the Recht-Ipson model with $a = 1$ and $p = 2$.

Table 6.8 shows the results for the IMPETUS model. The model was run with the two different CL parameters to compare the convergence, and to see if there was any difference in the predicted ballistic limits for the two. For the IMPETUS model, a clear difference is seen between the two CL parameters, but the same is not seen for the Abaqus model, presented in Table 6.9.

One reason for the small difference between the two CL parameters in Abaqus may be due to the temperature erosion criterion. Without this criterion the analyses crash due to excessively distorted elements. The same tendency can be seen in IMPETUS with linear elements. Linear elements were tested in IMPETUS, but this resulted in elements being eroded because of negative volume due to the S/R integration in IMPETUS [37].

Table 6.8: *Mesh sensitivity results from IMPETUS analyses.*

Elements over thickness	Element size [mm]	W_c [MPa]	GPU/CPU-time	v_{bl} [m/s]	Rel. Diff.
Experiment	-	-	-	517.5	Ref.
30	1.000	364.3	11min	436.8	-15.6%
60	0.500	364.3	38min	407.9	-21.2%
90	0.333	364.3	1h 51min	420.7	-18.7%
150	0.200	364.3	4h 14min	437.4	-15.5%
300	0.100	364.3	40h 37min	451,0	-12.9%
405	0.075	364.3	5days	454.3	-12.2%
30	1.000	174.1	8min	368.2	-28.9%
60	0.500	174.1	31min	364.0	-29.7%
90	0.333	174.1	1h 29min	366.1	-29.3%
150	0.200	174.1	3h 27min	391.6	-24.3%
300	0.100	174.1	10h 45min	412.3	-20.3%
405	0.075	174.1	35h 51min	424.6	-17.9%

The three mesh sizes studied in Table 6.5 in Section 6.2.2, with erosion technique 2 are here retested with the new numerical model in IMPETUS. The predicted ballistic limits are lower for the five-degree model than for the half model. The reason for this is probably that the five-degree model resembles a 2D axisymmetric model more than a 3D model. According to Børvik [44], a 2D model often needs a finer mesh than a 3D model to obtain convergence.

Table 6.9 presents the data from the Abaqus analyses. Note that the Abaqus model uses linear elements versus cubic elements in IMPETUS. The node spacing is therefore three times as high in Abaqus for the same element size. One analysis with 1200 elements over the thickness was tested in Abaqus to give approximately the same node spacing as for the finest mesh in IMPETUS. The analysis used 10 days on the supercomputer Vilje, and based on this analysis it is believed that the Abaqus mesh has converged.

Table 6.9: *Mesh sensitivity results from Abaqus analyses.*

Elements over thickness	Element size [mm]	W_c [MPa]	CPU-time	v_{bl} [m/s]	Rel. Diff.
Experiment	-	-	-	517.5	Ref.
30	1.000	364.3	1min	504.0	-2.6%
60	0.500	364.3	2min	479.2	-7.4%
90	0.333	364.3	6min	474.9	-8.2%
150	0.200	364.3	1h 35min	492.0	-4.9%
300	0.100	364.3	8h 57min	478.5	-7.5%
405	0.075	364.3	16h 38min	477.6	-7.7%
1200	0.025	364.3	10days*	478.2	-7.6%
30	1.000	174.1	1min	493.4	-4.6%
60	0.500	174.1	2min	477.8	-7.7%
90	0.333	174.1	4min	473.3	-8.5%
150	0.200	174.1	1h 20min	488.3	-5.6%
300	0.100	174.1	8h 24min	477.1	-7.8%
405	0.075	174.1	13h 5min	475.7	-8.1%

* The analysis was run on the supercomputer Vilje at NTNU.

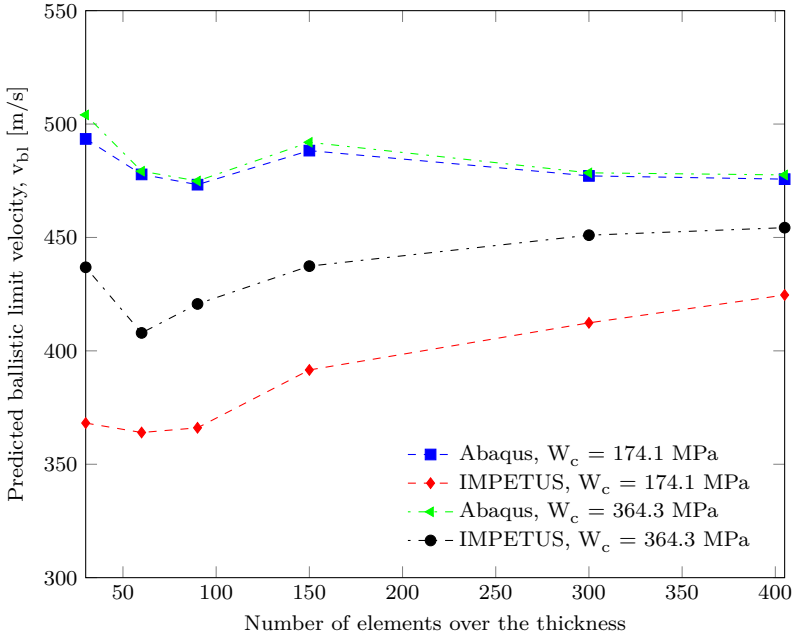

Figure 6.13: *Mesh sensitivity study showing the data in Tables 6.8 and 6.9, comparing IMPETUS and Abaqus analyses with different CL parameters.*

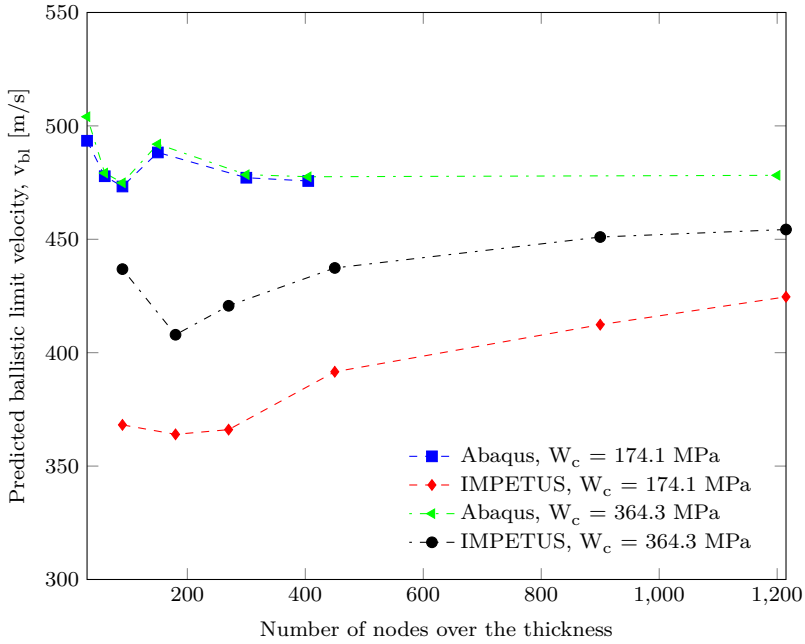

Figure 6.14: *Mesh sensitivity study showing the data in Tables 6.8 and 6.9 with the number of nodes over the target thickness.*

Figures 6.13 and 6.14 presents the results obtained from the sensitivity study. The mentioned difference in CL parameter is visualized, and IMPETUS is compared to Abaqus. In these figures, one can clearly see that IMPETUS and Abaqus converge towards a ballistic limit from different sides; IMPETUS converges from below and Abaqus converges from above. Based on the trend of the curves it is not possible to determine whether they converge towards the same value or not. Investigation of the curves in Figure 6.14 reveals that Abaqus converges faster than IMPETUS for the same node spacing.

There are several possible reasons for this. One cause may be the use of cubic elements and exact integration in IMPETUS, versus linear elements with reduced integration in Abaqus. IMPETUS erodes an element when 16 out of 64 integration points reach material failure, while an element in Abaqus only has one integration point. The temperature erosion criterion in Abaqus, which is not needed in IMPETUS, may be another factor.

From Figure 6.13, it can be seen that although the element size is 75 μm, close to the 65μm grain size of the AlMgSi-alloy seen in Section 3.6, the FE solution has not yet converged.

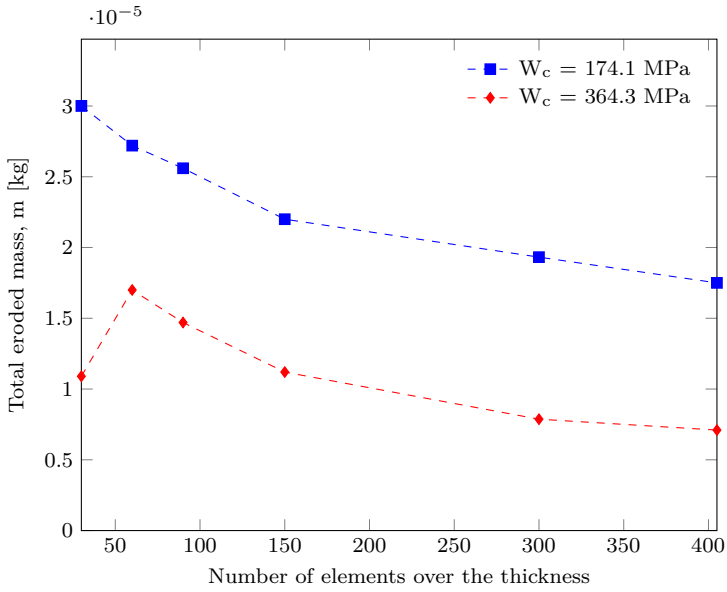

Figure 6.15: *Total eroded target mass in IMPETUS.*

For the IMPETUS model, the eroded mass versus number of elements over the thickness is plotted in Figure 6.15. One can see that the eroded mass converges towards a finite value, and has the same trend as the ballistic limit in Figure 6.13. For the coarser mesh, too much mass is eroded and there is no longer contact between the bullet and target surface, seen in Figure 6.16(a). The finer mesh in Figure 6.16(b) does not have this problem.

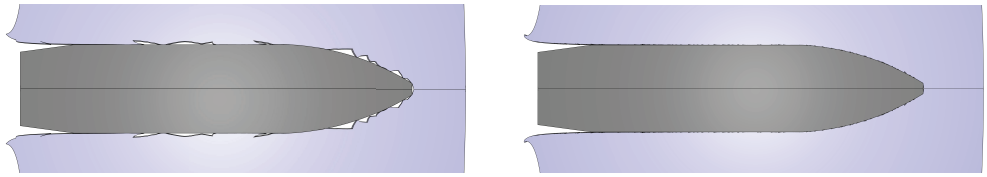

(a) ***(b)***

Figure 6.16: *Comparison of the penetration process for different mesh sizes: (a) element size 0.5 mm and (b) element size 0.075 mm.*

The penetration channel for the Abaqus model is smooth for both mesh sizes and does not seem to be as mesh sensitive as the IMPETUS model. To erode an element when 16 out of 64 integration points reach material failure, may not be sufficient. Some of the mesh size dependency seen for the IMPETUS model might change if the number of integration points needed to erode an element is increased.

(a) Entry *(b) Path* *(c) Exit*

Figure 6.17: *Penetration channel magnification in IMPETUS.*

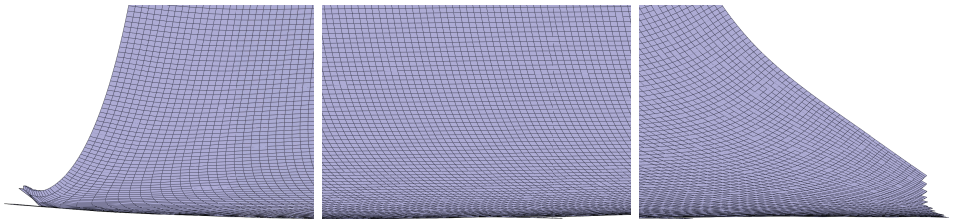

(a) Entry *(b) Path* *(c) Exit*

Figure 6.18: *Penetration channel magnification in Abaqus.*

Figures 6.17 and 6.18 illustrate the deformation of three important locations after perforation. The element size shown is 0.075 mm, both for the IMPETUS and Abaqus model. The figures resemble those in Figure 3.27 in Section 3.6, especially for the IMPETUS model. The cubic elements in IMPETUS is superior to the linear elements in Abaqus when it comes to the deformation in the entry of the penetration channel.

6.4 Discussion

In this chapter, we have studied the effects of the MJC parameters, friction coefficient, erosion techniques and mesh size. These parameters were studied to be able to model the experimental tests as accurately and realistically as possible.

Although aluminium is more strain rate dependent for temperatures close to the melting temperature, this was not tested for the AlMgSi-alloy, and a value for the strain rate parameter c was selected based on data available at room temperature. This may lead to some deviation from the experimental tests, but the effect of the strain rate parameter was minor and an increase by a factor 10 resulted in a 7.3% increase in the ballistic limit.

It is believed that erosion technique 2 is the one best suited for this particular target thickness. This technique predicted a different ballistic limit for the two different CL parameters tested, and is suitable for testing different failure criteria. Technique 2 also

allowed for friction to be used in the analyses. The energy balance problems encountered in the early tests proved to be due to the new and unverified `*CONTACT_SUPER` algorithm in IMPETUS, and the standard `*CONTACT` algorithm was used in later analyses.

The mesh size sensitivity study concluded that the solution had not yet converged for the IMPETUS model, but due to limitations in computing capacity, an element size smaller than 0.075 mm was not possible. The IMPETUS analyses were compared to Abaqus analyses, and they were seen to converge from different sides. Greater mesh sensitivity was seen for the IMPETUS analyses, and the number of integration points needed to reach material failure before element erosion was discussed as a probable cause. It was not possible to change the number of integration points needed for erosion in IMPETUS, and as a results, this effect was not possible to investigate further.

7 Numerical Analyses of Ballistic Impacts

In this chapter the numerical ballistic impact results are presented. Three different damage evolution models, calibrated in Chapter 5, are used, and the results compared to the experimental results.

7.1 Numerical Model

The numerical models used in this chapter are based on the result of the preliminary numerical study in Chapter 6. All analyses were run using the five-degree model presented in Section 6.3.1. Erosion technique 2 and the MJC parameters selected in Section 6.1, were used for the IMPETUS model. The SIMLab Metal Model was used to describe the material behaviour for the Abaqus model with the Cockcroft-Latham fracture criterion. For the Gurson analyses, the GTN model in Abaqus was tested. A material subroutine by Dæhli [51] was used to add adiabatic heating effects, and was later modified to include the shear softening term in the GTN model, introduced in Section 2.2.7.2.

A mesh with element size of 0.2 mm was selected for both models based on GPU/CPU-times presented in Tables 6.8 and 6.9. The GPU/CPU-times were based on an initial velocity of 700 $^{m}/_{s}$ and an integration time of $1.5 \cdot 10^{-4}$ seconds. For lower initial velocities the GPU/CPU-times will be greater due to longer integration times. The mesh is the same as presented in Figures 6.9 and 6.11 in Section 6.3.1.

The analyses were run with initial velocities in the range 450 - 900 $^{m}/_{s}$, and the ballistic limits were fitted using a non-linear least-square method. The values for a and p in the Recht-Ipson model were fitted with the ballistic limits from the analyses.

7.1.1 Rigid Steel Core vs. Johnson-Cook Steel Core

A small study was conducted to quantify the importance of a Johnson-Cook steel core versus a rigid steel core for the bullet. The material properties of the steel core was adopted from Børvik [57], and are presented in Table 7.1.

Table 7.1: *Johnson-Cook steel core material properties, adopted from Børvik [57].*

E [MPa]	ν	ρ [kg/m^3]	C_p [J/(kg K)]	σ_0 [MPa]	B [MPa]	n	$\dot{p}_0$ [1/s]	c	T_r [K]	T_m [K]	m
210 000	0.33	7850	452	1200	50 000	1.0	$5 \cdot 10^{-4}$	0	293	1800	1.0

Analyses with an initial velocity of 700 m/s and a CL parameter of $W_c = 364.3$ MPa were conducted. The simulation using a JC steel core resulted in a residual velocity of $v_r = 542.4$ m/s, while the analysis with a rigid steel core had a residual velocity of $v_r = 546.6$ m/s. The difference in residual velocities for the two cases were only 0.8%, and hence the effect was negligible. The computational time needed for one analysis with the JC steel core was 11 hours and 53 minutes, and with the rigid steel core it was 3 hours and 59 minutes. The computational time with the JC steel core was almost three times as long.

The experiments showed that the bullet was nearly unaffected by the impact, and therefore it was assumed that the deformation of the bullet could be neglected. Based on this, it was considered a reasonable assumption to model the bullet as a rigid part, which was done in both IMPETUS and Abaqus.

7.2 Impact with the Cockcroft-Latham Model

In this section the results from the impact analyses with the Cockcroft-Latham model are presented. The two parameters calibrated in Section 5.1 were used and compared for both the IMPETUS and Abaqus analyses. The keyword `*PROP_DAMAGE_CL` was used in IMPETUS to add the CL criterion, while the SIMLab Metal Model was used in Abaqus.

7.2.1 Impacts Analysed in IMPETUS

Table 7.2 presents the Recht-Ipson parameters and the ballistic limit velocities for the analyses run with the Cockcroft-Latham criterion in IMPETUS. The ballistic limits are compared to the experimental results, and the relative difference is given. The CL parameter calibrated from the computational cells yields the best result compared with the experiments, with a 9.7% lower ballistic limit. As observed, the difference in CL parameters yields a large difference in ballistic limit velocities.

Note that the mesh selected has not converged, and both the differences between the two analyses and the deviation from the experimental results are considered too large. The differences in ballistic limit velocity for the selected mesh and the finest mesh presented in Section 6.3 were 6.4% and 3.3% for the lower and higher CL parameters, respectively. Hence, the analyses with the lower CL parameter is more mesh sensitive.

Table 7.2: *Recht-Ipson parameters for analyses with the Cockcroft-Latham fracture criterion in IMPETUS.*

W_c [MPa]	a	p	v_{bl} [m/s]	Rel. Diff.
Experiment	0.9851	2.1072	517.5	Ref.
174.1	0.9248	2.4825	384.4	-25.7%
364.3	0.9424	2.4882	467.2	-9.7%

Figure 7.1 shows the ballistic limit curves fitted to the points from the analyses with different CL parameters. The experimental results are shown for comparison. The ballistic limits with the CL fracture criterion are observed to be conservative to the experimental results.

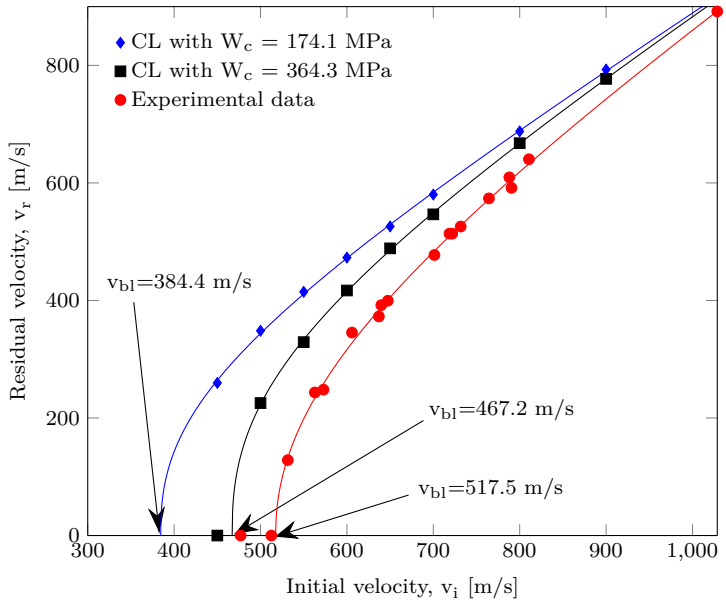

Figure 7.1: *Ballistic limit curves with two different CL parameters in IMPETUS.*

Figure 7.2 shows the penetration process in IMPETUS with the two different CL parameters for an initial velocity of 700 m/s. The dominating fracture mechanism for the deformation process is observed to be ductile hole growth, with some petalling in the exit area. An overall small difference is seen in the deformation. The largest difference is observed near the exit region, where the deformation is smaller for the lower CL parameter. The reason for this is probably that more mass is eroded for the analyses with lower CL parameter, as shown in Figure 6.15 in Section 6.3.

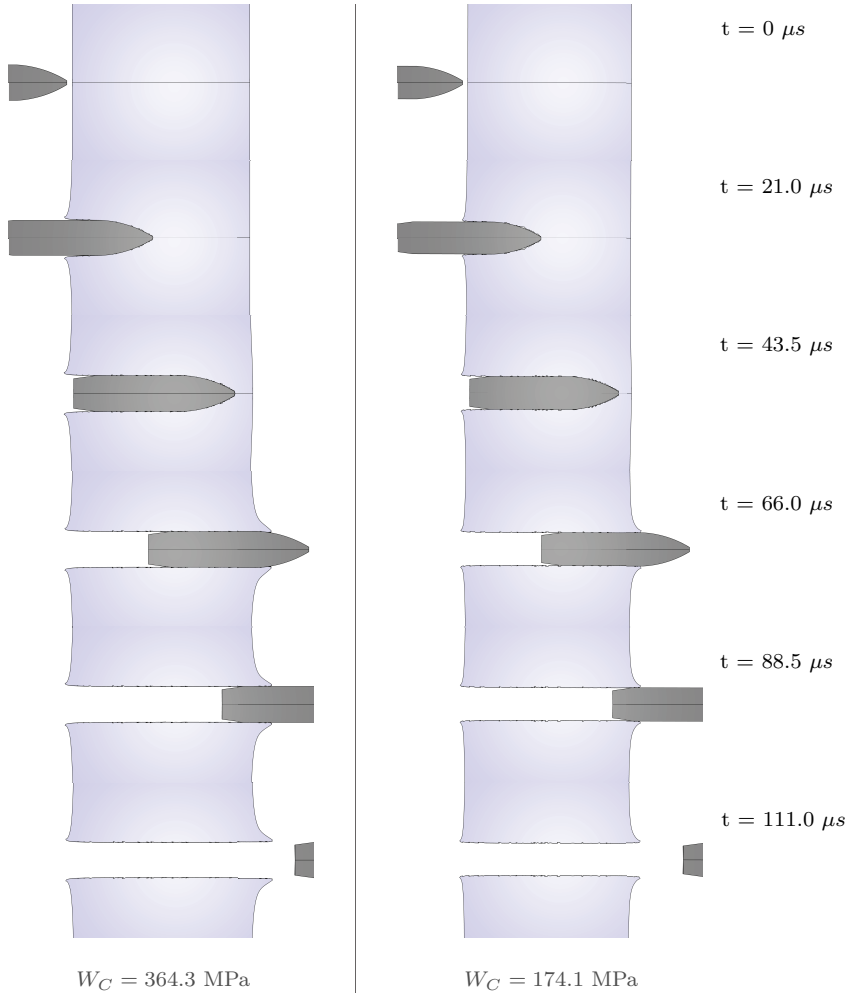

Figure 7.2: *Time-lapse illustrating the penetration process with two different CL parameters in IMPETUS for* $v_i = 700$ m/s. $W_c = 364.3$ *MPa yields* $v_r = 546.6$ m/s, *and* $W_c = 174.1$ *MPa yields* $v_r = 580.2$ m/s.

7.2.2 Impacts Analysed in Abaqus

Table 7.3 presents the Recht-Ipson parameters and the ballistic limits for the analyses with the Cockcroft-Latham criterion performed in Abaqus. The analysis with the higher CL parameter is the one closest to the experimental results, with a relative difference of only 4.3%. A minimal difference is observed between the different CL parameters, in contrast to the IMPETUS results.

The reason for the negligible difference in ballistic limit between the two CL parameters is

probably the temperature erosion criterion needed in the Abaqus analyses. The SIMLab Metal Model does not allow one to check if the elements were eroded on temperature or the CL criterion. Therefore, the amount of elements eroded on the temperature criterion is uncertain.

Table 7.3: *Recht-Ipson parameters with the Cockcroft-Latham fracture criterion in Abaqus.*

W_c [MPa]	a	p	v_{bl} [m/s]	Rel. Diff.
Experiment	0.9851	2.1072	517.5	Ref.
174.1	0.9943	2.0450	491.4	-5.0%
364.3	0.9990	2.0247	495.0	-4.3%

Figure 7.3 shows the ballistic limit curves from the Abaqus analyses with the Cockcroft-Latham criterion. One can see the minimal difference between the two CL parameters, and the Abaqus results are observed to be conservative to the experimental results.

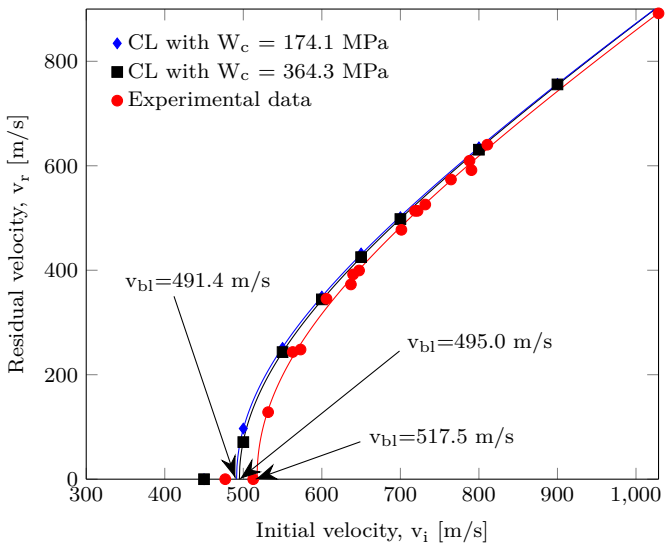

Figure 7.3: *Ballistic limit curves with two different CL parameters in Abaqus.*

The penetration process for the two CL parameters in Abaqus is shown in Figure 7.4, and the same phenomenon can be seen as for the IMPETUS analyses regarding presence of petalling in the exit region. Slightly smaller deformation is observed around the exit region for the lower CL parameter analysis, and the edge is not as sharp. Around the entry region, no difference is seen for the Abaqus analyses, unlike the IMPETUS analyses where the lower CL parameter showed less deformation.

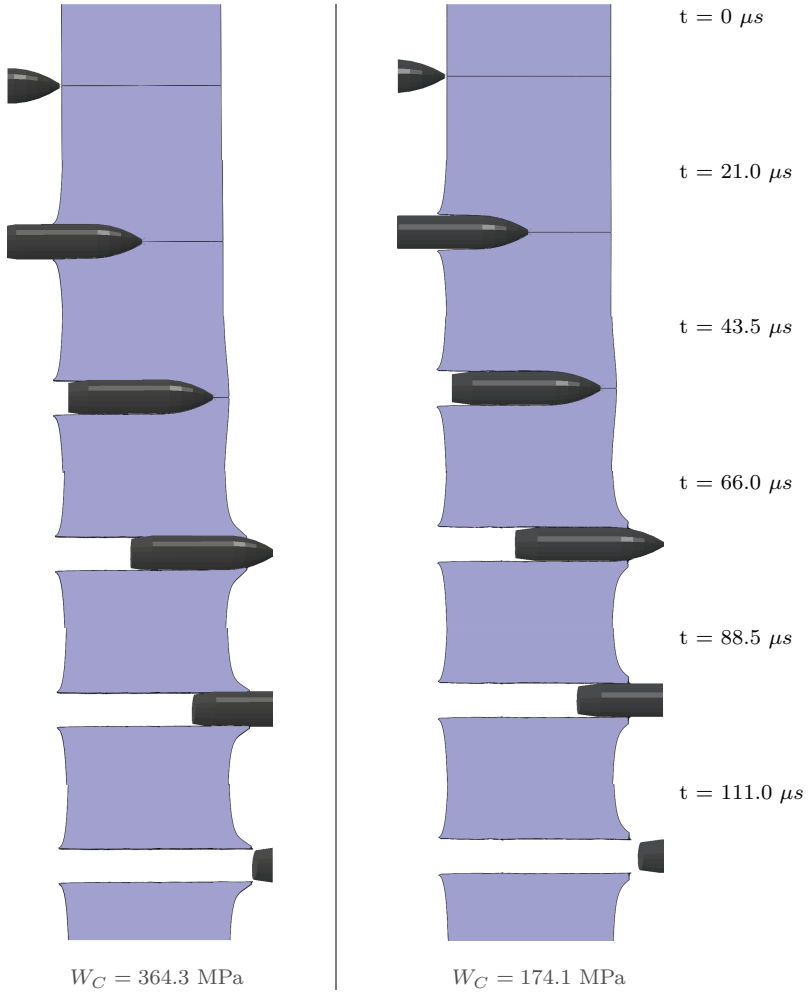

Figure 7.4: *Time-lapse illustrating the penetration process with two different CL parameters in Abaqus for* $v_i = 700$ m/s. $W_c = 364.3$ *MPa yields* $v_r = 498.0$ m/s, *and* $W_c = 174.1$ *MPa yields* $v_r = 501.6$ m/s.

7.3 Impact with the Johnson-Cook Model

Impact analyses with the Johnson-Cook fracture model are presented in this section. Parameters calibrated in Chapter 5 were used in IMPETUS, and compared with the experimental results. The JC fracture model in IMPETUS does not include the last term in Equation 2.35 in Section 2.2.6.2, and the influence of the Lode parameter on the fracture surface could therefore not be investigated. The keyword `*PROP_DAMAGE_JC` was used to add the JC fracture model in IMPETUS.

The SIMLab Metal Model does not have the JC fracture model implemented, thus the built-in JC model in Abaqus was tested, but the bullet was unable to perforate the target without the temperature erosion criterion. Therefore, the JC model was only investigated using IMPETUS.

7.3.1 Impacts Analysed in IMPETUS

The Recht-Ipson parameters, as well as the ballistic limits from the CL and JC fracture models in IMPETUS, are presented in Table 7.4. A notable difference is seen between the two fracture models, although they are calibrated to the same computational cell data.

Table 7.4: *Recht-Ipson parameters with the Cockcroft-Latham and Johnson-Cook fracture models in IMPETUS.*

Fracture model	a	p	v_{bl} [m/s]	Rel. Diff.
Experiment	0.9851	2.1072	517.5	Ref.
CL with $W_c = 174.1$ MPa	0.9248	2.4825	384.4	-25.7%
CL with $W_c = 364.3$ MPa	0.9424	2.4882	467.2	-9.7%
JC	0.9482	2.2175	419.2	-19.0%

The ballistic limit curve for the JC fracture model is shown in Figure 7.5, and the result is seen to be conservative, as for the two CL parameters. This is preferable when designing and dimensioning protective structures. Figure 7.6 shows the ballistic limit curves for the IMPETUS analyses with both the JC and CL fracture criteria presented in Table 7.4.

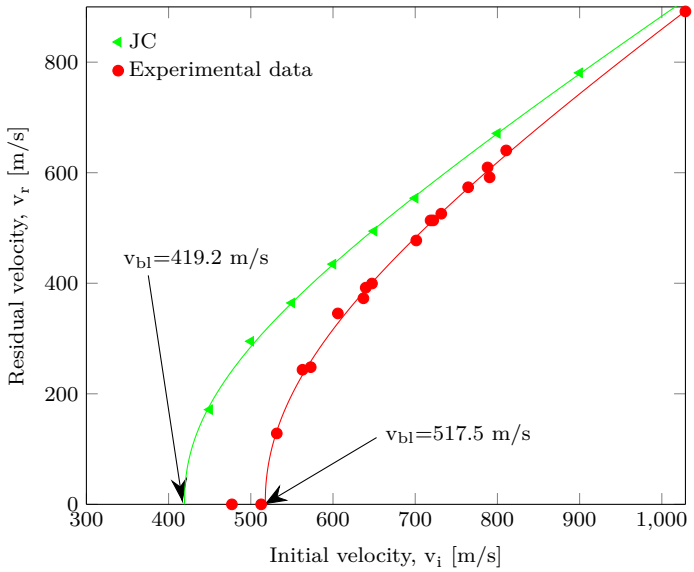

Figure 7.5: *Ballistic limit curve with the JC fracture model in IMPETUS.*

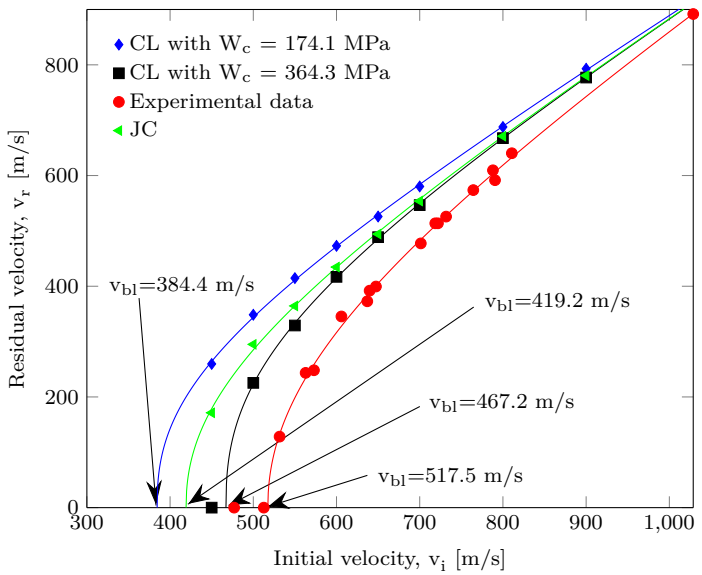

Figure 7.6: *Ballistic limit curves with the CL and JC fracture models in IMPETUS.*

The penetration process for an analysis with the JC fracture model is shown in Figure 7.7. Investigation of the perforation reveals a similar deformation pattern to the one with the higher CL parameter, presented in Figure 7.2. The difference in residual velocity for

these two analyses is only 7.3 m/s for an initial velocity of 700 m/s. No noticeable difference is seen in the deformation pattern.

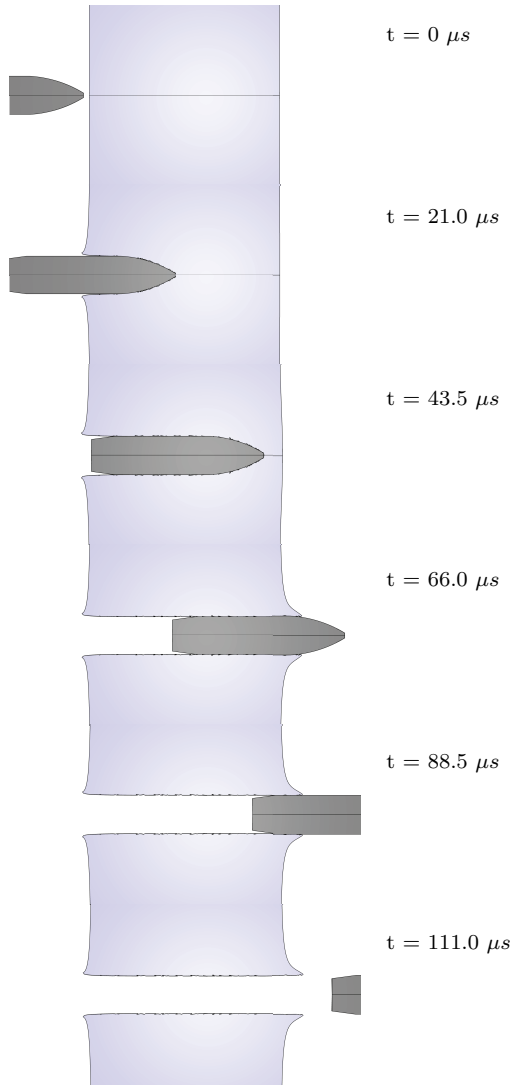

Figure 7.7: *Time-lapse illustrating the penetration process with the JC fracture model in IMPETUS for $v_i = 700$ m/s, yielding a residual velocity $v_r = 553.9$ m/s.*

A considerable difference is seen in the ballistic limit curves for the JC and CL fracture criteria calibrated to the computational cells, cf. Figure 7.6 , in contrast to the results presented in Section 5.3 regarding the tensile test comparison. Therefore an element in the exit region of the target plate was selected, and is shown in Figure 7.8, to compare the

response from the different fracture criteria. The maximum accumulated plastic strain in the element is plotted in Figure 7.9.

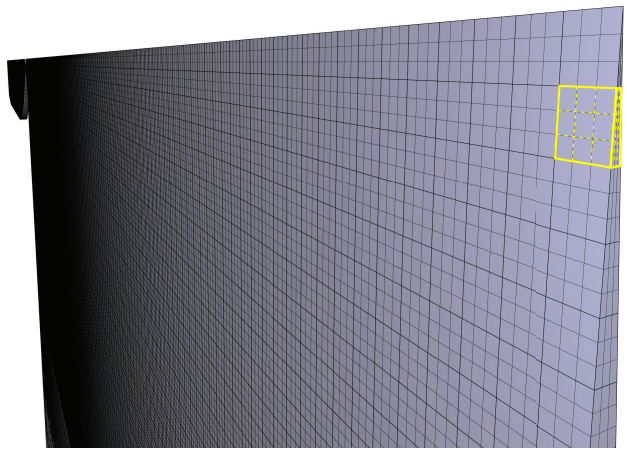

Figure 7.8: *Selected element used to compare the accumulated plastic strain for the Cockcroft-Latham and the Johnson-Cook fracture criteria in IMPETUS.*

The element is eroded in the penetration process, and one can see in Figure 7.9 that the plastic strain at failure is considerable lower for the JC criterion than for the CL criterion with the higher parameter. An initial velocity of 700 m/s was chosen for this investigation. Note that a similar difference is seen for all initial velocities.

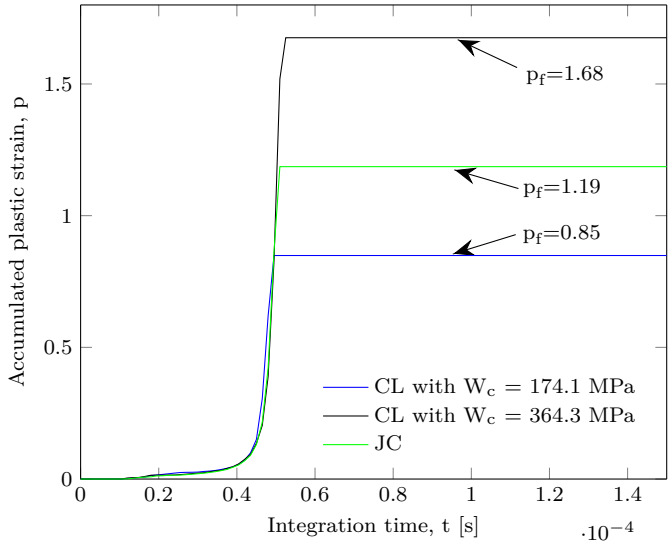

Figure 7.9: *Accumulated plastic strain in the selected element comparing the Cockcroft-Latham and the Johnson-Cook fracture criteria in IMPETUS.*

7.4 Impacts with the Gurson Model

In this section the ballistic impact response with the Gurson-Tvergaard-Needleman model is presented. The Gurson parameters calibrated in Sections 5.4.1 and 5.4.2 were used, and the analyses run using Abaqus. A temperature erosion criterion was needed to perforate the target. A user-subroutine adopted from Dæhli [51] was used to include adiabatic heating, and was later modified to add the shear softening term in the GTN model. As the GTN model is not available in IMPETUS, only Abaqus have been used for the analyses in this section.

7.4.1 The GTN Model in Abaqus

The built-in GTN model in Abaqus was tested with the calibrated parameters of $q_1 = 1.16$ and $q_2 = 1.00$. Figure 7.10 shows a contour plot of the void volume fraction for the last converged state. The compressive forces in front of the bullet makes the initial voids in the target close. Naturally, this results in no void growth, and hence ductile fracture cannot occur. When the voids close and the void volume fraction becomes zero, the GTN yield surface develops into a von Mises yield surface, and the bullet is unable to perforate the target.

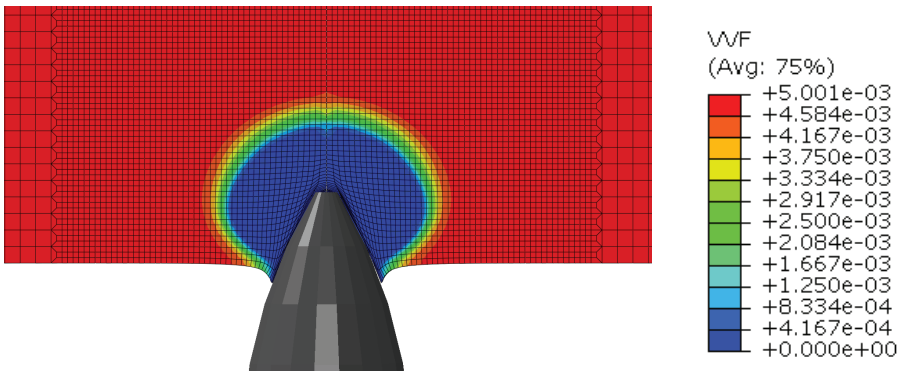

Figure 7.10: *Penetration with the GTN model in Abaqus, presented as a void volume fraction contour plot. The compressive forces in front of the bullet closes the initial voids.*

7.4.2 The GTN Model with Adiabatic Heating

To see if the bullet was able to penetrate with the temperature erosion criterion, the user-subroutine with the GTN model and adiabatic heating was tested. This was also done to see if the later stages of the penetration process would yield void growth or not, since the exit area showed a tendency of petalling in previous analyses and in the experiment.

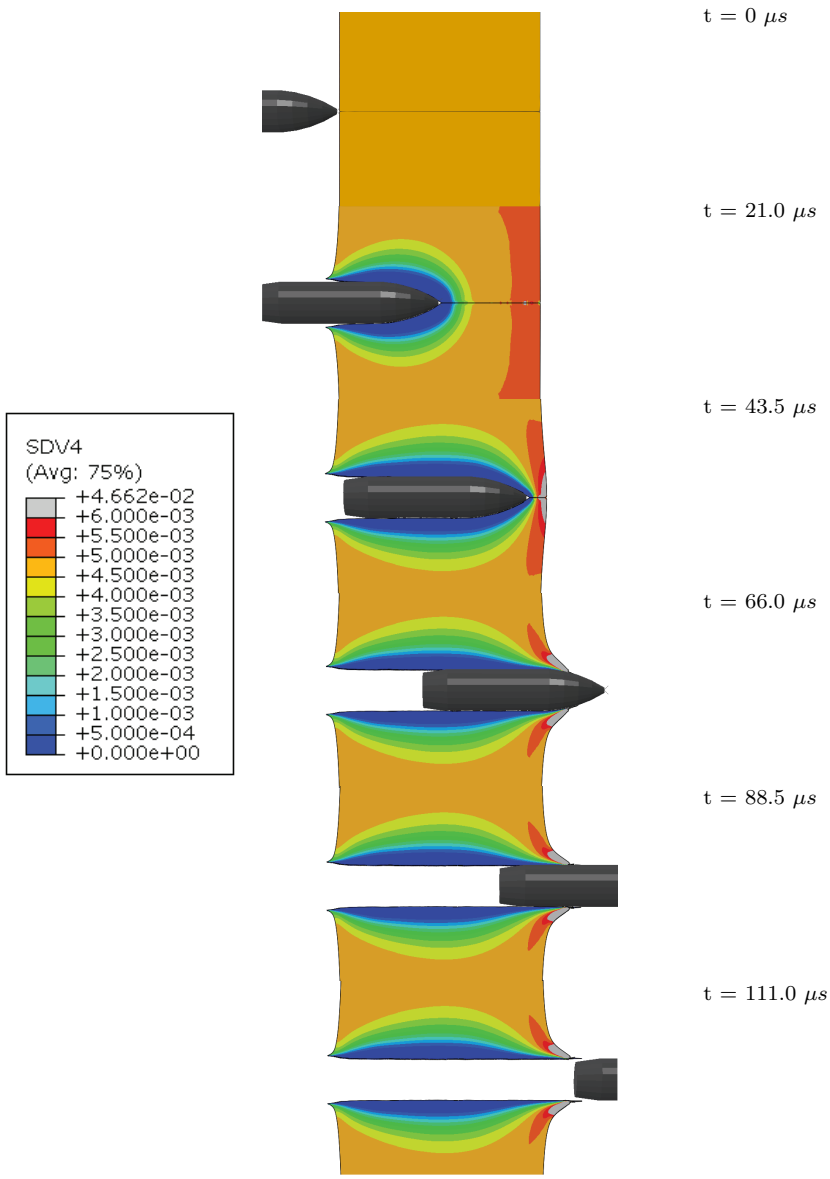

Figure 7.11: *Time-lapse illustrating the penetration process with the GTN model and adiabatic heating in Abaqus. The legend shows the void volume fraction.* $v_i = 700$ m/s *and* $v_r = 500.5$ m/s.

Figure 7.11 shows the void volume fraction contour plot for the penetration process with GTN and adiabatic heating. Observations reveal that the voids are closing right in front of the bullet, and the bullet is able to perforate the target due to the temperature erosion criterion. Note that the void volume fraction is equal to the damage parameter, i.e., $f = \omega$. One can see that as the bullet penetrates the target, the voids grow near the exit

region, and a few elements are eroded due to the high void volume fraction. A critical void volume fraction of $f_c = 0.0470$ was used, as this value is the average of the critical void volumes for the computational cells with $\mu_\sigma = -1$. Note that this is the lowest critical void volume fraction of the different Lode parameters from the computational cells, and it should therefore be the most conservative.

The results from the analyses with the GTN model with adiabatic heating and temperature erosion is presented, and compared to the CL analyses in Abaqus, in Table 7.5. Small differences are observed between the two failure models. Although some elements are eroded on the critical void volume fraction, the temperature erosion criterion is believed to dominate the results.

Table 7.5: *Recht-Ipson parameters with the Cockcroft-Latham and Gurson-Tvergaard-Needleman fracture models in Abaqus.*

Fracture model	a	p	v_{bl} [m/s]	Rel. Diff.
Experiment	0.9851	2.1072	517.5	Ref.
CL with $W_c = 174.1$ MPa	0.9943	2.0450	491.4	-5.0%
CL with $W_c = 364.3$ MPa	0.9990	2.0247	495.0	-4.3%
GTN	0.9810	2.0980	497.6	-3.8%

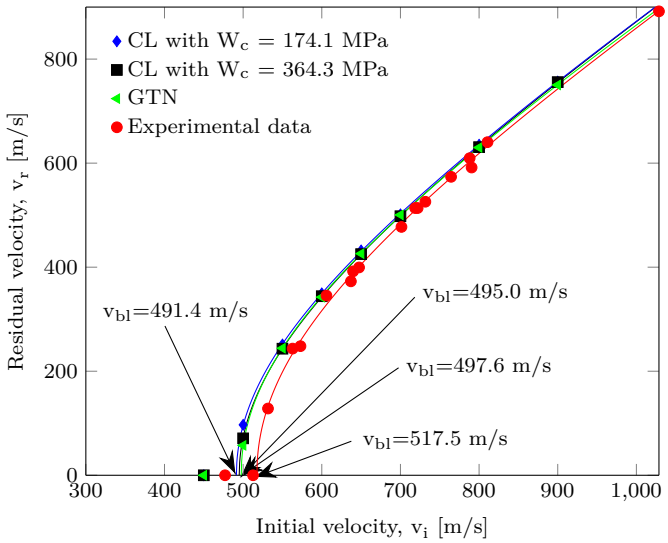

Figure 7.12: *Ballistic limit curves with the CL and GTN fracture models in Abaqus.*

Figure 7.12 presents the ballistic limit curves corresponding to Table 7.5. The curves are hard to distinguish, and only small differences can be seen.

7.4.3 The Modified Gurson model with Softening in Shear

The ballistic impact is believed to be dominated by shear, and the shear softening term in the GTN model was therefore implemented in the user-subroutine. First, the effect of the shear softening term in the GTN model is investigated in Section 7.4.3.1, using different values of the shear softening parameter k_s. Further, Section 7.4.3.2 presents the results from analyses using the parameters calibrated from the computational cells. Note that the void volume fraction is no longer equal to the damage parameter, i.e., $f \neq \omega$.

7.4.3.1 The Effect of Shear Softening

Figure 7.13 shows the contribution to the damage parameter from the shear softening term in the GTN model. The largest influence is seen around the exit region, to the right in the figure. A smaller contribution is seen near the entry region. Although the shear softening term contributes to an increase in the damage parameter, the void growth term may be negative and result in no increase or a decrease in the overall damage parameter. This can be seen by comparing Figures 7.13 and 7.14, especially in the entry region.

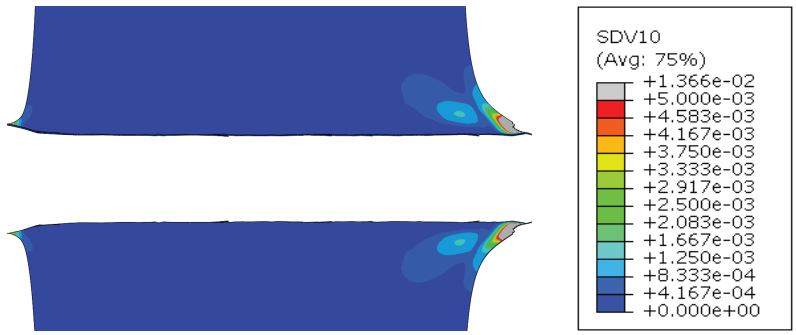

Figure 7.13: *Contribution to the damage parameter from the shear softening term, ω_s, for $k_s = 1$. $v_i = 700$ m/s and $v_r = 500.9$ m/s. Entry from the left.*

The effect of the shear softening parameter can be seen in Figure 7.14, where two different values for k_s are shown. Note that a value of 10 might be unreasonably high. Nahshon and Hutchinson [18] identified a reasonable range for the shear softening parameter, with $1 \leq k_s \leq 3$. For $k_s = 1$, one can see that a small amount of elements have been eroded in the exit region, and no one in the entry region, due to material failure. A larger amount of elements can be seen to have eroded for $k_s = 10$. A few have eroded in the entry region, and the exit region is highly effected.

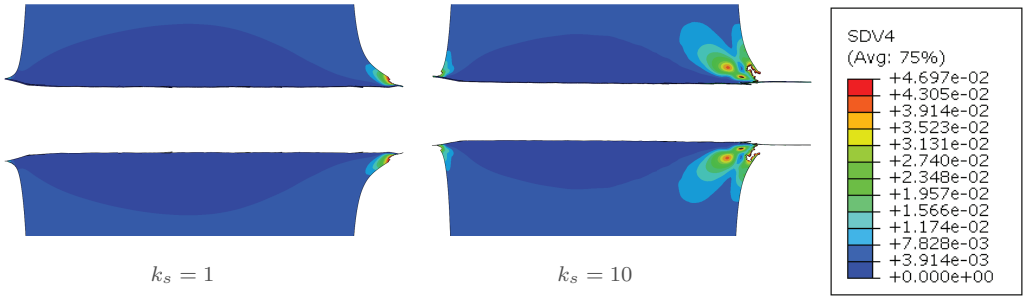

Figure 7.14: *Comparison of different shear softening parameters effect on the damage parameter, ω, for $v_i = 700$ m/s. $k_s = 1$ yields $v_r = 500.9$ m/s and $k_s = 10$ yields $v_r = 504.4$ m/s. Entry from the left.*

The shear softening parameter was further increased to see if the entry region and the penetration channel could be influenced. Figure 7.15 shows the effect with $k_s = 50$. This is an unrealistic high value only used to illustrate the effect of softening in shear. In front of the bullet, the region with dark blue colour in the figure, is compressed and no increase in damage parameter occur. The area just outside seems to be affected by the shear forces between the compressed material in front of the bullet and the surrounding material, forming shear bands in the direction of the penetration process where elements are eroded.

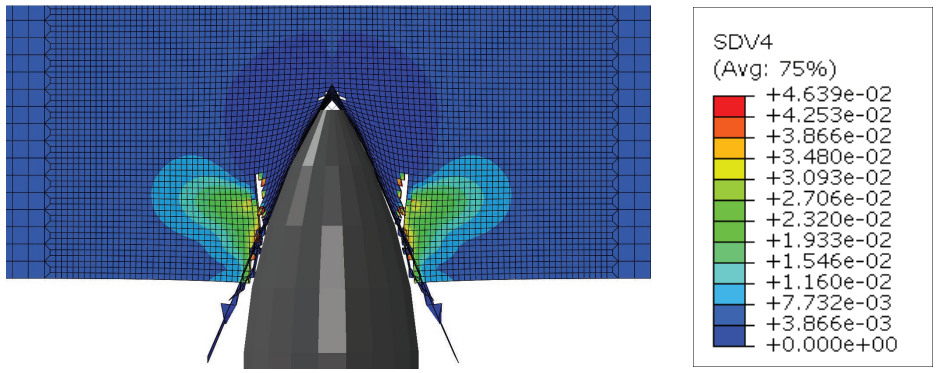

Figure 7.15: *Influence of the shear softening term with $k_s = 50$.*

7.4.3.2 Results

Parameters calibrated in Sections 5.4.1 and 5.4.2 are used to obtain the final result with the GTN model with softening in shear. Figure 7.16 shows the penetration process. An increase in the damage parameter is observed in both the entry and exit regions, but a larger influence is seen near the exit. When comparing Figures 7.11 and 7.16 one can observe the influence of the shear softening term through the whole penetration process. A

clear difference is seen, and the damage parameter is higher during the whole penetration process when shear softening is included.

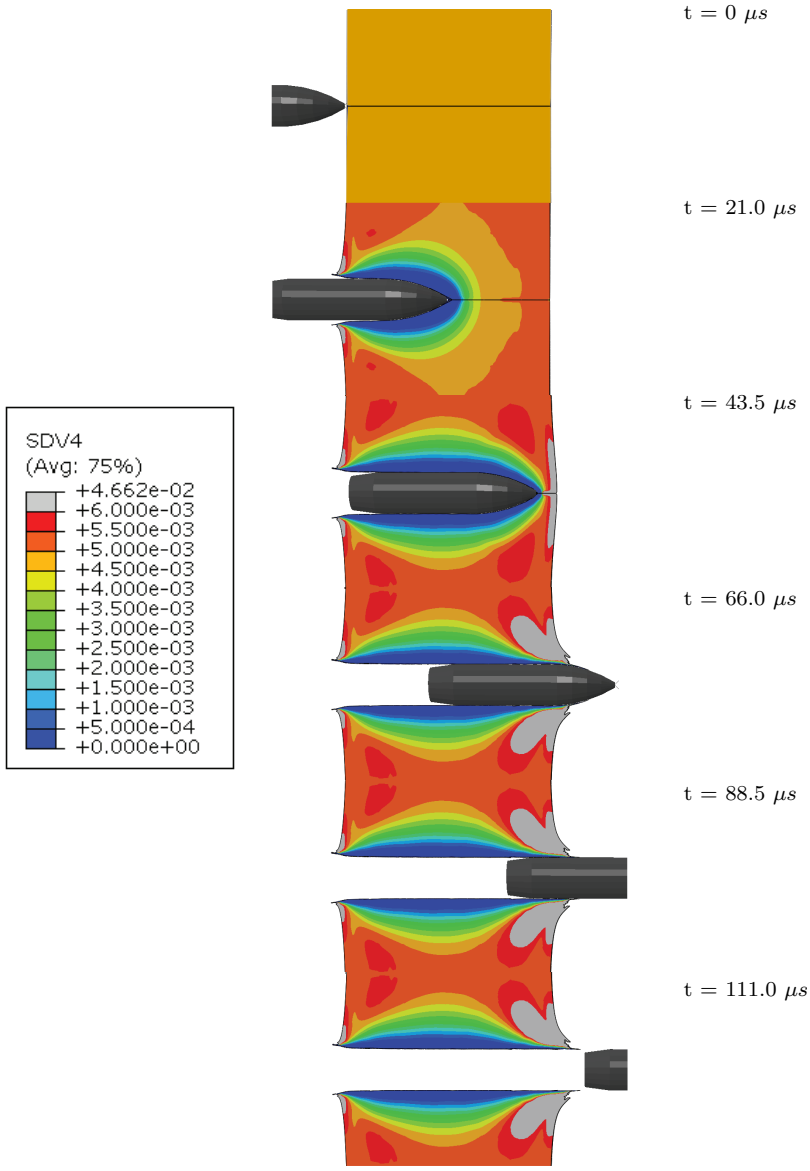

Figure 7.16: *Time-lapse illustrating the penetration process with the GTN model and softening in shear in Abaqus, with the calibrated shear parameter $k_s = 5.25$. The legend shows the damage parameter, with a critical value of $\omega_c = 0.0470$. $v_i = 700$ m/s and $v_r = 503.5$ m/s.*

In the entry region, a small amount of elements have been eroded due to the failure

criterion. A greater amount of elements are eroded in the exit region which is observed to be more affected. The residual velocity is larger for the analyses with shear softening included. It is therefore concluded that the penetration process is affected by shear softening. The process is probably not as dependent on the temperature criterion, but this is still needed to perforate the target.

Table 7.6 presents all results from Abaqus, and compares the results from the CL criterion with the GTN model. The shear softening term in the GTN model reduces the ballistic limit by 4.2 m/s, which is a larger difference than between the two CL parameters.

Table 7.6: *Recht-Ipson parameters with the Cockcroft-Latham and Gurson-Tvergaard-Needleman fracture models in Abaqus, including the shear softening term.*

Fracture model	a	p	v_{bl} [m/s]	Rel. Diff.
Experiment	0.9851	2.1072	517.5	Ref.
CL with $W_c = 174.1$ MPa	0.9943	2.0450	491.4	-5.0%
CL with $W_c = 364.3$ MPa	0.9990	2.0247	495.0	-4.3%
GTN	0.9810	2.0980	497.6	-3.8%
GTN with shear softening	0.9893	2.0643	493.4	-4.7%

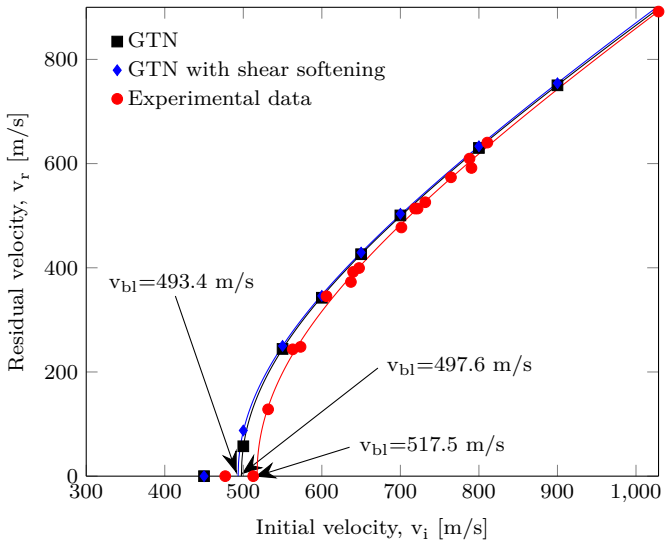

Figure 7.17: *Ballistic limit curves with the GTN model in Abaqus.*

The two ballistic limit curves from the analyses with the GTN model is shown in Figure 7.17, together with the experimental results. A small difference can be seen between the two curves with the GTN model.

7.5 Comparison of Deformation Pattern

Two selected tests with initial velocities $v_i = 810.7$ m/s and $v_i = 1028.7$ m/s from the experimental results presented in Table 3.5 in Section 3.5, were analysed to compare the deformation pattern. The selected tests correspond to the two tests studied in the macro- and microscopy, presented in Section 3.6. Simulations were run in both Abaqus and IMPETUS using a CL parameter of $W_c = 364.3$ MPa, in addition to a pinhole analysis. The residual velocities from the analyses are presented in Table 7.7.

As seen in the table, there is overall good correspondence between the analyses and the experimental data. The results for the highest initial velocity are observed to give generally better agreement than the lower. One possible reason for this is that for higher initial velocities, the ballistic limit curve lies closer to the ballistic limit line, and hence the relative difference will be smaller. The reader is referred to Section 2.1.2 for further information regarding the ballistic limit line.

Table 7.7: *Residual velocities for analyses in Abaqus and IMPETUS with CL parameter* $W_c = 364.3$ *MPa and pinhole analyses, compared with experimental results.*

Analysis	Initial velocity v_i [m/s]	Residual velocity v_r [m/s]	Rel. Diff.
Experiment	810.7	640.3	Ref.
Abaqus		643.6	+0.5%
Pinhole		659.3	+3.0%
IMPETUS		677.9	+5.9%
Experiment	1028.7	891.8	Ref.
Abaqus		903.1	+1.3%
Pinhole		913.0	+2.4%
IMPETUS		915.6	+2.7%

Figure 7.18 shows the penetration channel for the three analyses run with initial velocity $v_i = 810.7$ m/s and the corresponding experimental test. Note that the entry is located at the top of the picture. The deformation pattern is observed to be close to identical for all four cases. Smooth surfaces are seen in the penetration channel, in addition to some petalling in the exit. This indicates that all the analyses are capable of re-creating the ballistic impact.

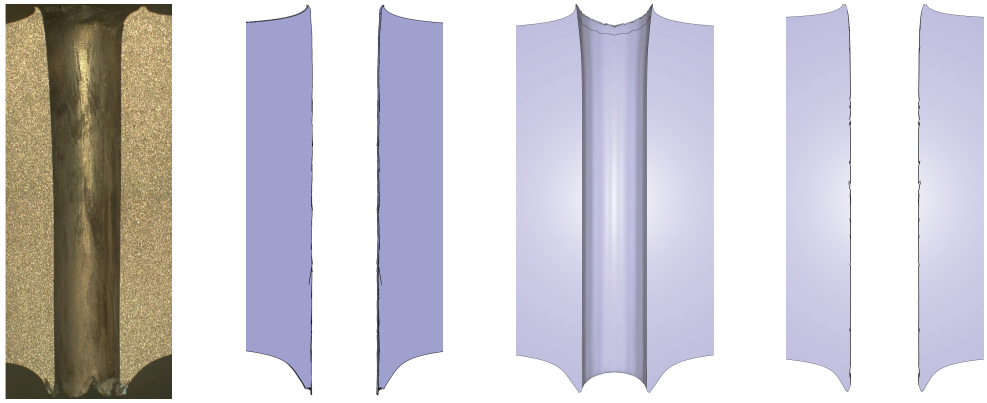

Figure 7.18: *Deformation pattern comparison of Abaqus, pinhole and IMPETUS analyses with an initial velocity of* $v_i = 810.7$ m/s. *Entry from above.*

The deformation pattern for the three analyses run with initial velocity $v_i = 1028.7$ m/s is shown in Figure 7.19. The extreme deformation seen in the entry for the experiment cannot be seen as clearly for the numerical analyses. Since $v_i = 1028.7$ m/s lies in the upper range of the ordnance velocity regime, density is of greater importance, and a hydrodynamic description of the material is probably necessary to properly recreate the experiment. Although no hydrodynamic description was implemented in the numerical models, the pinhole model shows signs of a conical entry as for the experimental test. The analyses in Abaqus and IMPETUS do not exhibit this deformation in the same extent as the pinhole analysis.

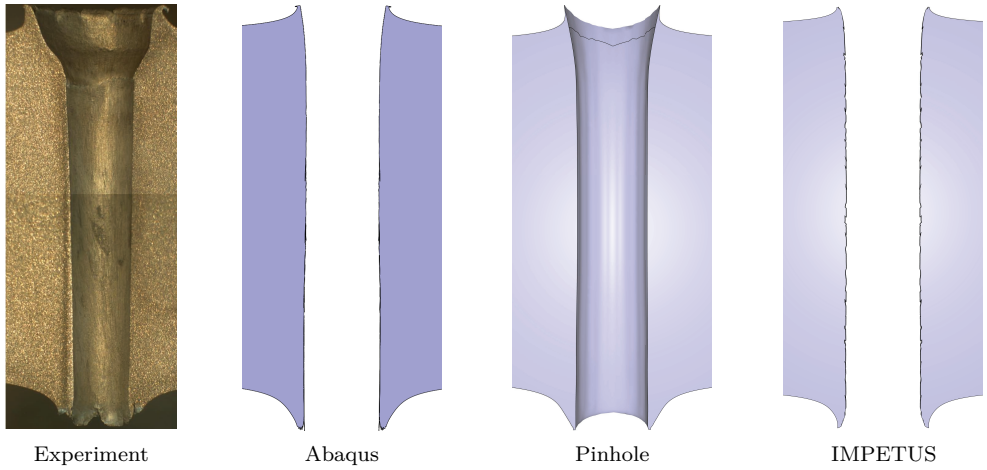

Figure 7.19: *Deformation pattern comparison of Abaqus, pinhole and IMPETUS analyses with an initial velocity of* $v_i = 1028.7$ m/s. *Entry from above.*

The IMPETUS analysis show best correspondence with the experiment in the exit area. This is clearly seen by studying the pictures from the microscopy, shown in Figure 3.28 in Section 3.6.

Comparison of the deformation patterns presented in Figures 7.18 and 7.19 reveal that for lower initial velocities in the ordnance velocity regime, all three numerical models recapture the deformation from the experiments. For velocities close to the ultra-ordnance velocity regime, a hydrodynamic material description may be necessary to properly re-create the deformation pattern seen in the experiments. Only the test with the highest initial velocity, $v_i = 1028.7^{\text{m}}/_{\text{s}}$, exhibited extreme deformation in the entry. By studying all entry and exit holes presented in Appendices A and B, the deformation patterns are similar to the ones presented in Figure 7.18, the only exception being the test with initial velocity $v_i = 1028.7^{\text{m}}/_{\text{s}}$.

7.6 Discussion

In this chapter, we have investigated the results from the numerical analyses in IMPETUS and Abaqus with different fracture criteria. The ballistic limits for the analyses are summarised in Table 7.8. Unfortunately, some of the criteria were unavailable either in IMPETUS or Abaqus, and could therefore not be compared. It would have been particularly interesting to see how the GTN model with shear softening would have behaved in IMPETUS, compared to the CL and JC fracture criteria commonly used in impact analyses, but this was not possible.

Table 7.8: *Ballistic limit velocities for analyses in Abaqus and IMPETUS using the Cockcroft-Latham, Johnson-Cook and Gurson-Tvergaard-Needleman models.*

FEM model	Fracture model	v_{bl} [m/s]	Rel. Diff.
Experiment	Experiment	517.5	Ref.
Abaqus	CL with $W_c = 174.1$ MPa	491.4	-5.0%
	CL with $W_c = 364.3$ MPa	495.0	-4.3%
	GTN	497.6	-3.8%
	GTN with shear softening	493.4	-4.7%
IMPETUS	CL with $W_c = 174.1$ MPa	384.4	-25.7%
	CL with $W_c = 364.3$ MPa	467.2	-9.7%
	JC	419.2	-19.0%

Analyses run with Abaqus gave the best compliance to the experimental results, but the fracture criteria are seen to have minor influence on the response. The IMPETUS results are highly affected by the fracture criteria, but the deviations from the experimental results are large.

The negligible differences between the Abaqus results are believed to be due the temperature erosion criterion needed for the Abaqus model. Børvik [44] pointed out that a temperature erosion criterion is as valid as any other erosion criterion. The physical nature of the problem is dominated by temperature and material softening. The bullet holes from the experiments, investigated in Section 3.6, showed no sign of any melted material, but the temperatures were undoubtedly high.

Temperature erosion was not needed in IMPETUS, probably because of how the third-order elements and erosion technique 2 behave together. The other erosion techniques in IMPETUS, presented in Section 6.2.2, needed a critical time step erosion criterion. Erosion technique 2 is believed to be most similar to the erosion technique in Abaqus.

The results from the IMPETUS analyses showed a large difference between the fracture criteria, and the JC fracture criterion gave a much lower ballistic limit than the CL criterion fitted to the same computational cells, presented in Chapter 5. This difference was not seen in Section 5.3 for the tensile test comparison. Therefore an element in the target was selected, and the accumulated plastic strain was investigated, revealing a much lower failure strain for the JC criterion. One possible reason for this difference is believed to be the nature of the two fracture criteria. Cockcroft-Latham is driven by plastic straining, but the damage parameter only increase when the maximum principal stress is positive. The Johnson-Cook criterion is also driven by plastic straining, but the fracture strain is only a function of the stress state. Therefore, the damage parameter will always increase for increasing plastic strain with the Johnson-Cook model.

The discrepancies between the IMPETUS analyses and the experimental results are affected by the FE mesh. In Chapter 6, the IMPETUS analyses proved to be highly mesh sensitive, and a mesh was selected based on computational time. The IMPETUS results would therefore have been more accurate, and a better compliance to the experimental results could have been achieved, if more computing power had been available.

Other factors influencing the results are the parameters for strain rate, temperature softening and friction, investigated in Section 6.1.

All results from Abaqus are considered good and Abaqus predicts the ballistic limit with little error. The IMPETUS results on the other hand deviates more, and the CL criterion calibrated from the computational cells are the only one that is within 10% of the experimental results. According to Børvik [44], prediction within 10% of the experimental results is considered good. All analyses in both Abaqus and IMPETUS were conservative with respect to the experimental results.

The small study conducted to investigate the deformation pattern for Abaqus, pinhole and IMPETUS analyses showed that all models were able to recreate the experimental test for initial velocities well within the ordnance velocity regime. The only exception was the test with initial velocity $v_i = 1028.7 \frac{\text{m}}{\text{s}}$, which is believed to be highly affected by hydrodynamic like forces. It was therefore hard to properly reproduce the deformation pattern for this velocity.

8 | Concluding Remarks

In this thesis, ballistic impact experiments were conducted on isotropic AlMgSi target plates using the steel core of 7.62 APM2 bullets. The ballistic limit curve was obtained from the experimental results. Numerical analyses of micromechanical computational unit cells were used to calibrate different macro-scale fracture models, i.e., the Cockcroft-Latham, Johnson-Cook and Gurson-Tvergaard-Needleman models. The fracture criteria were used in numerical analyses in both IMPETUS and Abaqus, to investigate the importance of ductile fracture for the AlMgSi-alloy and to recapture the same deformation trends seen for the ballistic impact experiments.

The most important results and conclusions from the work with this thesis are presented in the following.

Experimental Results

The three tensile tests performed to verify the material data by Westermann et al. [41], gave unexpected results, and was therefore not used. The data points from the ballistic experiments, on the other hand, gave good correspondence with the Recht-Ipson curve.

In the light optical microscope, no signs of melted material was found even though this was expected, for some of the tests, due to high initial velocities and large plastic strains. The numerical analyses in Abaqus proved to be highly dependent on temperature erosion of elements. There exists a possibility that the material has melted even though this could not be confirmed by the rather limited microscopical investigations.

The preliminary numerical study proved to give lower ballistic limit velocity than the experimental results, with $v_{bl} = 428.0^{\text{m}}/_{\text{s}}$ versus $v_{bl} = 517.5^{\text{m}}/_{\text{s}}$. Reasons for this discrepancy seemed to be significant friction forces, as well as strain rate dependency at high temperatures, which were not included in the preliminary model. These effects were studied and included in the final numerical model.

All plates experienced ductile hole growth, which was the dominant failure mechanism. Minimal fragmentation and small degrees of petalling near the exit holes were observed, with higher occurrence for tests with high initial velocities.

Micromechanical Computational Unit Cells

When studying the computational cells, some differences were observed between the generalized tension and generalized compression loading cases. It was harder to determine coalescence for generalized compression, $\mu_\sigma = 1$, and it was eventually decided to use the change in ligament thickness to establish the point of coalescence since a uniaxial deformation mode did not occur as for generalized tension, $\mu_\sigma = -1$. The trend observed regarding change in ligament thickness for $\mu_\sigma = 1$ was also observed for $\mu_\sigma = -1$ near coalescence.

Inclusion of the Gurson-Tvergaard-Needleman model in the unit cell matrix resulted in lower critical equivalent strains for both generalized tension and generalized compression, which was as expected. For generalized compression, coalescence was defined when the void volume fraction in the matrix was equal to $f = {}^1/_{q_1}$, due to collapse of the yield surface. Two different ways were used to define coalescence for the von Mises yield criterion and GTN in the matrix, and the results from the two generalized compression cases were therefore not directly comparable. It is believed that inclusion of a secondary void in the critical region in the matrix could have solved this problem.

It was observed that the correspondence between the two-dimensional and three-dimensional cells were overall good for the axisymmetric cells, but the plane strain cells only gave acceptable agreement for triaxiality ratio $\sigma^* = 0$. This discrepancy is probably a result of the use of different void shapes. The plane strain cells have a cylindrical void instead of a spherical void. This does not affect the shear cell with $\sigma^* = 0$ as much, since coalescence is defined using another criterion than the occurrence of a uniaxial deformation mode. Due to the difference in void shape, the plane strain cell could not be compared with the axisymmetric cells.

Calibration of Fracture Models

The Cockcroft-Latham, Johnson-Cook and Gurson-Tvergaard-Needleman fracture models were calibrated to the computational cell data. The CL model was additionally calibrated to experimental tensile test data. Quite large discrepancies were seen for the CL fracture parameters, where W_c for the computational cells were approximately twice the value of W_c from the tensile tests. The simplified two-dimensional cells with only one initial void in the matrix is believed to be too stiff, and hence result in a too large value for W_c. By including GTN in the matrix, the parameters for both the CL model and the JC model decreased.

The different fracture parameters for CL and JC were compared by executing numerical tensile tests in IMPETUS. It was observed that fracture occurred later for CL calibrated to the computational cells, which was expected due to higher fracture parameter W_c. The overall correspondence between the two fracture models were relatively good, but larger discrepancies were seen when the models were calibrated to computational cell data with GTN in the matrix.

The GTN model was only calibrated to the axisymmetric cell in generalized tension, $\mu_\sigma = -1$, due to the troublesome determination of coalescence for generalized compression. The results would probably have been insignificantly affected if the calibration were done to $\mu_\sigma = 0$ or $\mu_\sigma = 1$. It was shown that for a given triaxiality ratio, several combinations of the GTN parameters q_1 and q_2 could yield good correspondence. Note that when taking several triaxialities into account, only one set of values gave the best fit.

Calibration of the shear softening term in the modified Gurson model was done using the data from the two-dimensional plane strain shear cell. The parameter was a bit higher than what was suggested by Nahshon and Hutchinson [18].

Preliminary Numerical Study

The effects of strain rate, temperature and friction were studied. Both strain rate and friction proved to be significant for the ballistic limit, with friction being the most important. The temperature parameter did only have a consequential influence for $m \leq 1$.

Different element erosion techniques were studied in IMPETUS, and the final choice fell on a method that clearly showed a difference between the two CL parameters and allowed for the use of friction.

The `*CONTACT_SUPER` algorithm resulted in problems for some analyses regarding the energy balance. These analyses were rerun using the standard `*CONTACT` algorithm, which fixed the problem.

The mesh sensitivity studies did only achieve convergence for the analyses in Abaqus. 0.2 mm elements were chosen since they gave good correspondence with experimental tests, and had an acceptable CPU-time. It was discovered that by using a lower fracture parameter in IMPETUS, the analyses seemed to become more mesh sensitive.

Numerical Analyses

The three calibrated fracture models were used in the penetration analyses in IMPETUS and Abaqus. A distinct difference were seen between the models in IMPETUS, but in Abaqus they gave almost identical results. The reason for the negligible differences in Abaqus is probably due to temperature erosion.

Analyses were run with the GTN model, both with and without the shear softening term. It was discovered that the effects of shear softening were significant. Different shear parameters were investigated, and proved to affect element erosion. With only the GTN model, merely a few elements near the exit were eroded due to the fracture criterion. By including, and varying, the shear softening term more elements were eroded due to the fracture criterion, also in the entry of the penetration channel.

The numerical analyses show ductile hole growth as the dominating failure mechanism, with only small amounts of fragmentation near the exit region. This indicates that the model recaptures the ballistic perforation mode from the experiments.

From Table 7.8, it is seen that the Abaqus analyses had better agreement with the experimental results than the IMPETUS analyses. The main reason for this is probably that most elements were eroded due to temperature, and not the fracture criterion. This basically means that the fracture criterion is of less importance for the analyses in Abaqus. The discrepancies seen between the IMPETUS analyses and experimental results are believed to be due to the selected element size and the erosion technique. Note that all results are conservative with respect to the experiments, which is preferable when designing protective structures.

Generally it can be concluded that the CL, JC and GTN model with shear softening work for penetration problems. GTN without the shear term resulted in closing of the initial voids due to large pressure forces in front of the bullet. Although the results with this

method gave the best correspondence with the experimental ballistic limit velocity, it is believed that the other methods are better at describing the ductile fracture process.

Due to the inconsistencies seen between Abaqus and IMPETUS, it is hard to determine the importance of a ductile fracture criterion for the AlMgSi-alloy in ballistic impacts. In the IMPETUS analyses, it was observed that the fracture criteria had a significant influence on the penetration process, while the Abaqus analyses were not as affected. It was believed that by doubling the fracture parameter, a clear difference would be seen in the ballistic limit velocity, which was only observed for the IMPETUS analyses. It is therefore hard to determine which solver that gives the most accurate results. Nevertheless, calibration based on micromechanical unit cells is considered promising.

9 Future Work

New experimental tests
The tensile tests conducted for this thesis gave very unexpected results. It would therefore be desirable to execute new tensile tests. In addition, it would have been interesting to perform experimental tests to investigate the shear properties of the AlMgSi-alloy. This is believed to be particularly interesting for calibration of the shear softening term in the modified Gurson model.

Experimental tests at elevated temperatures
Vilamosa et al. [55] showed that aluminium is rate dependent at temperatures above 50% of the melting temperature. Experimental tests at elevated temperatures should therefore be performed to obtain the strain rate properties of the AlMgSi-alloy.

Ballistic impact with blunt projectiles
An investigation of the material behaviour during ballistic impacts with flat ended projectiles could be valuable. It is believed that the blunt projectile is better at capturing the shear phenomenon.

Ballistic impact using thinner plates
Some numerical difficulties have been present for the analyses of the perforation of the 30 mm thick plates in Abaqus, regarding temperature erosion. Due to high pressure forces in front of the bullet, most of the elements are eroded due to temperature. The fracture criteria have therefore minor influence. It is believed that use of thinner plates may solve this problem. Thin plates will result in a different deformation pattern where the rear surface of the plate is affected earlier in the perforation process, which is believed to make it easier to see the effects of the fracture models.

Investigation of microstructure in SEM (fractography)
It was desirable to investigate the impacted target plates in a scanning electron microscope (SEM), to see if the material actually had melted locally. No signs of melted material were present in the light optical microscope.

Calibration of fracture models using data from three-dimensional computational cells
It was concluded that the plane strain cell could not be compared to the axisymmetric cell due to different void shapes, and the data obtained from analyses of $\mu_\sigma = 0$ were only used to calibrate the shear softening term in Gurson. It was shown that the data for $\mu_\sigma = 0$ affected both fracture parameters and fracture surfaces, and it is believed that calibration of the fracture models to three-dimensiontal cell data would have been more accurate.

Implementation of GTN for $\mu_\sigma = 0$
If a 3D computational cell had been used for the microscopic analyses, or if the 2D data

for plane strain had been comparable to the axisymmetric, GTN should have been used for $\mu_\sigma = 0$, such that the calibration of the fracture models included the three Lode parameters studied.

Investigating more Lode parameters
Another point of interest is an expansion of the computational cell analyses to include more Lode parameters. This would most likely result in more accurate calibration of the fracture models due to more calibration points.

Micromechanical computational cell analyses for low triaxialities
Since low triaxialities are expected for the experimental tests, it is of current interest to study computational cells with triaxialities in the range $0 < \sigma^* < 1/3$. It is believed that the results would look similar to the fracture strain-stress triaxiality curve presented in Nahshon and Hutchinson [18]. To obtain coalescence without infinite stretching, it would be necessary to include a particle to avoid closing the void.

Inclusion of secondary voids
One subject of particular interest is the inclusion of secondary voids in the matrix in addition to the primary void, and to compare the results with the analyses with GTN in the matrix. It was seen, especially for generalized compression, that with GTN in the matrix, a very high void volume fraction occured in a concentrated area. If this area was replaced with a void, the analyses could probably be run farther than in the study presented in this thesis. This means that it could actually be possible to directly compare data for generalized tension. Note that this inclusion of secondary voids is likely to reduce the material strength.

Mesh sensitivity study in IMPETUS
A more thorough study of the mesh sensitivity in IMPETUS should be conducted, since convergence was not achieved for the investigated mesh sizes. Analyses with even finer mesh should be performed. This will although demand a better IMPETUS computer server than the one used for this thesis.

Implementation of Johnson-Cook in Abaqus
The Johnson-Cook model in Abaqus did not work for the penetration analysis, and to be able to compare with the IMPETUS analyses a user-subroutine that accounts for adiabatic heating and temperature erosion will be needed. Note that since elements are eroded due to temperature, there will probably be negligible difference between the JC and CL fracture models in Abaqus.

Implementation of GTN in IMPETUS
It is desirable to use GTN for the analyses in IMPETUS, but at the moment there is no simple way of accomplishing this. No Gurson model is implemented in the IMPETUS code, and the Porous Plasticity Model developed at SIMLab is not up and running or compatible with IMPETUS. This should be looked into when the model is working.

Numerical analyses of ballistic impacts including data for generalized shear
It would be interesting to investigate the effects of including the computational cell data for $\mu_\sigma = 0$ in the penetration analyses. Another aspect that should be looked into is running analyses for the CL and JC models calibrated to the cell data with GTN in the

matrix. In this thesis, only parameters calibrated to cell data excluding $\mu_\sigma = 0$, as well as tensile test data, have been used.

Element erosion in IMPETUS

Element erosion techniques proved significant for the perforation process. For erosion technique 2, an element is eroded when 16 out of 64 integration points reach the critical damage. If it was possible to control the critical number of integration points, this could be an interesting study.

References

[1] T. Børvik, A. H. Clausen, O. S. Hopperstad, and M. Langseth, "Perforation of AA5083-H116 aluminium plates with conical-nose steel projectiles—experimental study," *International Journal of Impact Engineering*, vol. 30, no. 4, pp. 367 – 384, 2004.

[2] T. Børvik, "An Introduction to Impact and Penetration Dynamics." SIMLAB/Department of Structural Engineering, NTNU, 2001.

[3] T. Børvik, M. J. Forrestal, and T. L. Warren, "Perforation of 5083-H116 aluminum armor plates with ogive-nose rods and 7.62 mm APM2 bullets," *Experimental Mechanics*, vol. 50, pp. 969 – 978, 2010.

[4] M. J. Forrestal, T. Børvik, and T. L. Warren, "Perforation of 7075-T651 aluminum armor plates with 7.62 mm APM2 bullets," *Experimental mechanics*, vol. 50, no. 8, pp. 1245–1251, 2010.

[5] T. Børvik, O. S. Hopperstad, and K. O. Pedersen, "Quasi-brittle fracture during structural impact of AA7075-T651 aluminium plates," *International Journal of Impact Engineering*, vol. 37, no. 5, pp. 537 – 551, 2010.

[6] K. O. Pedersen, T. Børvik, and O. S. Hopperstad, "Fracture mechanisms of aluminium alloy AA7075-T651 under various loading conditions," *Materials & Design*, vol. 32, no. 1, pp. 97 – 107, 2011.

[7] M. Fourmeau, *Characterization and modelling of the anisotropic behaviour of high-strength aluminium alloy*. PhD thesis, Norwegian University of Science and Technology, 2014.

[8] A. Needleman, "A numerical study of necking in circular cylindrical bar," *Journal of the Mechanics and Physics of Solids*, vol. 20, no. 2, pp. 111 – 127, 1972.

[9] V. Tvergaard, "Influence of voids on shear band instabilities under plane strain conditions," *International Journal of Fracture*, vol. 17, pp. 389 – 407, 1981.

[10] V. Tvergaard, "On localization in ductile materials containing spherical voids," *International Journal of Fracture*, vol. 18, pp. 237 – 252, 1982.

[11] J. Koplik and A. Needleman, "Void growth and coalescence in porous plastic solids," *International Journal of Solids and Structures*, vol. 24, no. 8, pp. 835 – 853, 1988.

[12] A. Needleman, "A Continuum Model for Void Nucleation by Inclusion Debonding," *Journal of Applied Mechanics*, vol. 54, no. 3, pp. 525 – 531, 1987.

[13] A. A. Benzerga and J. B. Leblond, "Ductile Fracture by Void Growth to Coalescence." 2010.

[14] F. A. McClintock, "A criterion for ductile fracture by the growth of holes," *Journal of Applied Mechanics*, vol. 35, no. 2, pp. 363 – 371, 1968.

[15] J. R. Rice and D. M. Tracey, "On the ductile enlargement of voids in triaxial stress fields," *Journal of Mechanics and Physics of Solids*, vol. 17, no. 3, pp. 201 – 217, 1969.

[16] A. L. Gurson, "Continuum Theory of Ductile Rupture by Void Nucleation and Growth: Part I - Yield Criteria and Flow Rules for Porous Ductile Media," *J. Eng. Mater. Technol.*, vol. 99, pp. 2–15, 1977.

[17] V. Tvergaard and A. Needleman, "Analysis of the cup-cone fracture in a round tensile bar," *Acta Metallurgica*, vol. 32, no. 1, pp. 157 – 169, 1984.

[18] K. Nahshon and J. W. Hutchinson, "Modification of the Gurson Model for shear failure," *European Journal of Mechanics A/Solids*, vol. 27, pp. 1–17, 2008.

[19] X. Gao and J. Kim, "Modeling of ductile fracture: Significance of void coalescence," *International Journal of Solids and Structures*, vol. 43, pp. 6277 – 6293, 2006.

[20] M. G. Cockcroft and D. J. Latham, "Ductility and the Workability of Metals," *Journal of the Insitute of Metals*, vol. 96, pp. 33–39, 1968.

[21] G. R. Johnson and W. H. Cook, "Fracture characteristics of three metals subjected to various strains, strain rates, temperatures and pressures," *Engineering fracture mechanics*, vol. 21, pp. 31–48, 1985.

[22] J. A. Zukas, "Impact Dynamics." John Wiley & Sons, Inc., 1982.

[23] M. E. Backman and W. Goldsmith, "The mechanics of penetration of projectiles into targets," *International Journal of Engineering Science*, vol. 16, no. 1, pp. 1 – 99, 1978.

[24] R. F. Recht and T. W. Ipson, "Ballistic Perforation Dynamics," *Int J Applied Mech (Trans. ASME)*, vol. 30, pp. 384–390, 1963.

[25] O. S. Hopperstad and T. Børvik, "KT8306 Plasticity Theory - Lecture Notes Part 2, Chapter 9." NTNU 2014.

[26] P. W. Bridgman *Trans. Am. Soc. Met.*, vol. 32, p. 553, 1944.

[27] G. Le Roy, J. D. Embury, G. Edwards, and M. F. Ashby, "A model of ductile fracture based on the nucleation and growth of voids," *Acta Metallurgica*, vol. 29 (8), pp. 1509–1522, 1981.

[28] T. L. Anderson, *Fracture mechanics.* Taylor and Francis, third ed., 2005.

[29] O. S. Hopperstad, M. Langseth, and T. Børvik, "Analysis of the Cockcroft-Latham and maximum shear stress criteria for ductile fracture of metals," tech. rep., SINTEF, 2006.

[30] G. R. Johnson and W. H. Cook, "A constitutive model and data for metals subjected

to large strains, high strain rates and high temperatures," in *Proceedings of the 7th International Symposium on Ballistics*, vol. 21, pp. 541–547, 1983.

[31] T. Børvik, O. S. Hopperstad, T. Berstad, and M. Langseth, "A computational model of viscoplasticity and ductile damage for impact and penetration," *European Journal of Mechanics - A/Solids*, vol. 20, no. 5, pp. 685 – 712, 2001.

[32] G. T. Camacho and M. Ortiz, "Adaptive Lagrangian modelling of ballistic penetration of metallic targets," *Computer Methods in Applied Mechanics and Engineering*, vol. 142, no. 3–4, pp. 269 – 301, 1997.

[33] J. K. Holmen and J. Johnsen, "Effects of Heat Treatment on the Ballistic Properties of AA6070 Aluminium Plates," Master's thesis, Norwegian University of Science and Technology , 2012.

[34] R. Cook, D. Malkus, and R. Plesha, M. Witt, *Concepts and applications of finite element analysis*. John Wiley & sons inc., fourth ed., 2001.

[35] K. M. Mathisen, "Lecture 9: Solution of the Nonlinear Dynamic Equilibrium Equations." Lecture notes in TKT4197 - Nonlinear finite element analysis, 2014.

[36] "http://www.impetus-afea.com/solver." IMPETUS Afea Solver. Obtained in April 2015.

[37] L. Olovsson, "IMPETUS AFEA SOLVER - An introduction." February 2015.

[38] J. K. Holmen, 2015. Private communication.

[39] Structural Impact Laboratory (SIMLab), "SIMLab Metal Model (SMM) - Theory, user's and example manual." 2014.

[40] D. Morin, 2015. Private communication.

[41] I. Westermann, K. O. Pedersen, T. Furu, T. Børvik, and O. S. Hopperstad, "Effects of particles and solutes on strength, work-hardening and ductile fracture of aluminium alloys," *Mechanics of Materials*, vol. 79, pp. 58–72, 2014.

[42] J. K. Holmen, J. Johnsen, S. Jupp, O. S. Hopperstad, and T. Børvik, "Effects of heat treatment on the ballistic properties of AA6070 aluminium alloy," *International Journal of Impact Engineering*, vol. 57, pp. 119–133, 2013.

[43] T. Børvik, S. Dey, and A. H. Clausen, "Perforation resistance of five different high-strength steel plates subjected to small-arms projectiles," *International Journal of Impact Engineering*, vol. 36, no. 7, pp. 948 – 964, 2009.

[44] T. Børvik, 2015. Private communication.

[45] T. Børvik, M. Langseth, O. S. Hopperstad, and K. A. Malo, "Ballistic penetration of steel plates," *International Journal of Impact Engineering*, vol. 22, no. 9–10, pp. 855 – 886, 1999.

[46] T. Børvik, O. S. Hopperstad, M. Langseth, and K. A. Malo, "Effect of target thickness

in blunt projectile penetration of weldox 460 e steel plates," *International Journal of Impact Engineering*, vol. 28, no. 4, pp. 413 – 464, 2003.

[47] E. Orthe and H. Thorsen, "Ballistic Perforation of Surface Hardened Mild Steel Plates," Master's thesis, Norwegian University of Science and Technology, 2014.

[48] W. Goldsmith, "Non-ideal projectile impact on targets," *International Journal of Impact Engineering*, vol. 22, no. 2–3, pp. 95 – 395, 1999.

[49] I. Westermann, 2015. Private communication.

[50] O. S. Hopperstad, 2015. Private communication.

[51] L. E. Dæhli, 2015. Private correspondence.

[52] V. Tvergaard, "Material failure by void growth to coalescence," *Adv. Applied Mechanics*, vol. 27, pp. 83–151, 1990.

[53] Y. Bao and T. Wierzbicki, "On fracture locus in the equivalent strain and stress triaxiality space," *International Journal of Mechanical Sciences*, vol. 46, no. 1, pp. 81 – 98, 2004.

[54] X. Teng and T. Wierzbicki, "Evaluation of six fracture models in high velocity perforation," *Engineering Fracture Mechanics*, vol. 73, no. 12, pp. 1653 – 1678, 2006.

[55] V. Vilamosa, A. H. Clausen, O. S. Hopperstad, T. Børvik, and S. Skjervold, "Influence of temperature and strain rate on the mechanical behaviour of the aluminium alloy AA6060," *Materials Science Forum*, vol. 794-796, pp. 520–525, 2014.

[56] M. Ravid and S. R. Bodner, "Dynamic perforation of viscoplastic plates by rigid projectiles," *International Journal of Engineering Science*, vol. 21, no. 6, pp. 577 – 591, 1983.

[57] T. Børvik, L. Olovsson, S. Dey, and M. Langseth, "Normal and oblique impact of small arms bullets on AA6082-T4 aluminium protective plates," *International Journal of Impact Engineering*, vol. 38, no. 7, pp. 577 – 589, 2011.

A Front and Back side of All Target Plates

A.1 Plate 1

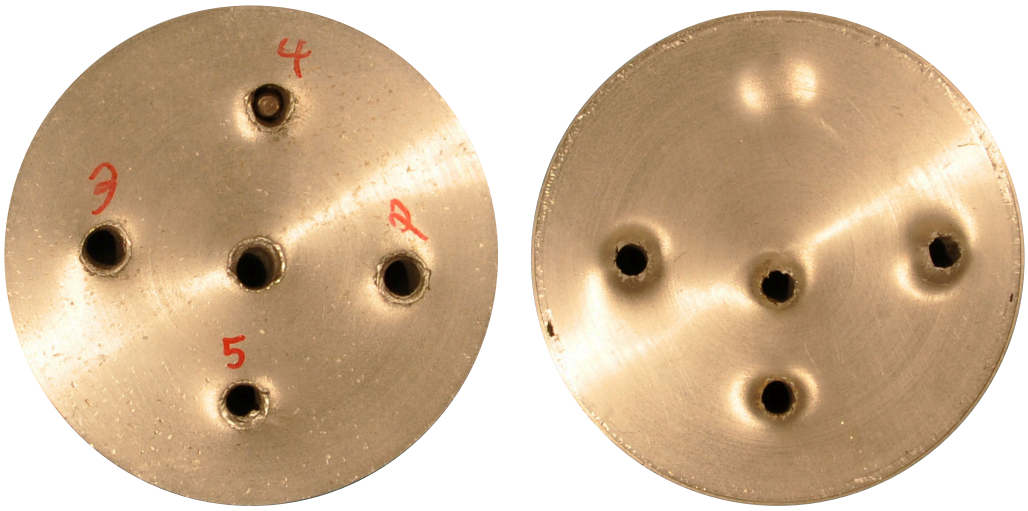

(a) Front. *(b) Back.*

Figure A.1: *Impacted target plate.*

A.2 Plate 2

(a) *Front.* ***(b)*** *Back.*

Figure A.2: *Impacted target plate.*

A.3 Plate 3

(a) *Front.* ***(b)*** *Back.*

Figure A.3: *Impacted target plate.*

A.4 Plate 4

(a) *Front.* ***(b)*** *Back.*

Figure A.4: *Impacted target plate.*

B | Entry and Exit Holes from Ballistic Experiments

B.1 Plate 1

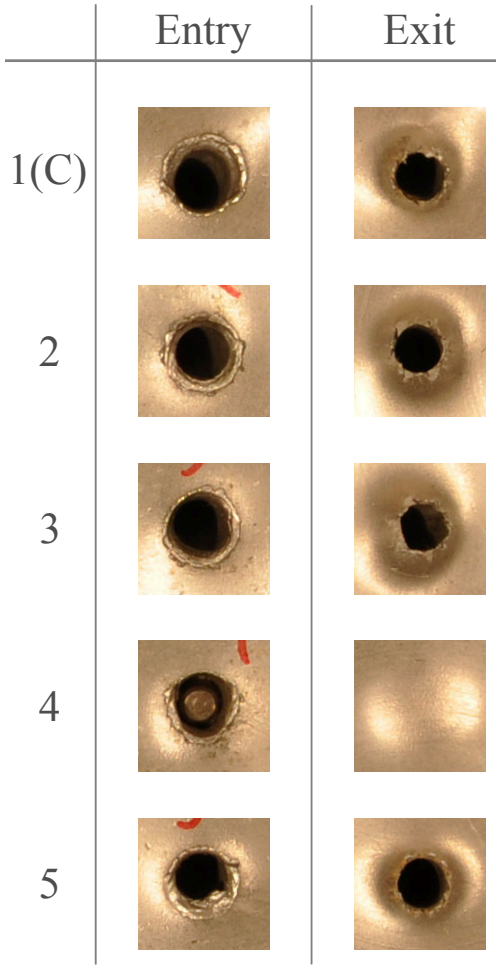

Figure B.1: *Entry and exit holes for plate 1 after ballistic impact. Locations correspond to impact locations illustrated in Figure 3.17, and Figure A.1 in Appendix A.*

B.2 Plate 2

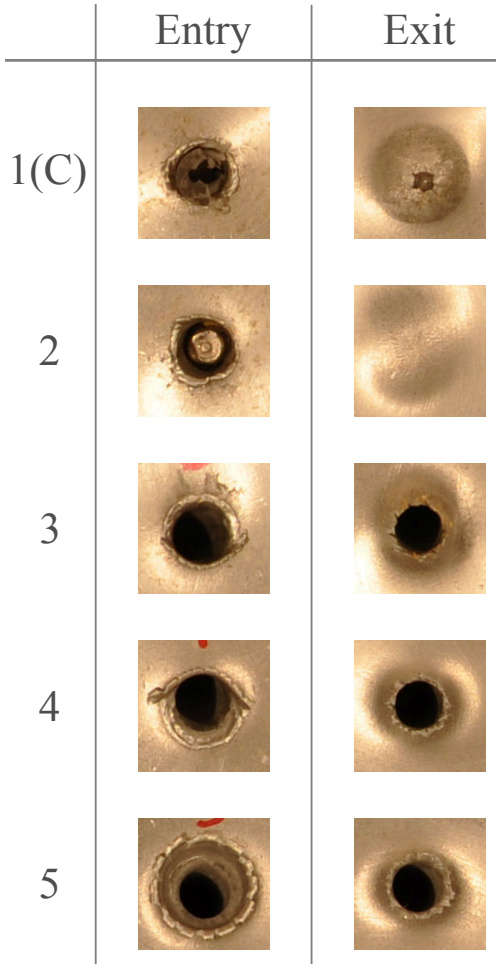

Figure B.2: *Entry and exit holes for plate 2 after ballistic impact. Locations correspond to impact locations illustrated in Figure 3.17, and Figure A.2 in Appendix A.*

B.3 Plate 3

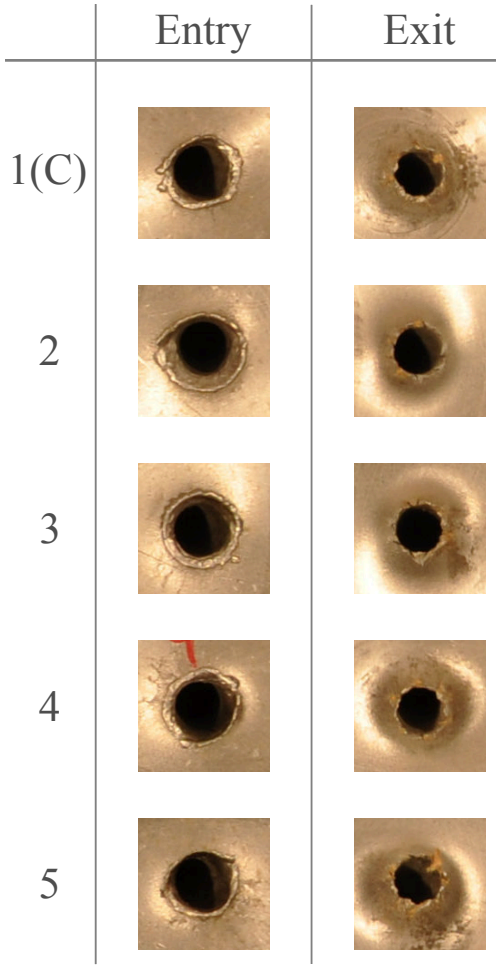

Figure B.3: *Entry and exit holes for plate 3 after ballistic impact. Locations correspond to impact locations illustrated in Figure 3.17, and Figure A.3 in Appendix A.*

B.4 Plate 4

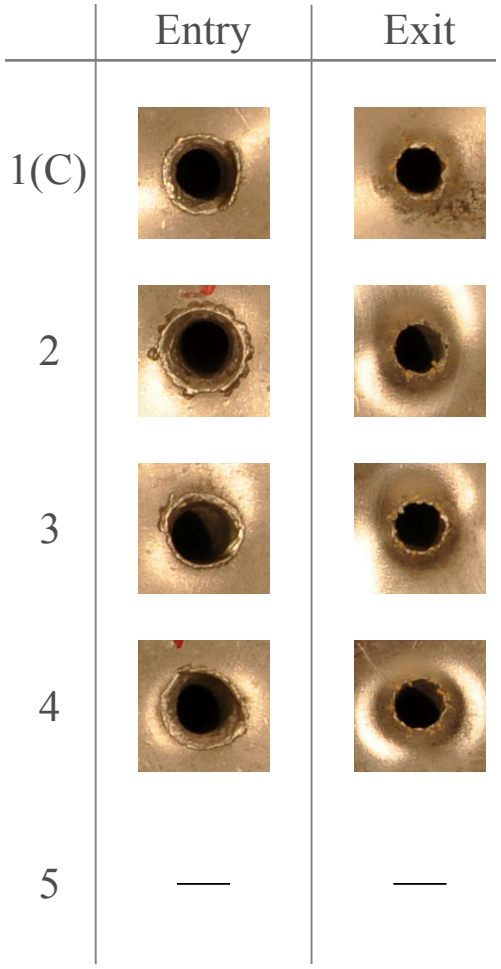

Figure B.4: *Entry and exit holes for plate 4 after ballistic impact. Locations correspond to impact locations illustrated in Figure 3.17, and Figure A.4 in Appendix A.*

C | Matlab Code

C.1 Ballistic Limit Curves

```
clc
clf
close all
clear

FontSize=16;
color={'c','m','g','k','r','b'};

%% Lab Data
Vi_lab=[790.5;562.9;572.9;512.6;647.4;637.0;477.0;788.0;810.7;1028.7;...
    764.4;605.9;639.8;531.6;701.3;718.7;721.9;731.7];
Vr_lab=[591.6;243.5;248.2;0.0;399.5;372.8;0.0;609.5;640.3;891.8;573.7;...
    345.4;392.0;128.3;477.4;513.7;513.7;525.8];

%% Base Model Data IMPETUS
Vi=[450,500,550,600,650,700,800,900];
Vr_Cell=[0,225.41,329.08,416.96,488.66,546.55,667.59,777.05];
Vr_JC=[171.35,295,364.41,434.65,494.28,553.94,671.12,780.67];
Vr_Strekk=[259.62,348.47,414.7,472.93,525.94,580.23,687.76,792.99];

%%  Base Model Data ABAQUS
Vr_Cell_ABA=[0,70.983,243.280,344.222,425.093,497.971,630.750,755.739];
Vr_Strekk_ABA=[0,96.937,251.341,349.655,432.167,501.570,635.332,756.719];
Vr_GTNSS=[0,87.692,250.023,346.069,429.136,503.536,633.325,754.229];
Vr_GTN=[0,57.374,244.204,342.484,426.053,500.483,630.016,750.277];

%% Curve Fit
% Fitting Lab data
n=0;
for i=1:length(Vi_lab)
    if Vr_lab(i)~=0
        n=n+1;
        vi_lab(n)=Vi_lab(i);
        vr_lab(n)=Vr_lab(i);
    end
end

[Vbl_lab,~]=RI_Fit(vr_lab,vi_lab);
a_lab=Vbl_lab.a;
p_lab=Vbl_lab.p;
Vbl_lab=Vbl_lab.Vbl;

vi_lab=linspace(Vbl_lab,max(Vi_lab),1000)';
vr_lab=a_lab*(vi_lab.^p_lab-Vbl_lab^p_lab).^(1/p_lab);
```

```
%% Fitting IMPETUS data
[fitresult,~]=RI_Fit(Vr_Cell(2:end),Vi(2:end));
a_Cell=fitresult.a;
p_Cell=fitresult.p;
Vbl_Cell=fitresult.Vbl;

[fitresult,~]=RI_Fit(Vr_Strekk,Vi);
a_Strekk=fitresult.a;
p_Strekk=fitresult.p;
Vbl_Strekk=fitresult.Vbl;

[fitresult,~]=RI_Fit(Vr_JC,Vi);
a_JC=fitresult.a;
p_JC=fitresult.p;
Vbl_JC=fitresult.Vbl;

%% Fitting Abaqus data
[fitresult,~]=RI_Fit(Vr_Cell_ABA(2:end),Vi(2:end));
a_Cell_ABA=fitresult.a;
p_Cell_ABA=fitresult.p;
Vbl_Cell_ABA=fitresult.Vbl;

[fitresult,~]=RI_Fit(Vr_Strekk_ABA(2:end),Vi(2:end));
a_Strekk_ABA=fitresult.a;
p_Strekk_ABA=fitresult.p;
Vbl_Strekk_ABA=fitresult.Vbl;

[fitresult,~]=RI_Fit(Vr_GTNSS(2:end),Vi(2:end));
a_GTNSS=fitresult.a;
p_GTNSS=fitresult.p;
Vbl_GTNSS=fitresult.Vbl;

[fitresult,~]=RI_Fit(Vr_GTN(2:end),Vi(2:end));
a_GTN=fitresult.a;
p_GTN=fitresult.p;
Vbl_GTN=fitresult.Vbl;

%% Creating Recht-Ipson Curves
vi_Cell_ABA=linspace(Vbl_Cell_ABA,max(Vi_lab),1000);
vi_Cell=linspace(Vbl_Cell,max(Vi_lab),1000);
vi_JC=linspace(Vbl_JC,max(Vi_lab),1000);
vi_Strekk=linspace(Vbl_Strekk,max(Vi_lab),1000);
vi_Strekk_ABA=linspace(Vbl_Strekk_ABA,max(Vi_lab),1000);
vi_GTNSS=linspace(Vbl_GTNSS,max(Vi_lab),1000);
vi_GTN=linspace(Vbl_GTN,max(Vi_lab),1000);
vr_Cell_ABA=a_Cell_ABA.*(vi_Cell_ABA.^p_Cell_ABA-...
    Vbl_Cell_ABA.^p_Cell_ABA).^(1./p_Cell_ABA);
vr_Cell=a_Cell.*(vi_Cell.^p_Cell-Vbl_Cell.^p_Cell).^(1./p_Cell);
vr_JC=a_JC.*(vi_JC.^p_JC-Vbl_JC.^p_JC).^(1./p_JC);
vr_Strekk=a_Strekk.*(vi_Strekk.^p_Strekk-Vbl_Strekk.^p_Strekk).^(1./p_Strekk);
vr_Strekk_ABA=a_Strekk_ABA.*(vi_Strekk_ABA.^p_Strekk_ABA-...
    Vbl_Strekk_ABA.^p_Strekk_ABA).^(1./p_Strekk_ABA);
vr_GTNSS=a_GTNSS.*(vi_GTNSS.^p_GTNSS-Vbl_GTNSS.^p_GTNSS).^(1./p_GTNSS);
vr_GTN=a_GTN.*(vi_GTN.^p_GTN-Vbl_GTN.^p_GTN).^(1./p_GTN);

%% Plotting
```

```
%% IMPETUS
% Plot fit with data.
h=figure('name','IMPETUS');
plot(Vi,Vr_Strekk,'bd','MarkerFaceColor','b')
hold on
plot(Vi,Vr_Cell,'ks','MarkerFaceColor','k')
plot(Vi_lab,Vr_lab,'ro','MarkerFaceColor','r')
plot(Vi,Vr_JC,'m<','MarkerFaceColor','m')
plot(vi_Cell,vr_Cell,'k')
plot(vi_JC,vr_JC,'m')
plot(vi_Strekk,vr_Strekk,'b')
plot(vi_lab,vr_lab,'r')
% Legends
legend('CL with W_{c} = 174.1 MPa','CL with W_{c} = 364.3 MPa',...
    'Experimental data','JC','location','northwest');
legend('boxoff')
% axis limits
axis([300,max(Vi_lab),0,900])
% Label axes
xlabel('Initial velocity, v_i [m/s]','FontSize',FontSize)
ylabel('Residual velocity, v_r [m/s]','FontSize',FontSize)
set(gca,'FontSize',FontSize)
hold off
% Saving as pdf
saveas(h,'..\..\..\LaTex\figures\BallisticLimit\BaseModelIMPETUS','pdf')
% matlab2tikz('..\..\..\LaTex\figures\BallisticLimit\BaseModelIMPETUS.tikz',...
% 'width','\figurewidth','height','\figureheight')

%% Abaqus
h=figure('name','Abaqus');
plot(Vi,Vr_Strekk_ABA,'bd','MarkerFaceColor','b')
hold on
plot(Vi,Vr_Cell_ABA,'ks','MarkerFaceColor','k')
plot(Vi_lab,Vr_lab,'ro','MarkerFaceColor','r')
plot(vi_Cell_ABA,vr_Cell_ABA,'k')
plot(vi_Strekk_ABA,vr_Strekk_ABA,'b')
plot(vi_lab,vr_lab,'r')
% Legends
legend('CL with W_{c} = 174.1 MPa','CL with W_{c} = 364.3 MPa',...
    'Experimental data','location','northwest');
legend('boxoff')
% axis limits
axis([300,max(Vi_lab),0,900])
% Label axes
xlabel('Initial velocity, v_i [m/s]','FontSize',FontSize)
ylabel('Residual velocity, v_r [m/s]','FontSize',FontSize)
set(gca,'FontSize',FontSize)
hold off
% Saving as pdf
saveas(h,'..\..\..\LaTex\figures\BallisticLimit\BaseModelAbaqus','pdf')
% matlab2tikz('..\..\..\LaTex\figures\BallisticLimit\BaseModelAbaqus.tikz',...
% 'width','\figurewidth','height','\figureheight')

%% Plotting IMPETUS
% Plot fit with data.
h=figure('name','IMPETUS CL');
plot(Vi,Vr_Strekk,'bd','MarkerFaceColor','b')
```

```
hold on
plot(Vi,Vr_Cell,'ks','MarkerFaceColor','k')
plot(Vi_lab,Vr_lab,'ro','MarkerFaceColor','r')
plot(vi_Cell,vr_Cell,'k')
plot(vi_Strekk,vr_Strekk,'b')
plot(vi_lab,vr_lab,'r')
% Legends
legend('CL with W_{c} = 174.1 MPa','CL with W_{c} = 364.3 MPa',...
    'Experimental data','location','northwest');
legend('boxoff')
% axis limits
axis([300,max(Vi_lab),0,900])
% Label axes
xlabel('Initial velocity, v_i [m/s]','FontSize',FontSize)
ylabel('Residual velocity, v_r [m/s]','FontSize',FontSize)
set(gca,'FontSize',FontSize)
hold off
% Saving as pdf
saveas(h,'..\..\..\LaTex\figures\BallisticLimit\BaseModelIMPETUSCL','pdf')
% matlab2tikz('..\..\..\LaTex\figures\BallisticLimit\BaseModelIMPETUSCL.tikz',...
% 'width','\figurewidth','height','\figureheight')

%% Plotting IMPETUS
% Plot fit with data.
h=figure('name','IMPETUS JC');
plot(Vi,Vr_JC,'m<','MarkerFaceColor','m')
hold on
plot(Vi_lab,Vr_lab,'ro','MarkerFaceColor','r')
plot(vi_JC,vr_JC,'m')
plot(vi_lab,vr_lab,'r')
% Legends
legend('JC','Experimental data','location','northwest');
legend('boxoff')
% axis limits
axis([300,max(Vi_lab),0,900])
% Label axes
xlabel('Initial velocity, v_i [m/s]','FontSize',FontSize)
ylabel('Residual velocity, v_r [m/s]','FontSize',FontSize)
set(gca,'FontSize',FontSize)
hold off
% Saving as pdf
saveas(h,'..\..\..\LaTex\figures\BallisticLimit\BaseModelIMPETUSJC','pdf')
% matlab2tikz('..\..\..\LaTex\figures\BallisticLimit\BaseModelIMPETUSJC.tikz',...
% 'width','\figurewidth','height','\figureheight')

%% Abaqus
h=figure('name','Abaqus GTN');
plot(Vi,Vr_GTN,'ks','MarkerFaceColor','k')
hold on
plot(Vi,Vr_GTNSS,'bd','MarkerFaceColor','b')
plot(Vi_lab,Vr_lab,'ro','MarkerFaceColor','r')
plot(vi_GTN,vr_GTN,'k')
plot(vi_GTNSS,vr_GTNSS,'b')
plot(vi_lab,vr_lab,'r')
% Legends
legend('GTN','GTN with shear softening','Experimental data','location','northwest');
legend('boxoff')
```

```
% axis limits
axis([300,max(Vi_lab),0,900])
% Label axes
xlabel('Initial velocity, v_i [m/s]','FontSize',FontSize)
ylabel('Residual velocity, v_r [m/s]','FontSize',FontSize)
set(gca,'FontSize',FontSize)
hold off
% Saving as pdf
saveas(h,'..\..\..\LaTex\figures\BallisticLimit\BaseModelAbaqusGTN','pdf')
% matlab2tikz('..\..\..\LaTex\figures\BallisticLimit\BaseModelAbaqusGTN.tikz',...
% 'width','\figurewidth','height','\figureheight')

%% Abaqus
h=figure('name','Abaqus compare');
plot(Vi,Vr_Strekk_ABA,'bd','MarkerFaceColor','b')
hold on
plot(Vi,Vr_Cell_ABA,'ks','MarkerFaceColor','k')
plot(Vi,Vr_GTN,'m<','MarkerFaceColor','m')
plot(Vi_lab,Vr_lab,'ro','MarkerFaceColor','r')
plot(vi_Cell_ABA,vr_Cell_ABA,'k')
plot(vi_Strekk_ABA,vr_Strekk_ABA,'b')
plot(vi_GTN,vr_GTN,'m')
plot(vi_lab,vr_lab,'r')
% Legends
legend('CL with W_{c} = 174.1 MPa','CL with W_{c} = 364.3 MPa','GTN',...
    'Experimental data','location','northwest');
legend('boxoff')
% axis limits
axis([300,max(Vi_lab),0,900])
% Label axes
xlabel('Initial velocity, v_i [m/s]','FontSize',FontSize)
ylabel('Residual velocity, v_r [m/s]','FontSize',FontSize)
set(gca,'FontSize',FontSize)
hold off
% Saving as pdf
saveas(h,'..\..\..\LaTex\figures\BallisticLimit\BaseModelAbaqusCompare','pdf')
% matlab2tikz('..\..\..\LaTex\figures\BallisticLimit\BaseModelAbaqusCompare.tikz',...
% 'width','\figurewidth','height','\figureheight')
```

C.2 Numerical Micromechanical Unit Cell

```
clc
clf
close all
clear

FontSize=16;
color={[1,0.6,0.1],'c','m','g','k','r','b'};

% Triaxiality ratios
Tstr={'0,65','0,75','1,0','1,25','1,5','1,75','2,0'};
% Triaxiality ratios in Text string
T=[0.65,0.75,1.0,1.25,1.5,1.75,2.0];
% Triaxiality ratios
```

```
N_1=[5,3,4,2,2,2,1];
% Adjusting failure point
N_2=[25,25,25,25,25,25,25];
% Adjusting failure point
N_3=[1,2,2,1,2,2,0];

%% Finding critical void volume fraction and Critical Equivalent Strain for
%% each Triaxiality ratio
% Defining variables
f_c_1=zeros(1,length(Tstr));
f_c_2=f_c_1;
f_c_3=f_c_1;
Eeq_c_1=f_c_1;
Eeq_c_2=f_c_1;
Eeq_c_3=f_c_1;
Seq_c_1=f_c_1;
Seq_c_2=f_c_1;
Seq_c_3=f_c_1;
pl=f_c_1;
pl2=f_c_1;
pl3=f_c_1;
pl4=f_c_1;

startRow=2;
% Row to start importing data
endRow=inf;
% Row to end importing data

[~,T_3D,Eeq_c_3D]=Results3D();

for i=1:length(Tstr)
    %% Loading Data from File
    %% L=-1
    filename_1=['..\..\Abaqus\AxSymm_L=-1\DAT-filer\AlMgSi_f0=0,005_T=',...
        Tstr{i},'.dat']; % File name to load
    [~,~,Seq_1,Eeq_1,E1_1,~,f_1]=importfile(filename_1,startRow,endRow);
    % Importing data from file

    %% L=0
    filename_2=['..\..\Abaqus\PlaneStrain\TXT-FILES\AlMgSi_f0=0,005_T=',...
        Tstr{i},'.txt']; % File name to load
    [~,~,Seq_2,Eeq_2,E1_2,~,f_2]=file_2(filename_2,startRow,endRow);
    %Importing data from file

    %% L=1
    filename_3=['..\..\Abaqus\AxSymm_L=1\DAT-Files\AlMgSi_f0=0,005_T=',...
        Tstr{i},'_L=1,0.dat']; % File name to load
    [~,~,Seq_3,Eeq_3,~,E2_3,f_3]=importfile(filename_3,startRow,endRow);
    % Importing data from file
    [t,L3_3,DL3_3]=Ligament(Tstr{i});

    %% Finding critical/failure point
    % L=-1
    [M_1,~]=min(E1_1);
    % Finding min value of E1
    M_1=0.99*M_1;
    % Setting 99% of max as critical point
```

```
[~,n_1]=min(abs(E1_1-M_1));
% Finding entry nr. of critical point
n_1=n_1+N_1(i);
% Adjusting critical point
% L=0
[M_2,~]=min(E1_2);
% Finding min value of E1
M_2=0.99*M_2;
% Setting 99% of max as critical point
[~,n_2]=min(abs(E1_2-M_2));
% Finding entry nr. of critical point
n_2=n_2+N_2(i);
% Adjusting critical point
% L=1
[M_3,~]=min(E2_3);
% Finding min value of E2
M_3=0.95*M_3;
% Setting 99% of max as critical point
[~,n_3]=min(abs(E2_3-M_3));
% Finding entry nr. of critical point
n_3=n_3+N_3(i);

%% Plotting failure point
% Strain in radial direction vs. Equivalent Strain
figure(1);
pl(i)=plot(Eeq_1,abs(E1_1),'color',color{i});
% Plotting Equivalent Strain vs. Strain in r-direction
hold on
plot(Eeq_2,abs(E1_2),'color',color{i});
plot(Eeq_3,abs(E2_3),'color',color{i});
plot(Eeq_1(n_1),abs(E1_1(n_1)),'kx','MarkerFaceColor','k','MarkerSize',...
    8,'LineWidth',1.5) % Plotting critical point as X
plot(Eeq_2(n_2),abs(E1_2(n_2)),'kx','MarkerFaceColor','k','MarkerSize',...
    8,'LineWidth',1.5) % Plotting critical point as X
plot(Eeq_3(n_3),abs(E2_3(n_3)),'kx','MarkerFaceColor','k','MarkerSize',...
    8,'LineWidth',1.5) % Plotting critical point as X
% Stress vs. Strain
figure(2);
pl2(i)=plot(Eeq_1(1:n_1+5),Seq_1(1:n_1+5),'color',color{i});
% Plotting Equivalent Strain vs. Equivalent Stress
hold on
plot(Eeq_2(1:n_2+100),Seq_2(1:n_2+100),'color',color{i});
plot(Eeq_3,Seq_3,'color',color{i});
plot(Eeq_1(n_1),Seq_1(n_1),'kx','MarkerFaceColor','k','MarkerSize',...
    8,'LineWidth',1.5) % Plotting critical point as X
plot(Eeq_2(n_2),Seq_2(n_2),'kx','MarkerFaceColor','k','MarkerSize',...
    8,'LineWidth',1.5)
plot(Eeq_3(n_3),Seq_3(n_3),'kx','MarkerFaceColor','k','MarkerSize',...
    8,'LineWidth',1.5)
% Void Volume fraction vs. Equivalent Strain
figure(3);
pl3(i)=plot(Eeq_1(1:n_1+5),f_1(1:n_1+5),'color',color{i});
hold on
plot(Eeq_2(1:n_2+100),f_2(1:n_2+100),'color',color{i});
plot(Eeq_3,f_3,'color',color{i});
plot(Eeq_1(n_1),f_1(n_1),'kx','MarkerFaceColor','k','MarkerSize',...
    8,'LineWidth',1.5) % Plotting critical point as X
```

```
    plot(Eeq_2(n_2),f_2(n_2),'kx','MarkerFaceColor','k','MarkerSize',...
        8,'LineWidth',1.5)
    plot(Eeq_3(n_3),f_3(n_3),'kx','MarkerFaceColor','k','MarkerSize',...
        8,'LineWidth',1.5)
    figure(4)
    pl4(i)=plot(Eeq_3,DL3_3,'color',color{i});
    hold on
    plot(Eeq_3(n_3),DL3_3(n_3),'kx','MarkerFaceColor','k','MarkerSize',7.5)

    %% Volume fraction ( f ) at failure +++
    % L=-1
    f_c_1(i)=f_1(n_1);
    % Critical void volume fraction for each triaxiality ratio
    Eeq_c_1(i)=Eeq_1(n_1);
    % Critical Equivalent Strain for each triaxiality ratio
    Seq_c_1(i)=Seq_1(n_1);
    % L=0
    f_c_2(i)=f_2(n_2);
    % Critical void volume fraction for each triaxiality ratio
    Eeq_c_2(i)=Eeq_2(n_2);
    % Critical Equivalent Strain for each triaxiality ratio
    % L=1
    f_c_3(i)=f_3(n_3);
    % Critical void volume fraction for each triaxiality ratio
    Eeq_c_3(i)=Eeq_3(n_3);
    % Critical Equivalent Strain for each triaxiality ratio
    Seq_c_3(i)=Seq_3(n_3);
end

%% Calibrating Cockcroft-Latham
% Calculating accumulated plastic strain at fauilure
E=70000;
% Young's modulus
p_f_1=Eeq_c_1-Seq_c_1/E;
% accumulated plastic strain at fauilure
p_f_2=Eeq_c_2-Seq_c_2/E;
p_f_3=Eeq_c_3-Seq_c_3/E;

mu_sig=[-1,0,1];
H_1=66.26*p_f_1+62*p_f_1+62/32.36*(exp(-32.36*p_f_1)+1)+126.46*p_f_1+...
    126.46/4.21*(exp(-4.21*p_f_1)+1);
H_2=66.26*p_f_2+62*p_f_2+62/32.36*(exp(-32.36*p_f_2)+1)+126.46*p_f_2+...
    126.46/4.21*(exp(-4.21*p_f_2)+1);
H_3=66.26*p_f_3+62*p_f_3+62/32.36*(exp(-32.36*p_f_3)+1)+126.46*p_f_3+...
    126.46/4.21*(exp(-4.21*p_f_3)+1);

H=[H_1;H_2;H_3]';

[fitresult,~]=CL_Fit(mu_sig,T,H,FontSize);
Wcr=fitresult.Wcr;

%% Calibrating Johnson - Cook
pf=[p_f_1;p_f_2;p_f_3]';

[fitresult,~]=JC_Fit(mu_sig,T,pf,FontSize);
D1=fitresult.D1;
D2=fitresult.D2;
```

```
D3=fitresult.D3;
D6=fitresult.D6;

%% Calibrating Cockcroft-Latham without L=0
mu_sig=[-1,1];
H_1=66.26*p_f_1+62*p_f_1+62/32.36*(exp(-32.36*p_f_1)+1)+126.46*p_f_1+...
    126.46/4.21*(exp(-4.21*p_f_1)+1);
H_3=66.26*p_f_3+62*p_f_3+62/32.36*(exp(-32.36*p_f_3)+1)+126.46*p_f_3+...
    126.46/4.21*(exp(-4.21*p_f_3)+1);

H=[H_1;H_3]';

[fitresult,~]=CL_Fit_uten(mu_sig,T,H,FontSize);
Wcr_utenL0=fitresult.Wcr;

%% Calibrating Johnson - Cook without L=0
pf=[p_f_1;p_f_3]';

[fitresult,~]=JC_Fit_uten(mu_sig,T,pf,FontSize);
D1_utenL0=fitresult.D1;
D2_utenL0=fitresult.D2;
D3_utenL0=fitresult.D3;

%% Plotting
Tstr={'\sigma* = 0.65','\sigma* = 0.75','\sigma* = 1.00','\sigma* = 1.25',...
    '\sigma* = 1.50','\sigma* = 1.75','\sigma* = 2.00'};
%% Edit figure 1
h=figure(1);
% Legends
legend(pl,Tstr,'location','southeast')
legend('boxoff')
% axis limits
% Label axes
xlabel('Equivalent strain, E_{eq}','FontSize',FontSize)
ylabel('Strain, || E_{1} ||','FontSize',FontSize)
set(gca,'FontSize',FontSize)
% Saving as pdf
saveas(h,'..\..\LaTex\figures\CelleSim\Cellefailure_ALL','pdf')
matlab2tikz('..\..\LaTex\figures\CelleSim\Cellefailure_ALL.tikz',...
    'width','\figurewidth','height','\figureheight')

%% Edit figure 2
h=figure(2);
% Legends
legend(pl2,Tstr,'location','southeast')
legend('boxoff')
% axis limits
% Label axes
xlabel('Equivalent strain, E_{eq}','FontSize',FontSize)
ylabel('Equivalent stress, \Sigma_{eq} [Mpa]','FontSize',FontSize)
set(gca,'FontSize',FontSize)
% Saving as pdf
saveas(h,'..\..\LaTex\figures\CelleSim\StressStrain_ALL','pdf')
matlab2tikz('..\..\LaTex\figures\CelleSim\StressStrain_ALL.tikz',...
    'width','\figurewidth','height','\figureheight')

%% Edit figure 3
```

```
h=figure(3);
% Legends
legend(pl3,Tstr,'location','northeast')
legend('boxoff')
% axis limits
% Label axes
xlabel('Equivalent strain, E_{eq}','FontSize',FontSize)
ylabel('Void volume fraction, f','FontSize',FontSize)
set(gca,'FontSize',FontSize)
% Saving as pdf
saveas(h,'..\..\LaTex\figures\CelleSim\VoidVolumeFraction_ALL','pdf')
matlab2tikz('..\..\LaTex\figures\CelleSim\VoidVolumeFraction_ALL.tikz',...
    'width','\figurewidth','height','\figureheight')

%% Edit figure 4
h=figure(4);
% Legends
legend(pl4,Tstr,'location','southeast')
legend('boxoff')
% axis limits
% Label axes
xlabel('Equivalent strain, E_{eq}','FontSize',FontSize)
ylabel('Change in ligament thickness, \partialL_{33}/\partialt','FontSize',FontSize)
set(gca,'FontSize',FontSize)
% Saving as pdf
saveas(h,'..\..\LaTex\figures\CelleSim\Ligament_All','pdf')
matlab2tikz('..\..\LaTex\figures\CelleSim\Ligament_All.tikz',...
    'width','\figurewidth','height','\figureheight')

%% Plotting critical void volume fraction vs. Triaxiality ratio
h=figure(5);
B(1)=plot(T,f_c_1,'bs:','MarkerFaceColor','b');
hold on
B(2)=plot(T,f_c_2,'rd:','MarkerFaceColor','r');
B(3)=plot(T,f_c_3,'mo:','MarkerFaceColor','m');
% Legends
legend(B,{'\mu_{\sigma} = -1','\mu_{\sigma} = 0','\mu_{\sigma} = 1'},...
    'Location','northwest')
legend('boxoff')
% axis limits
axis([min(T),max(T),min(min([f_c_1,f_c_2,f_c_3]))/...
    3,1.1*max(max([f_c_1,f_c_2,f_c_3]))])
% Label axes
xlabel('Triaxiality ratio, \sigma*','FontSize',FontSize)
ylabel('Critical void volume fraction, f_c','FontSize',FontSize)
set(gca,'FontSize',FontSize)
hold off
% Saving as pdf
saveas(h,'..\..\LaTex\figures\CelleSim\VoidFraction_ALL','pdf')
matlab2tikz('..\..\LaTex\figures\CelleSim\VoidFraction_ALL.tikz',...
    'width','\figurewidth','height','\figureheight')

%% Plotting Critical Equivalent Strain vs. Triaxiality ratio
C=0.2;
[Shear_c_2D,Shear_c_3D]=ShearCell(C);
h=figure(6);
B(1)=plot(T,Eeq_c_1,'bs:','MarkerFaceColor','b');
```

```
hold on
B(2)=plot([0,T],[Shear_c_2D,Eeq_c_2],'rd:','MarkerFaceColor','r');
B(3)=plot(T,Eeq_c_3,'mo:','MarkerFaceColor','m');
% 3D values
% Legends
 legend([B(1),B(2),B(3)],{'\mu_{\sigma} = -1','\mu_{\sigma} = 0',...
     '\mu_{\sigma} = 1'},'Location','northeast')
legend('boxoff')
% axis limits
xlim([min([0,T]),max([0,T])])
% Label axes
xlabel('Triaxiality ratio, \sigma*','FontSize',FontSize)
ylabel('Critical equivalent strain, E_{eq}^{c}','FontSize',FontSize)
set(gca,'FontSize',FontSize)
hold off
% Saving as pdf
saveas(h,'..\..\LaTex\figures\CelleSim\EquivalentStrain_ALL','pdf')
matlab2tikz('..\..\LaTex\figures\CelleSim\EquivalentStrain_ALL.tikz',...
    'width','\figurewidth','height','\figureheight')

%% Plotting Critical Equivalent Strain vs. Triaxiality ratio Compared to 3D
h=figure(7);
B(1)=plot(T,Eeq_c_1,'bs--','MarkerFaceColor','b');
hold on
B(2)=plot(T_3D{1},Eeq_c_3D{1},'bd--','MarkerFaceColor','b');
B(3)=plot([0,T],[Shear_c_2D,Eeq_c_2],'rs-.','MarkerFaceColor','r');
B(4)=plot([0;T_3D{2}],[Shear_c_3D;Eeq_c_3D{2}],'rd-.','MarkerFaceColor','r');
B(5)=plot(T,Eeq_c_3,'ms:','MarkerFaceColor','m');
B(6)=plot(T_3D{3},Eeq_c_3D{3},'md:','MarkerFaceColor','m');
% Legends
legend(B,{'2D Cell, \mu_{\sigma} = -1','3D Cell','2D Cell, \mu_{\sigma} = 0',...
    '3D Cell','2D Cell, \mu_{\sigma} = 1','3D Cell'},'Location','northeast')
legend('boxoff')
% axis limits
xlim([min([0,T]),max([0,T])])
% Label axes
xlabel('Triaxiality ratio, \sigma*','FontSize',FontSize)
ylabel('Critical equivalent strain, E_{eq}^{c}','FontSize',FontSize)
set(gca,'FontSize',FontSize)
hold off
% Saving as pdf
saveas(h,'..\..\LaTex\figures\CelleSim\EquivalentStrain_ALL_Compare_3D','pdf')
matlab2tikz('..\..\LaTex\figures\CelleSim\EquivalentStrain_ALL_Compare_3D.tikz',...
    'width','\figurewidth','height','\figureheight')

%% Plotting Critical Equivalent Strain vs. Triaxiality ratio
h=figure(99);
plot([0,T],[Shear_c_2D,Eeq_c_2],'ks:','MarkerFaceColor','k');
% 3D values
% Legends
% axis limits
ylim([0,0.6])
xlim([min([0,T]),max([0,T])])
% Label axes
xlabel('Triaxiality ratio, \sigma*','FontSize',FontSize)
ylabel('Critical equivalent strain, E_{eq}^{c}','FontSize',FontSize)
set(gca,'FontSize',FontSize)
```

```
hold off
% Saving as pdf
saveas(h,'..\..\LaTex\figures\CelleSim\L=0\CriticalEquivalentStrainShear','pdf')
matlab2tikz('..\..\LaTex\figures\CelleSim\L=0\CriticalEquivalentStrainShear.tikz',...
    'width','\figurewidth','height','\figureheight')
```

D FEM Input Files

D.1 IMPETUS Input File

```
*UNIT_SYSTEM
# Defines the Unit System: SI Units
SI
*INCLUDE
# Importing the Bullet Mesh Created in Abaqus
Bullet_5.k
1, 1, 1, 100000, 100000
0, 0, 0, -28e-3, 0, 0
0,-1,0,1,0,0
*INCLUDE'
# Importing the Target Mesh Created in Abaqus
Target.k
1e-3, 1e-3, 1e-3, 0, 0
0, 0, 0, 0, 0, 0
0,-1,0,1,0,0
*PARAMETER
# Parameters used
%A   = 66.26e6  # Initial yield Stress, Sigma_0
%Q1  = 62.00e6  # Voce Hardening Parameter
%C1  = 32.36    # Voce Hardening Parameter
%Q2  = 126.46e6 # Voce Hardening Parameter
%C2  = 4.21     # Voce Hardening Parameter
%Wcr = 364.3e6  # Critical Plastic Work, CL Criterion
%Vi=700         # Initial Velocity
%endtime=1.5e-4 # Integration Time
%mu=0.05        # Friction Coef.
%terode=0       # Time Step to Erode Elements
%tikk=1         # 0,1 or 2, for failed elements is not eroded,
                # is eroded or nodesplitting
*TIME
# Integration Time is Determined
[%endtime]
*INITIAL_TEMPERATURE
# Initial Temperature in the model is Determined
# by *FUNCTION 999. Hence T_i = 293 K
ALL, 0, 999
*FUNCTION
999
293
*PART
# Creates parts
"Plate Part"
1,1 , , , ,[%terode]
*PART
```

```
"Kule Part"
3,3
*MAT_METAL
# Target Material
1,2700,70.0e9,0.3,1,1
1,0,0,0.001,5.0e-4,1,293,893
*MAT_RIGID
# Bullet Material
3,7850
*FUNCTION
# Voce Hardening Curve
1
%A + %Q1*(1 - exp(-%C1*epsp)) + %Q2*(1 - exp(-%C2*epsp))
*PROP_DAMAGE_CL
# Cockcroft-Latham Fracture Criterion
1,[%tikk]
[%Wcr]
*PROP_THERMAL
# Termal Propeties for the target
1,2.3e-5,910,0,0.9,293
*GEOMETRY_PIPE
# Change the Polynomial Order of the Elements in the Center to 3.
2
-1,0,0,1,0,0,16.0e-3
*CHANGE_P-ORDER
ALL,0,3,2
*BC_SYMMETRY
# Boundary Conditions
0,1,2
*COORDINATE_SYSTEM_FIXED
1,0,0,0
0,0,1
*COORDINATE_SYSTEM_FIXED
2,0,0,0
0,[sin(5)],[-cos(5)]
*BC_MOTION
987
G,56,xyz,0
*GEOMETRY_PIPE
56
-1,0,0,1,0,0,55e-3,49e-3
*INITIAL_VELOCITY
# Initial Velocity of the Bullet
P,3,[%Vi]
*CONTACT
# Contact
"General contact"
123
ALL,0,ALL,0,[%mu],1e15
1,,,,,1e-8
*END
```

D.2 Abaqus Input Files

D.2.1 Abaqus Model

```
*Heading
** Job name: SMM Model name: BaseModel
** Generated by: Abaqus/CAE 6.14-1
*Preprint, echo=NO, model=NO, history=NO, contact=NO
**
** PARTS
**
*Part, name=Bullet
*End Part
**
*Part, name=Target
*End Part
**
**
** ASSEMBLY
**
*Assembly, name=Assembly
**
*Instance, name=Target-1, part=Target
*Node
#
# NODE INFORMATION NOT INCLUDED
#
      *Element, type=C3D8R
#
# ELEMENT INFORMATION NOT INCLUDED
#
 *Elset, elset=_PickedSet38, internal, instance=Target-1, generate
    1,  8057,     1
*Nset, nset=_PickedSet39, internal, instance=Target-1
#
# NOT INCLUDED
#
*Elset, elset=_PickedSet39, internal, instance=Target-1, generate
 7908,  8057,     1
*Nset, nset=_PickedSet40, internal
 1,
*Nset, nset=_PickedSet41, internal
 1,
*Nset, nset="_T-Datum csys-2", internal
_PickedSet38,
*Transform, nset="_T-Datum csys-2"
0.996194698091745,0.,-0.0871557427476581,0.,1.,0.
** Constraint: Bullet
*Rigid Body, ref node=_PickedSet32, analytical surface=Bullet-1.RigidSurface_
*Element, type=MASS, elset=_PickedSet42_Inertia-1_MASS_
1, 1
*Mass, elset=_PickedSet42_Inertia-1_MASS_
7.2078e-08,
*Element, type=ROTARYI, elset=_PickedSet42_Inertia-1_ROTI_
```

```
2, 1
*Rotary Inertia, elset=_PickedSet42_Inertia-1_ROTI_
1., 1., 1., 0., 0., 0.
*End Assembly
**
** MATERIALS
**
*include, input=mat_Heidi_new.inp
**
** INTERACTION PROPERTIES
**
*Surface Interaction, name=IntProp-1
*Friction
 0.05,
*Surface Behavior, pressure-overclosure=HARD
**
** BOUNDARY CONDITIONS
**
** Name: BulletFixed Type: Displacement/Rotation
*Boundary
_PickedSet40, 1, 1
_PickedSet40, 3, 3
_PickedSet40, 4, 4
_PickedSet40, 5, 5
_PickedSet40, 6, 6
** Name: Center Type: Displacement/Rotation
*Boundary
_PickedSet39, 1, 1
_PickedSet39, 3, 3
** Name: Fixed Type: Displacement/Rotation
*Boundary
_PickedSet37, 1, 1
_PickedSet37, 2, 2
_PickedSet37, 3, 3
** Name: Sym1 Type: Symmetry/Antisymmetry/Encastre
*Boundary
_PickedSet36, ZSYMM
** Name: Sym2 Type: Symmetry/Antisymmetry/Encastre
*Boundary
_PickedSet38, ZSYMM
**
** PREDEFINED FIELDS
**
** Name: InVel   Type: Velocity
*Initial Conditions, type=VELOCITY
_PickedSet41, 1, 0.
_PickedSet41, 2, 700000.
_PickedSet41, 3, 0.
** ----------------------------------------------------------------
**
** STEP: Load
**
*Step, name=Load, nlgeom=YES
*Dynamic, Explicit, scale factor=0.9
, 0.00015
*Bulk Viscosity
0.06, 1.2
```

```
**
** INTERACTIONS
**
** Interaction: Int-1
*Contact, op=NEW
*Contact Inclusions, ALL EXTERIOR
*Contact Property Assignment
 ,  , IntProp-1
**
** OUTPUT REQUESTS
**
*Restart, write, number interval=1, time marks=NO
**
** FIELD OUTPUT: F-Output-1
**
*Output, field, number interval=100
*Node Output
A, RF, U, V
*Element Output, directions=YES
EVF, LE, PE, PEEQ, PEEQVAVG, PEVAVG, S, SDV, STATUS, SVAVG
*Contact Output
CSTRESS,
**
** HISTORY OUTPUT: H-Output-1
**
*Output, history, variable=PRESELECT, time interval=1.5e-06
**
** HISTORY OUTPUT: Mass
**
*Output, history
*Integrated Output, elset=Target
MASS,
**
** HISTORY OUTPUT: Vel
**
*Output, history, time interval=1.5e-07
*Node Output, nset=Bullet
V2,
*End Step
```

D.2.2 SIMLab Metal Model Material Input

```
**************************************************************************
** Material card for ABAQUS explicit
** von Mises yield surface
** Isotropic hardening
** Visco-plasticity
** Thermo-plasticity
** Cockcroft-Latham
**************************************************************************
** The name of the material card must start with SMM_ when used with solid elements
**************************************************************************
*Material, name=SMM_AlMgSi_original
*Density
2.7E-9,
```

```
**********************************************************************
** This file (DEPVAR_SMM.inc) is used to specify the names of the history
** variables to the ABAQUS output file
*INCLUDE,INPUT=./DEPVAR_SMM.inc
**********************************************************************
*USER MATERIAL,CONSTANTS=41
**  EFLAG,    YFLAG, RMAPFLAG,  HFLAG,    VFLAG,    TFLAG,    DFLAG,    SFFLAG
        1,        1,         4,       1,        1,       12,       12,         0
** STFLAG,         E,        NU, SIGMA0,      KSI, THETAR1,      QR1,  THETAR2
        0,    70000,       0.3,  66.26,      0.1, 2006.32,       62,   532.39
**     QR2, THETAR3,       QR3,dRdpmin,       CS,     PDOT,       TI,        T0
    126.4,        0,         0,       0,    0.001,   0.0005,      293,       293
**      TM,      RHO,        CP, BETATQ,       MS,    DINIT,    DCRIT,        WC
       893,   2.7E-9,     910E6,    0.9,        1,        0,        1,     364.3
**     PHI,    GAMMA,        Tc,
        1,        1,       804,
```